Fall 2017

Biophysical mechanisms of frequency-dependence and its neuromodulation in neurons in oscillatory networks

David Michael Fox
New Jersey Institute of Technology

Recommended Citation

Fox, David Michael, "Biophysical mechanisms of frequency-dependence and its neuromodulation in neurons in oscillatory networks" (2017). *Dissertations*. 52.
https://digitalcommons.njit.edu/dissertations/52

ABSTRACT

BIOPHYSICAL MECHANISMS OF FREQUENCY-DEPENDENCE AND ITS NEUROMODULATION IN NEURONS IN OSCILLATORY NETWORKS

By
David Michael Fox

In response to oscillatory input, many isolated neurons exhibit a preferred frequency response in their voltage amplitude and phase shift. Membrane potential resonance (MPR), a maximum amplitude in a neuron's input impedance at a non-zero frequency, captures the essential subthreshold properties of a neuron, which may provide a coordinating mechanism for organizing the activity of oscillatory neuronal networks around a given frequency. In the pyloric central pattern generator network of the crab *Cancer borealis*, for example, the pacemaker group pyloric dilator neurons show MPR at a frequency that is correlated with the network frequency. This dissertation uses the crab pyloric CPG to examine how, in one neuron type, interactions of ionic currents, even when expressed at different levels, can produce consistent MPR properties, how MPR properties are modified by neuromodulators and how such modifications may lead to distinct functional effects at different network frequencies.

In the first part of this dissertation it is demonstrated that, despite the extensive variability of individual ionic currents in a neuron type such as PD, these currents can generate a consistent impedance profile as a function of input frequency and therefore result in stable MPR properties. Correlated changes in ionic current parameters are associated with the dependence of MPR on the membrane potential range. Synaptic inputs or neuromodulators that shift the membrane potential range can modify the interaction of multiple resonant currents and therefore shift the MPR frequency.

Neuromodulators change the properties of voltage-dependent ionic currents. Since ionic current interactions are nonlinear, the modulation of excitability and the impedance profile may depend on all ionic current types expressed by the neuron. MPR is generated by the interaction of positive and negative feedback effects due to fast amplifying and slower resonant currents. Neuromodulators can modify existing MPR properties to generate antiresonance (a minimum amplitude response). In the second part of this dissertation, it is shown that the neuropeptide proctolin produces antiresonance in the follower lateral pyloric neuron, but not in the PD neuron. This finding is inconsistent with the known influences of proctolin. However, a novel proctolin-activated ionic current is shown to produce the antiresonance. Using linear models, antiresonance is then demonstrated to amplify MPR in synaptic partner neurons, indicating a potential function in the pyloric network.

Neuromodulators are state dependent, so that their action may depend on the prior activity history of the network. It is shown that state-dependence may arise in part from the time-dependence of an inactivating inward current targeted by the neuromodulator proctolin. Due to the kinetics of inactivation, this current advances the burst phase and increases the duty cycle of the neuron, but mainly at higher network frequencies.

These results demonstrate that the effect of neuromodulators on MPR in individual neuron types depends on the nonlinear interaction of modulator-activated and other ionic currents as well as the activation of currents with frequency-dependent properties. Consequently, the action of neuromodulators on the output of oscillatory networks may depend on the frequency of oscillations and be predictable from the MPR properties of the network neurons.

BIOPHYSICAL MECHANISMS OF FREQUENCY-DEPENDENCE AND ITS NEUROMODULATION IN NEURONS IN OSCILLATORY NETWORKS

by
David Michael Fox

A Dissertation
Submitted to the Faculty of
New Jersey Institute of Technology
and Rutgers, The State University of New Jersey - Newark
in Partial Fulfillment of the Requirements for the Degree of
Doctor of Philosophy in Biology

Department of Biological Sciences

August 2017

APPROVAL PAGE

FREQUENCY-DEPENDENT MECHANISMS OF GENERATION ANDMODULATION OF NEURONS IN OSCILLATORY NETWORKS

David Michael Fox

Dr. Farzan Nadim, Dissertation Co-Advisor Date
Professor of Biology, NJIT

Dr. Horacio G. Rotstein, Dissertation Co-Advisor Date
Professor of Mathematical Sciences, NJIT

Dr. Gal Haspel, Committee Member Date
Assistant Professor of Biology, NJIT

Dr. Jorge P. Golowasch, Committee Member Date
Professor, Associate Chair of Biology, NJIT

Dr. Michael P. Nusbaum, Committee Member Date
Professor of Neuroscience, University of Pennsylvania, Philadelphia, PA

BIOGRAPHICAL SKETCH

Author:	David Michael Fox
Degree:	Doctor of Philosophy
Date:	August 2017

Undergraduate and Graduate Education:

- Doctor of Philosophy in Biology,
  New Jersey Institute of Technology, Newark, NJ, 2017

- Master of Science in Bioinformatics and Computational Systems Biology,
  Newcastle University, Newcastle, United Kingdom, 2009

- Bachelor of Science in Computer Science,
  Newcastle University, Newcastle, United Kingdom, 2008

Major: Biology

Presentations and Publications:

Fox DM, Tseng H, Smolinksi TG, Rotstein HG, Nadim F. Mechanisms of generation of membrane potential resonance in a neuron with multiple resonant ionic currents. Vervaeke K, ed. *PLoS* Computational Biology. 2017; 13(6): e1005565.

Fox DM, Rotstein HG, Nadim F. Bursting in neurons and small networks. In: Jaeger D, Jung R, eds. Encyclopedia of computational neuroscience. New York, NY: Springer; 2014.

Fox DM, Rotstein HG, Nadim F. Neuromodulator-induced antiresonance. In: International conference of mathematical neuroscience. Boulder, CO; 2017.

Fox DM, Rotstein HG, Nadim F. Neuromodulation produces complex changes in resonance profiles of neurons in an oscillatory network. In: Society for Neuroscience meeting. San Diego, California; 2016.

Fox DM, Tseng H, Rotstein HG, Nadim F. Using multi-objective evolutionary to predict the parameters that determine membrane resonance in a biophysical model of bursting neurons. BMC Neuroscience. 2014; 15(1): 79.

Fox DM, Tseng H, Rotstein HG, Nadim F, The role of a persistent inward current in shaping membrane resonance properties of different neuron types in an oscillatory network. In: Society for neuroscience meeting, Washington, DC; 2014.

Nadim F, Rotstein HG, Fox DM. Predicting the firing phase of an oscillatory neuron from its impedance profile. BMC Neuroscience. 2013; 14(1): 132.

Fox DM, Tseng H, Rotstein HG, Nadim F. Membrane resonance of bursting neuron captured with an $I_{\mathrm{Ca}}/I_{\mathrm{h}}$ model using multi-objective evolutionary algorithms. BMC Neuroscience. 2013; 14(1): 289.

Rotstein HG, Fox DM, Nadim F. Predicting the firing phase of an oscillator from its subthreshold impedance profile. In: Society for neuroscience meeting, San Diego, California; 2013.

Fox DM, Tseng H, Rotstein HG, Nadim F. Membrane potential resonance of burst neuron captured with an $I_{\mathrm{Ca}}/I_{\mathrm{H}}$ biophysical model using multi-objective evolutionary algorithms. In: Society for neuroscience meeting, San Diego, California; 2013.

Fox DM, Andras P. A model of endocannabinoid 2AG-mediated depolarization-induced suppression of inhibition. BMC Neuroscience. 2010; 11(1): 189

I would like to dedicate this thesis to my soulmate Michelle VanTieghem, without whom the successful and timely completion of this dissertation would not have been possible.

ACKNOWLEDGMENT

First and foremost, special note of thanks to my co-Advisors Drs. Farzan Nadim and Horacio G. Rotstein for their patience, support and enormous freedom afforded me throughout the years. I believe that if I learn to identify my career goals early and be systematic in my approach, work hard with focus, determination, and critical self-evaluation, I can be as accomplished as you are.

Thank you to my committee members for serving on my Committee: Dr. Gal Haspel, Dr. Jorge Golowasch, and Dr. Michael P. Nusbaum. With your critical feedback on the organization and presentation of ideas in the manuscript, I have been able to produce a thesis that I can be proud of in the future. I appreciate your willingness to cooperate with me in spite of my stubbornness.

I would also like to thank Dr. Haroon Anwar for support both as a friend and a colleague. He helped me to overcome many obstacles both emotional and scientific. I also appreciate all of the helpful scientific brainstorming and the debugging of computer codes.

I would also like to express my most sincere gratitude to my Mother for her unconditional love and support. She gave me the courage and strength to carry on even in difficult times.

Last, but not least, I devote my earnest appreciation to my loving girlfriend Michelle VanTieghem. With her help in planning and time-management, I was able to prioritize my work, focus my efforts and not get distracted. Without her, this thesis would not have been completed.

TABLE OF CONTENTS

TABLE OF CONTENTS
(Continued)

TABLE OF CONTENTS
(Continued)

LIST OF TABLES

LIST OF FIGURES

Figure **Page**

LIST OF FIGURES
(Continued)

LIST OF FIGURES
(Continued)

CHAPTER 1

INTRODUCTION

1.1 Objective

The objective of this dissertation is to understand the biophysical mechanisms that shape the frequency-dependent properties of single neurons and in turn how these properties determine the action of neuromodulation on the activity of a neuron in an oscillatory network.

1.2 Background and Motivation

Rhythmic network oscillations are ubiquitous in the nervous system. Since these oscillations underlie many behaviors, their abnormalities have been implicated in various motor and cognitive impairments. Rhythmic oscillations underlying different behaviors can be characterized by frequency and reflect dynamic interactions between neurons in a network. Furthermore, certain behaviors require network output within specific frequency ranges. Therefore, it is important to understand the factors that shape the frequency of neural networks.

One such factor proposed to contribute to the frequency of network level oscillations is the subthreshold frequency-dependent response of individual neurons. Networks are often composed of neurons that exhibit preferred frequencies in the form of membrane potential resonance (MPR), in which neurons produce a maximum subthreshold voltage amplitude response to oscillatory current inputs at a preferred (resonance) frequency (f_{res}). A different, but related, phenomenon is the zero phase response, in which neurons synchronize with their inputs at some non-zero frequency

($f_{\varphi=0}$). In many networks, the MPR has been implicated in the generation of oscillations because the f_{res} of a single neuron is correlated with the network frequency [1-5]. In some cases, the same low-threshold inactivating currents that give rise to oscillations also give rise to MPR. We were interested in the biophysical mechanisms that shape the MPR of neurons, since factors that affect f_{res} also affect the network frequency in the same direction [4].

Neurons can demonstrate a broad range of subthreshold behavior as seen in the impedance amplitude profile (*Z*-profile). For example in the CA1 hippocampus, the *Z*-profile of pyramidal neurons shows a single resonance peak in the theta frequency band (4-12 Hz); others produce more complex shapes, such as in CA1 fast-spiking interneurons, in which there is a trough at low frequencies (antiresonance) corresponding to theta followed by a peak at higher frequencies corresponding to gamma frequency band (Figure 1.1). Antiresonance has been reported experimentally [6] and linear modeling has provided minimum conditions for its generation [7, 8]. Often different neuron types exhibiting both forms of *Z*-profiles interact in the same network and it is not clear what antiresonance contributes to the dynamics of neurons and networks even in small two-cell networks connected via reciprocal inhibition. Previous studies showed that MPR influences network oscillations through electrical coupling [9]. Even though biophysical parameters and their interaction shape the *Z* profile, this effect was independent of the values of biophysical parameters. We will determine if there is a functional role of antiresonance in shaping the activity of individual neurons and networks.

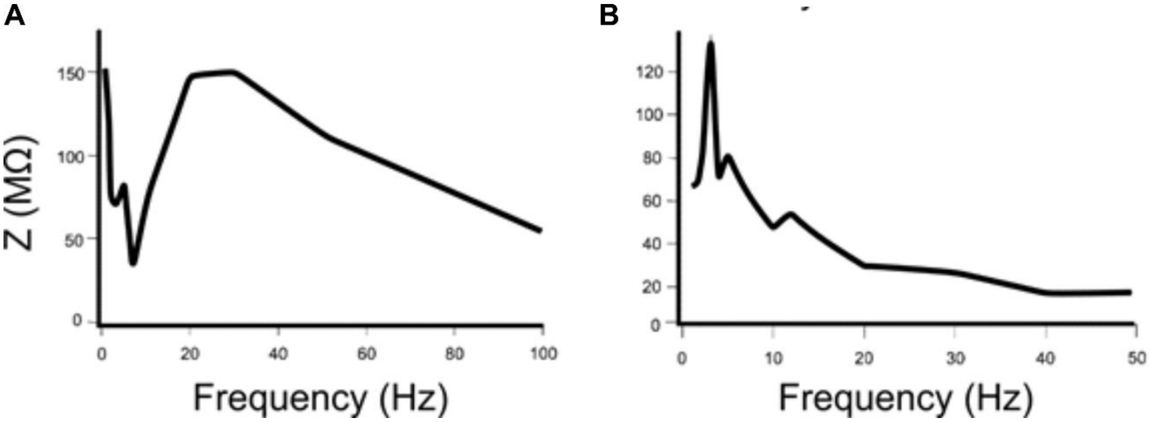

Figure 1.1 Distinct neuron types exhibit different impedance profile shapes. (A) The impedance profile of an interneuron of the CA1 hippocampus shows a resonance peak at an input frequency of 30 Hz, and the suppression at input frequencies below 20 Hz (antiresonance). (B) The impedance profile of a pyramidal neuron of the CA1 hippocampus shows a resonance peak at an input frequency of 3 Hz with no antiresonance. Figure modified from [6]

Characteristic frequencies of oscillatory networks underlie different behavioral states. Simultaneously, networks must be flexible and capable of producing different outputs to meet the changing environmental demands on behavior. Neuromodulation underlies this flexibility. The output of all networks in the nervous system is under the constant control via the actions of various amines, peptides and gases [10, 11]. Each substance can modify the properties of neurons and synapses in the network. Therefore, changes in the modulatory background may lead to changes in the network state and ultimately behavior.

We test multiple hypotheses regarding the frequency-dependent properties of neurons and state-dependent neuromodulation. We first examine the hypothesis that stability of MPR can arise in spite of variability in the biophysical properties of the multiple underlying resonant currents. I next examine the hypothesis that antiresonance preferentially amplifies the voltage response of coupled neurons in a narrow range of frequencies around f_{res} through reciprocal inhibition. Finally, we examine the hypothesis that the state dependence of neuromodulators on the activity of a follower neuron arises from both the time-dependence of modulator-activated currents and the interaction with variable baseline intrinsic currents.

1.2.1 Central Pattern Generators

Many essential behaviors including walking and breathing are rhythmic; that is, they involve repetitive sequences of muscle contractions. The timing cues to muscles are carried by the output of small neural networks called central pattern generators (CPGs) networks characterized by coherent oscillations[12]. CPGs have been found in both invertebrates, such as in leech and decapod crustaceans [13] and in vertebrates such as the Pre-Bötzinger complex controlling the respiratory rhythm in mammals [14] and swimming generated in the lamprey spinal cord [15].

Oscillatory output arises in CPG networks even in the absence of direct patterned inputs to the network. Invertebrate CPGs, such as the pyloric network of the decapod crustacean *Cancer borealis*, have provided invaluable insight about intrinsic and synaptic properties that govern the organization of oscillatory activity. Moreover, the effect of neuromodulators on these properties of well-characterized CPG networks is vast and has contributed general principles of the modulation of network dynamics.

1.2.2 The Stomatogastric Nervous System

The stomatogastric nervous system (STNS) in the crab *Cancer borealis* is an extension of the central nervous system (Figure 1.2). It has contributed enormously to understanding the general principles that underlie the generation of coordinated network activity at the cellular level [12]. The STNS consists of 4 interconnected ganglia (and the connecting nerves): the paired commissural ganglia; the esophageal ganglion; and the stomatogastric ganglion (STG). The STG contains about 26-30 neurons depending on the species that together form two distinct but interacting CPGs, which control different parts of a multi-compartment stomach involved in feeding. Food enters the gastric mill and is broken down by teeth (chewing) before the macerated food is filtered by the pylorus before excretion in the midgut. The pyloric and gastric CPG networks drive muscle contractions of the pylorus and gastric mill, respectively.

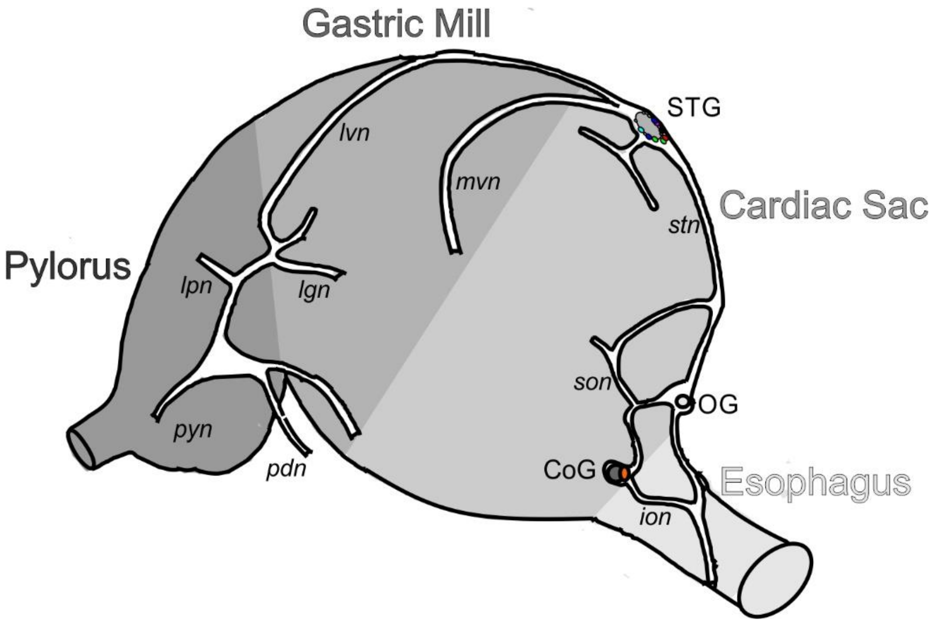

Figure 1.2 The stomatogastric nervous system (STNS) of decapod crustaceans. The STNS lies on the dorsal surface of the foregut and controls a multi-compartment stomach. There are four main ganglia that comprise the STNS: the oesophageal ganglion (OG), the paired commissural ganglia (CoG) and the stomatogastric ganglion (STG). The COGs and OG are connected to the STG through the stomatogastric nerve (stn). Figure adapted from [16].

The pyloric network produces a rhythmic output in a range of frequencies across individual animals (0.5 to > 2 Hz) but on average is ~1 Hz (Figure 1.3) [17]. The output is characterized by stable oscillations produced by a group of pacemaker neurons. This pacemaker group involves two neuron types, the Anterior Burster (AB) and the Pyloric Dilator (PD), of which there are two copies that are strongly electrically coupled with the AB neuron and with each other and produce synchronized bursting activity. However, only the AB neuron is an intrinsic oscillator [18]. In contrast, the PD neurons only burst due to their strong electrical coupling to the AB neuron and fire repetitive spikes when isolated from AB [18, 19]. In some species, all pyloric neurons are capable of producing bursting [18] in response to external neuromodulatory inputs (see below) to the network [20]. Interestingly, in *C. borealis* this is not the case and only the AB neurons, and the PD neurons when coupled to AB, oscillate in response to neuromodulatory input [21].

The frequency of the pyloric rhythm is mainly set by the frequency of the pacemaker group and its synaptic connections onto pyloric follower neurons. Synchronous bursting in the pacemaker neurons drive two pairs of follower neurons to sequentially fire bursts of action potentials with different onset timings. Of these neurons, the main components necessary for the manifestation of a tri-phasic rhythm are the Lateral Pyloric (LP) and the Pyloric constrictor (PY) neurons. However, only the LP neuron provides chemical synaptic feedback to the pacemaker group. The patterning of the triphasic rhythm depends on the dynamic interaction between synaptic and intrinsic properties. All synaptic connections in the pyloric network are inhibitory and utilize glutamate as the neurotransmitter except for the PD and the ventral dilator (VD) neurons, which use acetylcholine [22].

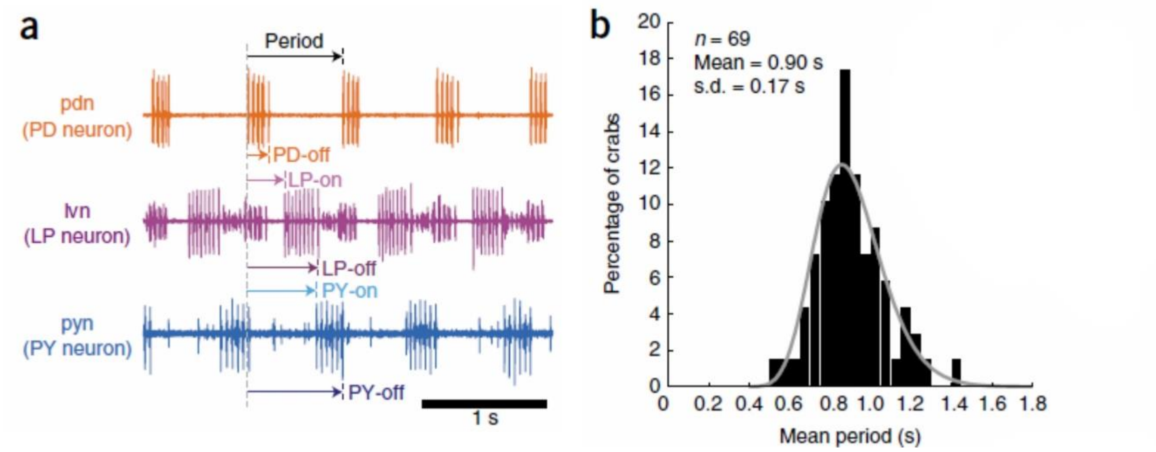

Figure 1.3 Variability of pyloric network cycle period across different animals. a) Typical extracellular recordings of pyloric neurons. Simultaneous recordings made from the pyloric dilator nerve (pdn), lateral ventricular nerve (lvn) and the pyloric nerve (pyn). The large spikes in pdn, lvn, and pyn recordings are from the PD, LP, and PY neurons. The activity phase of these neurons are labeled in a single cycle given by the start of one PD burst to the start of the next PD burst. b) Histogram showing the distribution of the mean pyloric cycle period for 69 animals. Figure modified from [17]

1.2.3 Neuromodulation

The pyloric network is modulated by a multitude of substances including biogenic amines and neuropeptides [10]. These substances reach the network through synaptic release from the modulatory projection neurons originating in anterior ganglia such as the commissural (CoGs) and oesophageal ganglia (OG), or through the bloodstream as circulating hormones [12, 23] (Figure 1.4). However, the importance of neuromodulation is not unique to the pyloric network of the STG; many neuromodulators modify network function underlying different behaviors in various animals. One example is the modulation of locomotor activity produced in spinal cord CPG networks of the rat by serotonin and dopamine [24]. In the pyloric network, neuromodulators strongly influence the frequency and phasing of neurons [25, 26]. Each neuromodulator elicits distinct pyloric network outputs by reconfiguring the properties of neurons and synapses.

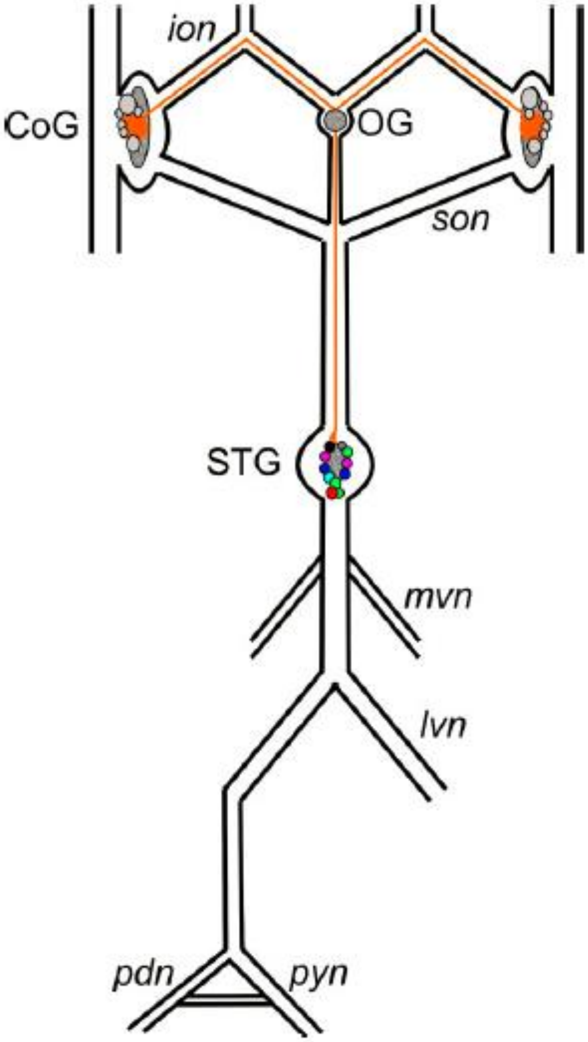

Figure 1.4 The stomatogastric nervous system. The Stomatogastric nervous system is comprised of four ganglia and interconnected nerves. Projection neurons located in the paired commissural ganglia (CoGs) and oesophageal ganglion (OG) provide modulatory inputs to the STG and modify the properties of neurons and synapses within the STG. The stomatogastric nerve serves as the only source of central input to the STG. The individual neurons that belong to the pyloric network are a part of the STG.

Neuromodulation modifies the membrane excitability of individual neuron by modifying the properties of ion channels. In some cases, a single neuromodulator may activate a single ionic channel type [27] or multiple channel types in the same neuron [11]. Furthermore, multiple neuromodulators may converge to activate the same channel type. For example, in the STG, multiple neuropeptides activate the modulatory inward current (I_{MI}) [27, 28], a fast regenerative inward current that promotes oscillatory activity in subsets of pyloric neurons. The activation of I_{MI} induces rhythmic oscillations in the AB and PD pacemaker neurons, but not follower neurons [21]. We examined the effects of the neuropeptide proctolin on the MPR properties of two pyloric neurons, PD and LP. In fact, the MPR properties of neurons in the medial prefrontal cortex and pyloric neurons [29] have been shown to be under the control of neuromodulators [30].

The action of neuromodulators on neurons and networks depends on the prior state and activity. For example, the effect of neuromodulators on networks depends on the activity of those networks [31-33]. In particular, proctolin increases the frequency of the pyloric rhythm when the initial frequency is low, but has little or no effect on frequency when the starting frequency is high [31, 33, 34]. Similarly, the effect of neuromodulators at the single neuron level can also be altered by activity. For instance, the effect of serotonin on the burst generation of R15 neuron of *Aplysia* is influenced by the level of activity [35]. Lastly, similar activity can arise from different combinations of biophysical properties of individual neurons [36, 37]. The effect of a neuromodulator that alters one ionic current may depend not just on the strength of its action but also on properties of other currents in the neuron such that sometimes it produces a large effect and other times no effect at all [38-40].

In this thesis, I examine whether the state-dependent actions of neuromodulation could arise from the addition of novel time-dependent current. Previous work has shown that neuropeptides can activate ionic currents with time-dependent inactivation in a gastric mill neuron [41]. However, the effect of adding a novel time-dependent ionic current to a neuron with variable underlying currents has not been explored. We examine whether the state-dependence of neuromodulators on the activity of follower neurons could arise from the time-dependent inactivation of modulator-activated currents.

1.2.4 Ionic Mechanisms of Membrane Potential Resonance

Neurons are able to generate MPR due to the interaction of active conductances with the passive properties of the membrane [42] (Figure 1.5). The passive properties form a low-pass filter and attenuate voltage response to high frequency inputs. A variety of ionic mechanisms can form a high-pass filter and attenuate responses at low frequencies. Traditionally, the ionic currents are labeled as resonant if they oppose voltage change at low frequencies and activate slowly relative to the membrane time constant. However, the (resonant) negative feedback effect of ionic currents arises from the dynamics of the associated gating variables. A gating variable is resonant if the reversal potential of the associated current lies at the base of the steady-state (in)activation curve for that gating variable and the associated time constant is slow relative to the membrane time constant. Examples of resonant currents are the hyperpolarization-activated inward current (I_{H}) [4, 43] and the M-current, a slowly activating, non-inactivating potassium current [44]. Moreover, since the properties of MPR depend on the voltage- and time-dependent ionic currents, f_{res} will also be voltage-dependent, a property which has been shown in many neuron types [29]. Fast regenerative inward currents provide a positive feedback that favors voltage changes due to the fact that the associated gating variable is fast relative to the membrane time constant and the reversal potential lies at peak of the steady-state activation curve. Examples of amplifying currents are the persistent sodium current [5] and the modulatory inward current (I_{MI}) found in STG neurons [28]. Inactivating currents possess both a fast amplifying activation gate and a slower resonant inactivation gate.

Therefore the classification of the current can be both amplifying and resonating but the effect of the current depends on the interaction between the gating variables. Examples of this type of current include the slowly inactivating low-threshold T-type calcium current [4, 43, 45] and the transient A-type K^+ current [5].

The pyloric pacemaker neurons AB and PD show MPR whose f_{res} (~1 Hz) is correlated with the pyloric network frequency. Pacemaker-driven networks such as the pyloric network contain neurons that produce bursts of action potentials that involve low-threshold activated ionic currents. Often the same low-threshold activated ionic currents that generate bursting also generate MPR. Using pharmacological blockers in the PD neurons, the MPR was found to be sensitive to blockers of both the hyperpolarization-activated inward current (I_{H}) and calcium currents (I_{Ca}) [4].

1.2.5 Variability and correlations

Neurons of the same type express variable ionic current levels across individual animals [46, 47]. The biophysical properties associated with ionic currents are themselves variable, for example, the voltage-dependences and time constants [48]. In spite of this variability, neurons typically exhibit remarkably stable outputs [17, 49, 50].

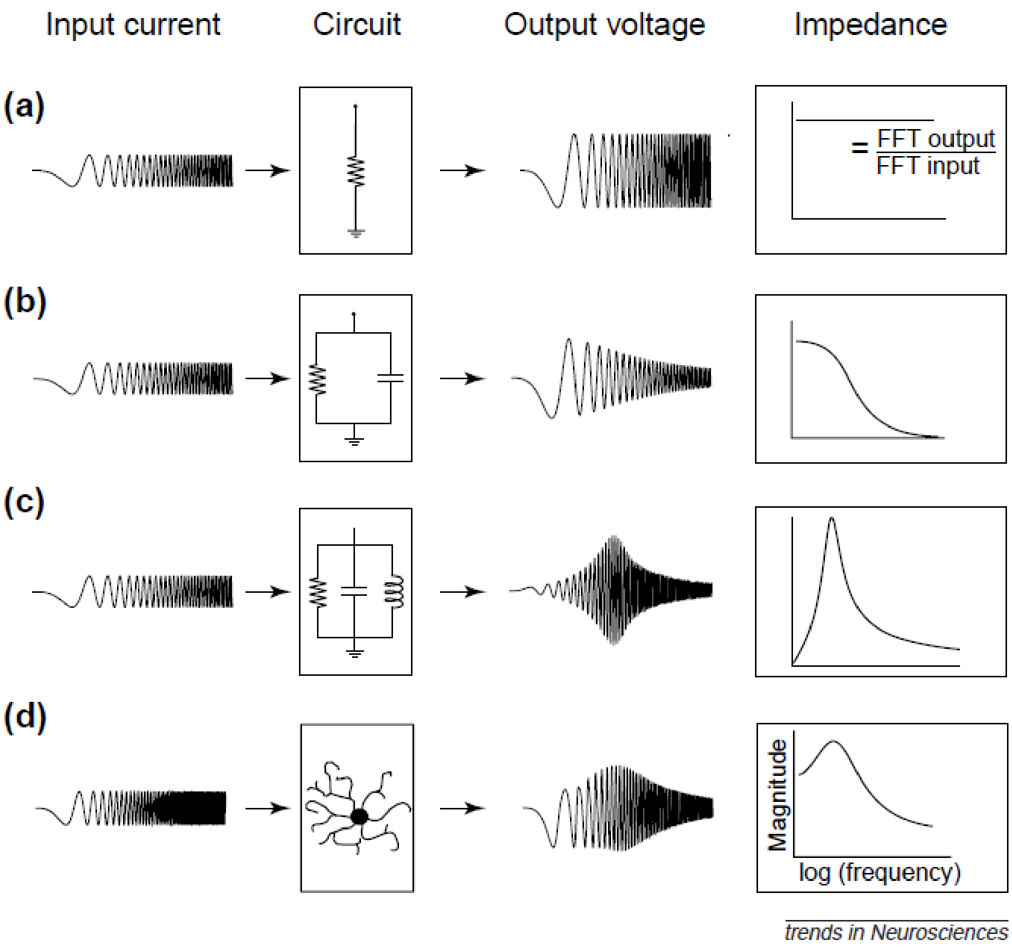

Figure 1.5 Frequency-dependent properties of electrical circuits and neurons. The relationship between the current input current (first column) and the voltage output (third column) of electrical circuits or neurons (second column) enables the calculation of the *Z* profile. The use of the ZAP current injection protocol allows one to probe the response in a specific range of frequencies (*f*). The *Z*-profile is obtained by dividing the Fourier spectrum (obtained from the FFT) of the output by that of the input. a, the voltage response of a simple resistor is just a linear scaling of the input, seen as a constant value in *Z* for all *f* equal to the resistance. b, a resistor and capacitor in parallel is a common model for the passive properties of the neuronal membrane. Values of *Z* decrease for increasing values of *f*, thus acting as a low-pass filter. c, adding an inductive component to the circuit enables the system to behave like a bandpass filter, i.e., produces a resonance peak at nonzero *f*. d, Similar to electrical circuits, neurons can exhibit resonance. Resonant neurons produce maximal outputs when driven with inputs at frequencies near their resonance frequency. Taken from [42].

Variable ion channel properties have been observed in a growing number of systems [47, 48, 51]. This variability has been directly related to their function [52]. For instance, the weakly electric fish electrocytes show a wide range of voltage-dependent activation and inactivation time constants of their sodium and potassium ionic currents across animals [48]. The variability of kinetic parameters correlates with the variability in the frequency of electric organ discharge (EOD) that the animal uses to communicate and navigate. These fish can rapidly change their EOD frequency by modifying the kinetic parameters associated with these currents under different behavioral contexts. This indicates that animals can produce outputs with different combinations of parameters but in a manner that is constrained by the behavioral context. In other systems, such as the pyloric network of the STG, the link between ionic current variability and function is not so clear. In the stomatogastric and cardiac ganglia of the crab *Cancer borealis*, individual neurons shows variable conductance and mRNA levels [47, 53]; however, it has never been shown what feature(s) of activity is (are) determined by the natural variability in ionic current properties across animals.

In many rhythmic networks, including the crab pyloric network [17], gill ventilation [54], leech heartbeat [55] and lamprey swimming [56], the phase relationships of bursting activity in neurons is highly conserved across a population of individual animals. Given that phase is determined by a complex interaction between voltage-gated and synaptic currents, it is possible that these systems have developed biophysical mechanisms to compensate for the variability in the voltage-gated and synaptic currents. interactions between the dynamics of synapses and intrinsic currents can contribute to maintaining phase when frequency changes within an animal [57]. Across individual animals an alternative compensatory mechanism could be utilized to conserve phase, where ionic current properties were coordinately regulated by some common effector [52].

In a number of systems, correlations have been observed between the biophysical properties of single neuron types across different animals. For example, a correlation between K^+ current activation and Na^+ current inactivation kinetics has been reported in electric fish [48]. This correlation may regulate the shape of the EOD by producing compensatory changes in these two parameters. In neurons of the crab pyloric network, there are linear correlations between the maximal conductances of ionic currents [58-60]. One study showed that manipulating the levels of either of two currents that contribute to post-inhibitory rebound in pyloric neurons, the transient K^+ current and the hyperpolarization-activated current, led to compensatory changes in the other current [59]. Thus, such changes in biophysical parameters that have opposing effects on the same activity feature may serve to conserve that feature. However, many correlations between ionic currents have been found but their function is unclear (e.g., I_{Ca} and I_{Na} [61])

MPR in individual neurons can be produced from a variety of ionic mechanisms [42]. The rhythm frequency of the pyloric network is determined by the properties of the pacemakers, of which the PD neuron is a member. The variability in the resonance frequency of PD is correlated with the variability of the pyloric network frequency [4]. I expect to find correlations between the parameters that have opposing effects on the resonance frequency. Furthermore, in a given voltage range, the resonance frequency of the PD neuron is remarkably stable across individual animals [62]. I also expect that the values of biophysical parameters are constrained by the specific values of the MPR attributes. If the MPR is important in determining the supra-threshold neuronal and network activity, then coordinate changes in opposing parameters may be necessary in setting the frequency of such activity. In chapter two, I address the possibility that multiple combinations of parameter values can produce the same MPR, but the MPR attributes are conserved by correlations between pairs of biophysical parameters.

1.3 Outline

There were three separate but inter-related aims of this thesis. The first was to understand the biophysical mechanisms that shape the MPR of neurons. The second was to determine if there is a functional role of antiresonance in shaping the activity of individual neurons and networks. The third and final aim was to examine the frequency-dependent actions of neuromodulation.

The results of this thesis are divided into three Chapters. In Chapter 2, using a combined experimental and computational approach, we examine how the PD neuron generates MPR through a set of interacting resonant currents. We found that relationships among variable parameters determine MPR attributes. Furthermore, we linked the peak phase of individual currents to their amplitude to give a mechanistic explanation of the effect of the calcium current time constants on f_{res}. Chapter 3 is dedicated to the differential effects of proctolin on the Z-profile of the PD and LP neurons and the functional consequences for network activity. Chapter 4 focuses on the state-dependent actions of proctolin on the burst onset phase and duty cycle of a follower neuron. This state-dependence of the effect on follower neuron activity is dictated by the time-dependent properties of an inactivating inward current expressed in that neuron.

This dissertation demonstrated that despite the variability in individual ionic currents of distinct neuron types, stable MPR can be generated in a variety of ways but correlated changes in parameters associated with the ionic currents (activated in the relevant voltage range) set features of MPR. For MPR measured in voltage clamp, any factor that alters the phase of active ionic currents with respect to the passive current, will shift the resonance frequency. Under the normal voltage range of membrane potential oscillations a weakly activated resonant current may contribute indirectly by constraining the parameters of an inactivating resonant current strongly activated in the relevant voltage range. To produce appropriate shifts in resonance frequency when the membrane potential is hyperpolarized, the maximal conductances of distinct resonant currents must be finely balanced. Factors that hyperpolarize the voltage or neuromodulators that would make the voltage range of distinct ionic currents overlap are expected to change MPR and modify the interaction of multiple resonant currents. This dissertation also demonstrated that the effect of neuromodulators on MPR in individual neuron types depends on the type of ionic currents and their nonlinear interaction. In some cases, neuromodulators induce antiresonance. Using linear models, antiresonance was shown to amplify MPR of other neurons and decrease the feedback effect on the frequency of an oscillator neuron through reciprocal inhibitory connections (chapter 3). We concluded by showing that the action of neuromodulators on the activity of a neuron is not fixed but depends on the frequency of oscillations, which was attributed to the activation of currents with time-dependent properties.

CHAPTER 2

MECHANISMS OF GENERATION OF MEMBRANE POTENTIAL RESONANCE IN A NEURON WITH MULTIPLE RESONANT IONIC CURRENTS

2.1 Introduction

Neuronal network oscillations at characteristic frequency bands emerge from the coordinated activity of the participating neurons. The response of a neuron to oscillatory inputs can be characterized by the so-called impedance (Z) and phase (ϕ) profiles [42]. Membrane potential resonance (MPR) is defined as the ability of neurons to exhibit a peak in their voltage response to oscillatory current inputs at a particular (preferred or resonant) frequency (f_{res}) [42]. MPR has been observed in many neuron types such as those in the hippocampus [6, 63, 64] and entorhinal cortex [6, 63-66], inferior olive [67, 68], thalamus [69] , striatum [70, 71], as well as in invertebrate oscillatory networks such as the pyloric network of the crustacean stomatogastric ganglion (STG) [4, 29, 62]. Neurons may also exhibit phasonance (i.e., a zero-phase response), which describes their ability to synchronize with oscillatory inputs at a preferred phasonant frequency ($f_{\phi} = 0$) [7, 43, 64, 72, 73]. Resonance, phasonance and intrinsic oscillations are related, but are different phenomena as one or more of them may be present in the absence of the others [7, 43, 73].

Resonant and phasonant frequencies result from a combination of low- and high-pass filter mechanisms produced by the interplay of the neuron's passive properties and one or more ionic currents and their interaction with the oscillatory inputs [7, 42, 73, 74]. The slow resonant currents (or currents having resonant gating variables) oppose voltage changes and act as high-pass filters. . They include the hyperpolarization-activated inward current (I_H) and the slow outward potassium current (I_M) found in pyramidal neurons of CA1 hippocampus, pyramidal neurons of guinea pig frontal cortex, and layer 2 stellate cell of entorhinal cortex[44, 63, 65]. On the other hand, the fast amplifying currents (or currents having amplifying gating variables) favor voltage changes and can make MPR more pronounced. They include the persistent sodium current (I_{NaP}) and the inward rectifying potassium (I_{Kir}) current. Most previous systematic mechanistic studies have primarily examined models with one resonant and one amplifying current, such as I_{H} and I_{NaP}, respectively [7, 73-75]. Currents having both activating and inactivating gating variables (in a multiplicative way) such as the low-threshold calcium current (I_{Ca}) are not included in this classification, but they are able to produce resonance by mechanisms that are less understood [43, 45].

Resonant neurons have been implicated in the generation of network oscillations in a given frequency band because the resonant and network frequencies often match up or are correlated. One example is in the hippocampal theta oscillations [76] in which CA1 pyramidal cells exhibit MPR at theta frequencies of 4-8 Hz [6, 63, 64, 77]. Hippocampal interneurons also show MPR in vitro , but at gamma frequencies of 30±50 Hz [6, 64], and gamma oscillations have been found to be particularly robust in network models containing resonant interneurons [2, 78]. Despite speculations that MPR determines the frequency of network rhythms, a causal relationship between f_{res} and the network frequency has only been shown for networks of electrically-coupled neurons [9]. Furthermore, for other networks resonance at the subthreshold level in individual neurons does not necessarily translate to resonance at the spiking/network level even though they fall within the same frequency range [7, 70, 79].

The crab pyloric network produces stable oscillations at a frequency of ~1 Hz, driven by a pacemaker group composed of two neuron types, the anterior burster (AB) and the pyloric dilator (PD), that produce synchronized bursting oscillations through strong electrical-coupling [13]. The PD neuron shows MPR, with f_{res} ~1 Hz that is positively correlated with the pyloric network frequency [4]. Previous work has demonstrated that MPR in this neuron depends on two voltage-gated currents: I_{Ca} and I_H [4]. Ionic current levels in pyloric neurons are highly variable across animals, even in the same cell type [80]. It is therefore unclear how these currents may interact to produce a stable MPR in the PD neuron and whether this variability persists or is increased or decreased in the presence of oscillatory inputs.

Traditionally, MPR is measured by applying a ZAP (chirp) current injection, which is a constant amplitude, sweeping frequency sinusoidal waveform, and recording the amplitude of the voltage response [42, 81]. In some systems, depolarization can increase [44] or decrease [82]) the preferred frequency. Alternatively, resonance is measured by applying ZAP voltage inputs in voltage clamp and recording the amplitude of the total current [62]. Both approaches yield identical results for linear systems, but not necessarily for nonlinear systems. Previous studies from our lab showed that, in the PD neuron, hyperpolarization decreases both f_{res} and network frequencies [62]. Since MPR results from the outcome of the dynamics of voltage-gated ionic currents activated in different voltage ranges, changing the input voltage amplitude is expected to change f_{res} in an input amplitude-dependent manner. This cannot be captured by linear models in which impedance is independent of the input amplitude. To our knowledge, no study has attempted to understand the ionic mechanisms that produce shifts in f_{res} in response to changes in the voltage range.

A previous experimental study has explored the generation of MPR by I_{Ca} in thalamic neurons [45] and modeling studies explored the interaction between I_{Ca} and I_H in hippocampal CA1 pyramidal neurons [43, 72] where the resonant and network frequencies are significantly higher than in the crab pyloric network and the I_{Ca} time constants are smaller. Based on numerical simulations, these investigations have produced important results about the role played the activating and inactivating gating variables and their respective time constants in the generation of MPR and the determination of f_{res}. However, a mechanistic understanding of the effects of the interacting time constants and voltage-dependent inactivation that goes beyond simulations is lacking. An important finding for the CA1 pyramidal neurons is that, for physiological time constants, they exhibit resonance but not phasonance [43]. However, for larger time constants, outside the physiological range for these neurons, they are able to exhibit phasonance. This suggests that PD neurons, which have slower time scale currents, may exhibit resonance and phasonance at comparable frequencies. If so, such a correlation between resonance and phasonance can be used to explain the influence of ionic current parameters on MPR.

Our study has two interconnected goals: (i) to understand how the interplay of multiple resonant gating variables shapes the Z- and φ -profiles (impedance amplitude and phase-shift as a function of input frequency) of a biological PD neuron, and (ii) to understand the many ways in which these interactions can occur to produce the same Z-profile in these neurons. For a neuron behaving linearly, e.g., with small subthreshold inputs, this task is somewhat simplified by the fact that linear components are additive. However, neurons are nonlinear and the nonlinear interaction between ionic currents has been shown to produce unexpected results [43, 73, 74].

To achieve these goals we measured and quantified the Z- and φ -profiles of the PD neuron. We then used a single-compartment conductance-based model of Hodgkin-

Huxley type [83] that included a passive leak and the two voltage-gated currents IH and I_{Ca} to explore what combinations of model parameters can produce the experimentally observed PD neuron *Z*- and φ-profiles. The maximal conductances of ionic currents of neurons in the stomatogastric nervous system vary widely [46, 52, 60]. We therefore assume that the parameters that determine the Z-profile in the PD neuron vary across animals. Thus, instead of searching for a single model that fit the PD neuron Z-profile, we used a genetic algorithm to capture a collection of parameter sets that fit this Z-profile. To achieve such a fit, we defined a set of ten attributes that characterize the PD neuron *Z*-profile (e.g., resonant frequency and amplitude) and used a multi-objective evolutionary algorithm [MOEA, [84]] to obtain a family of models that fit these attributes. We then used this family of optimal models to identify the important biophysical parameters and relationships among these parameters to explain how the PD neuron *Z*-profile is shaped. We show how the fact that the inactivating calcium current peaks at the same phase as the passive properties, in response to sinusoidal inputs, can explain why resonant and phasonant frequencies are equal. We identify significant pairwise parameter-correlations, which selectively set certain attributes of MPR. We show that, in this neuron, I_{H} does not produce MPR but can extend the dynamic range of I_{Ca} parameters mediating MPR. Furthermore, we identify a subset of models that capture the experimental shift in the resonant frequency with changes in lower bound of voltage oscillation. Finally, we exploit the fact that the resonant and phasonant frequencies are equal for the PD neuron to provide a mechanistic understanding of the effects of the I_{Ca} time constants on the resonant frequency by using phase information. Our results provide a mechanistic understanding for a generic class of neurons that exhibit both resonance and phasonance as the result of the interaction between multiplicative gating variables and complement the studies in [43].

2.2 Methods

Electrophysiology. The stomatogastric nervous system of adult male crabs (*Cancer borealis*) was dissected using standard protocols as in previous studies [62]. After dissection, the entire nervous system including the commissural ganglia, the esophageal ganglion, the stomatogastric ganglion (STG) and the nerves connecting these ganglia, and motor nerves were pinned down in a 100mm Petri dish coated with clear silicone gel, Sylgard 186 (Dow Corning). The STG was desheathed to expose the PD neurons for impalement. During the experiment, the dish was perfused with fresh crab saline maintained at 10-13ºC. After impalement with sharp electrodes, the PD neuron was identified by matching intracellular voltage activity with extracellular action potentials on the motor nerves. After identifying the PD neuron with the first electrode, a second electrode was used to impale the same neuron in preparation for two-electrode voltage clamp. Voltage clamp experiments were done in the presence of 10^{-7}M tetrodotoxin (TTX; Biotium) superfusion to remove the neuromodulatory inputs from central projection neurons (decentralization) and to stop spiking activity [29, 62]. Intracellular electrodes were prepared by using the Flaming-Brown micropipette puller (P97; Sutter Instruments) and filled with 0.6M K_2SO_4 and 0.02M KCl. For the microelectrode used for current injection and voltage recording, the resistance was, respectively, 10-15MΩ and 25-35MΩ. Extracellular recording from the motor nerves was carried out using a differential AC amplifier model 1700 (A-M Systems) and intracellular recordings were done with an Axoclamp 2B amplifier (Molecular Devices).

*Measuring the Z-Profile***.** During their ongoing activity, the PD neurons produce bursting oscillations with a frequency of ~1 Hz and slow-wave activity in the range of -60 to -30 mV. Activity in the PD neuron is abolished by decentralization. The decentralized PD neuron shows MPR in response to ZAP current injection when the current drives the PD membrane voltage to oscillate between -60mV and -30mV, which is similar to the slow-wave oscillation amplitude during ongoing activity [4]. The MPR profiles are not significantly different when measured in current clamp and voltage clamp [62] There are also no significant effects of the direction that the frequency is ramped in the ZAP function – sweeping from low to high frequencies gave identical MPR to that obtained when frequency was ramped from high to low [29]. Moreover, the PD neuron f_{res} is not significantly affected by its electrical coupling to the other pyloric neurons, such as the anterior burster (AB) neuron [4]. Since the MPR depends on the dynamics of voltage-gated ionic currents, it will also depend on the range and shape of the voltage oscillation. Therefore, to examine how *Z*-profile in a given voltage range constrains the properties of voltage-gated currents and how factors that affect the voltage range change MPR, we measured the *Z*-profile in voltage clamp [70]. To measure the *Z*-profile, the PD neuron was voltage clamped with a sweeping-frequency sinusoidal impedance amplitude profile (ZAP) function [85] and the injected current was measured [62]. To increase the sampling duration of lower frequencies as compared to the higher ones, a logarithmic ZAP function was used:

$$ZAP(\mathrm{t}) = v_0 + v_1 \sin(2\pi F(t));\; F(t) = f_{lo} t \left(\frac{f_{hi}}{f_{lo}} \right)^{t/T} \tag{2.1}$$

The amplitude of the ZAP function was adjusted to range between -60 and -30 mV (v_0 = -45 mV, v_1 = 15 mV) and the waveform ranged through frequencies of f_{lo} = 0.1Hz to f_{hi} = 4 Hz over a total duration T = 100 s. Each ZAP waveform was preceded by three cycles of sinusoidal input at f_{lo}, which smoothly transitioned into the ZAP waveform. The total waveform duration was therefore 130 s. Impedance is a complex number consisting of amplitude and phase. To measure impedance amplitude, we calculated the ratio of the voltage and current amplitudes as a function of frequency and henceforth impedance amplitude will be referred to as $Z(f)$. To measure $\varphi_Z(f)$, we measured the time difference between the peaks of the voltage clamp ZAP and the measured clamp current. One can also measure $Z(f)$ by taking the ratio of the Fourier transforms of voltage and current. However, spectral leakage, caused by taking the Fourier transform of the ZAP function and the nonlinear response, often resulted in a low signal-to-noise ratio and therefore in inaccurate estimates of impedance. Such cases would lead to less accurate polynomial fits compared to the cycle-to-cycle method described above and we therefore limited our analysis to the cycle-to-cycle method. Because the average Z-profile may not be a realistic representation of a biological neuron, we used the attributes of Z and φ measurements from a single PD neuron as our target. We characterized attributes of Z into five objective functions used for fitting by specifying five points of the profile (Figure 2.1a). These five points were:

- (f_0 , Z_0), where $Z_0 = Z(f_0)$ and $f_0 = 0.1$ Hz,
- (f_{res} , Z_{max}), thereby capturing $Q_Z = Z_{max} - Z_0$,
- (f_1 , $Z(f_1)$) where $f_1 = 4$ Hz,

- The two frequencies at which $Z = Z_0 + Q_Z / 2$. Pinning the profile to these points captures the frequency bandwidth $\Lambda_{1/2}$ which is the frequency range for which $f > Z_0 + Q_Z / 2$.

We also constructed five objective functions to capture the attributes of $\varphi(f)$ at five points (Figure 2.1b):

- $(f_0, \varphi(f_0))$,
- $(f_{\varphi} = 0, 0)$, where $f_{\varphi = 0}$, is the phasonant frequency
- $(f_{\varphi\text{max}}, \varphi_{\text{max}})$ where φ_{max} is the maximum phase advance,
- $(f_{\varphi\text{min}}, \varphi_{\text{min}})$ where φ_{min} is the maximum phase delay,
- (2 Hz, $\varphi_{f = 2}$) capturing the phase at 2Hz.

Single-Compartment Modeling. We used a single-compartment biophysical conductance-based model containing only those currents implicated in shaping Z and φ [4]. We performed simulations in voltage clamp and measured the current as:

$$I_{clamp} = I_{Cm} + I_L + I_{Ca} + I_H \qquad (2.2)$$

where I_{Cm} is the capacitive current ($C\frac{dV}{dt}$ in nA), C_m is set to 1 nF and I_L is the voltage-independent leak current in nA. The voltage-dependent currents I_{curr} (I_{Ca} or I_H) in nA are given by:

$$I_{curr} = \bar{g}_{curr} m_{curr}^{p} h_{curr}^{q} (V - E_{curr}) \qquad (2.3)$$

where V is the ZAP voltage input (see below), m_{curr} is the activation gating variable, h_{curr} is the inactivation gating variable, $\bar{g}_{curr}$ is the maximal conductance in µS, E_{curr} is the reversal potential in mV, and p and q are non-negative integers. For I_{Ca}, $p = 3$ and $q = 1$;

for I_H, $p = 1$ and $q = 0$. The generic equation that governs the dynamics of the gating variables is:

$$\frac{dx}{dt} = \frac{1}{\tau_x}(x_\infty(V) - x) \tag{2.4}$$

where $x = m_{\mathrm{curr}}$ or h_{curr}, and

$$x_\infty(V) = 1/\left[1 + \exp\left(\left(V - V_x\right)/k_x\right)\right] \tag{2.5}$$

The sign of the slope factor (k_{x}) determines whether the sigmoid is an increasing (negative) or decreasing (positive) function of V, and V_{x} is the midpoint of the sigmoid.

A total of eight free model parameters were defined (Table 2.1), which were optimized in light of the objective functions introduced above, to yield a good fit to the Z-profile attributes as described below. The slope factors k_x of the sigmoid functions $m_\infty^{Ca}(V)$, $h_\infty^{Ca}(V)$, and $m_\infty^{h}(V)$ were fixed at -8 mV, 6 mV, and -7 mV, respectively. $V_{1/2}^{H_\infty^m}$ was fixed at -70 mV, using data from experimental measurements in crab [86]. The voltage-dependent time constant for I_H was also taken from to be

$$\tau_m^H / \left[1 + \exp\left(\left(V + 110\right)/-13\right)\right] \tag{2.6}$$

where the range of τ_m^H is given in Table 2.1.

Fitting Models to Experimental Data. Computational neuroscience optimization problems have used a number of methods, such as the brute-force exploration of the parameter space [36] and genetic algorithms [87]. However, the brute-force method is computationally prohibitive for an 8-dimensional model parameter space, which would require potentially very fine sampling to find optimal models [88]. We used an MOEA (evolutionary optimization) to identify optimal sets of model parameters constrained by experimental Z and φ attributes. MOEAs are computationally efficient at handling high-dimensional parameter spaces and other studies have used them to search for parameters constrained by other types of electrophysiological activity [88].

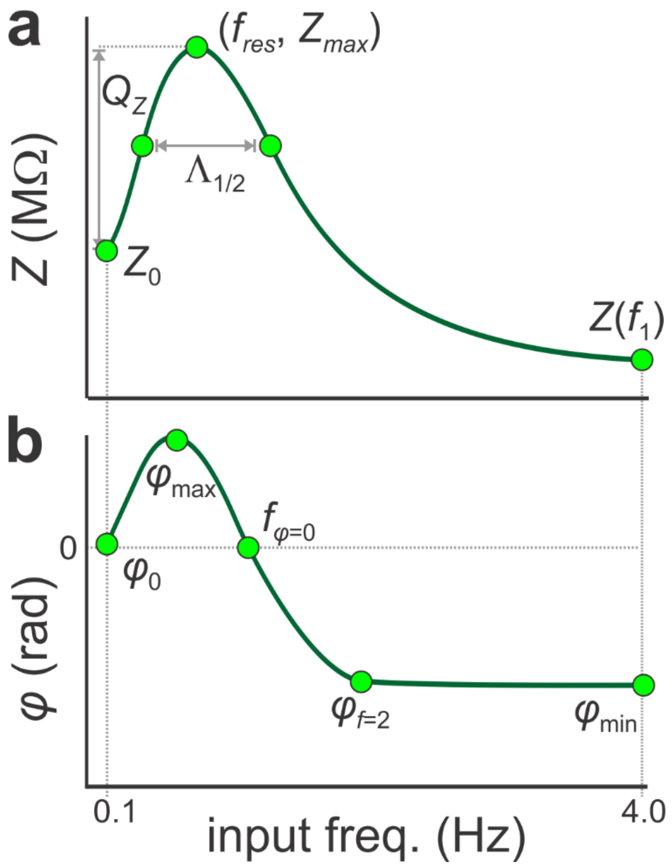

Figure 2.1 Characterization of impedance amplitude $Z(f)$ and phase $\varphi(f)$. The individual objective functions which collectively measure goodness-of-fit were taken as the distance away from characteristic points along the $Z(f)$ and $\varphi(f)$ profiles (green circles). **a.** The attributes used along $Z(f)$ were $Z_0 = Z(f_0)$ at $f_0 = 0.1$ Hz, $Z(f_1)$ at $f_1 = 4$ Hz, maximum impedance $Z_{max} = Z(f_{res})$ and the two points of the profile at $Z_0 + Q_Z/2$. $Q_Z = Z_{max} - Z_0$. $\Lambda_{½}$ is the width of the profile at $Z_0 + Q_Z/2$. **b.** The attributes used along $\varphi(f)$ were $\varphi(f0)$, maximum phase φ_{max}, zero-phase frequency $f(\varphi = 0)$, $\varphi(f=2)$ and $\varphi(f=4)$.

Evolutionary optimization finds solutions by minimizing a set of functions called objective functions, or simply objectives, subject to certain constraints. In our problem, each objective represents the Euclidean distance between the target and the model attributes of Z and φ. When optimizing multiple (potentially conflicting) objectives, MOEA will find a set of solutions that constitute trade-offs in objective scores. For instance, an optimal parameter set may include solutions that are optimal in f_{res} but not in Q_{Z} or vice versa and a range of solutions in between that result from the trade-offs in both objectives. In this paper, we used the non-dominated sorting genetic algorithm II (NSGA-II) [84, 89] to find optimal solutions, which utilizes concepts of non-dominance and elitism, shown to be critical in solving multi-objective optimization problems [89]. Solution x_1 is said to dominate solution x_2 if it is closer to the target $Z(f)$ and $\varphi(f)$ profiles in at least one attribute (e.g., f_{res}) and is no worse in any other attributes (e.g., Q_{Z} , Z_0 , etc.).

NSGA-II begins with a population of 100 parameter combinations created at random within pre-determined lower and upper limits (Table 2.1). The objective values for each parameter combination are calculated and ordered according to dominance. First, the highest rank is assigned to all of the non-dominated, trade-off solutions. From the remaining set of parameters, NSGA-II selects the second set of trade-off solutions. This process continues until there are no more parameter combinations to rank. Genetic operators such as binary tournament selection, crossover, and mutation form a child population. A combination of the parent and child parameter sets form the population used in the next generation of NSGA-II [84, 89]. NSGA-II favors those parameter combinations among solutions non-dominating with respect to one another that come from less crowded parts of the parameter search space (i.e., with fewer similar, in the sense of fitness function values, solutions), thus increasing the diversity of the population. The crowding distance metric is used to promote large spread in the solution space [84].

We ran NSGA-II multiple times (3-5 times, until the mean values of the distributions of optimal parameters were stable) each time for 200 generations with a population size of 100, and pooled the solutions at the end of each run to form a combined population of ~9000 parameter combinations. The algorithm stopped when no additional distinct parameter combinations were found. The Z and φ values associated with the optimal parameter sets match the target features (objectives) defining Z and φ to within 5% accuracy.

To test whether two parameters were significantly correlated in the population of 9000 PD models, we calculated the Pearson's correlation coefficient (R) for each pair of parameters and used a permutation test to determine the significance of R (using a random subset of 20 models). The p-value was given as the fraction of R-values for the permuted vectors greater than the R value for the original data [36]. We also used a t-test to determine whether the calculated slope of the linear fit differed significantly from zero, which gave us identical results.

Sensitivity analysis. We assessed how the values of f_{res} and Q_Z depend on changes in parameter values by performing a sensitivity analysis as in [90]. We split the model parameters into two categories: additive, for the voltage-midpoints of activation and inactivation functions, and multiplicative, for the maximal conductances and time constants. We changed the parameters one at a time and fit the relative change in the resonance attributes as a linear function of the relative parameter change. We changed the multiplicative parameters on a logarithmic scale to characterize parameters with both low and high sensitivity.

Multiplicative parameters were varied as $p_{n+1} = \exp(\pm\Delta p_n)\ p_0$ with $\Delta p_n = 0.001*1.15^n$ and the sign indicating whether the parameter was increased or decreased. To ensure approximate linearity, we added points to the fit until the R^2 value fell below 0.98. The sensitivity was defined as the slope of this linear fit (Figure 2.2). For example, if a resonance attribute has a sensitivity of 1 to a parameter, then a 2-fold change in the parameter results in a 2-fold change in the attribute. We changed additive parameters by ±0.5 mV.

We assessed the sensitivity of f_{res} and Q_{z} to parameter pairs (p_1 and p_2) that were correlated. We first fit a line through the correlated values in the p_1-p_2 space. We then shifted this line to pass through a subset of 50 random points in p_1-p_2 space, resulting in a family of parallel lines, $L^{\parallel}$. For each point, we also produced a line perpendicular to a line $L^{\perp}$. For each model, we performed a sensitivity analysis as before but used the linear fit equation $L^{\parallel}$ or $L^{\perp}$ to calculate the value of p_2. We fit the relative change in the $Z(f)$ attribute as a linear function of the correlated change in p_1 and p_2. We used the slope of the linear fit to represent the sensitivity. We used a 2-and 3-way repeated measures ANOVA and the lsmeans function in R to perform pairwise comparisons of means in testing for significant differences between each group of $\bar{g}_{Ca}$, each direction, $L^{\parallel}$ and $L^{\perp}$, and between each Z attribute, f_{res} and Q_{Z}.

For each model, we solved a system of three differential equations for m_{H}, m_{Ca} and h_{Ca} (voltage was clamped). All simulations were performed using the modified Euler method with a time step of 0.2ms. The simulation code, impedance calculations, and

MOEA were written in C++. MATLAB (The MathWorks) and R were used to perform statistical analyses.

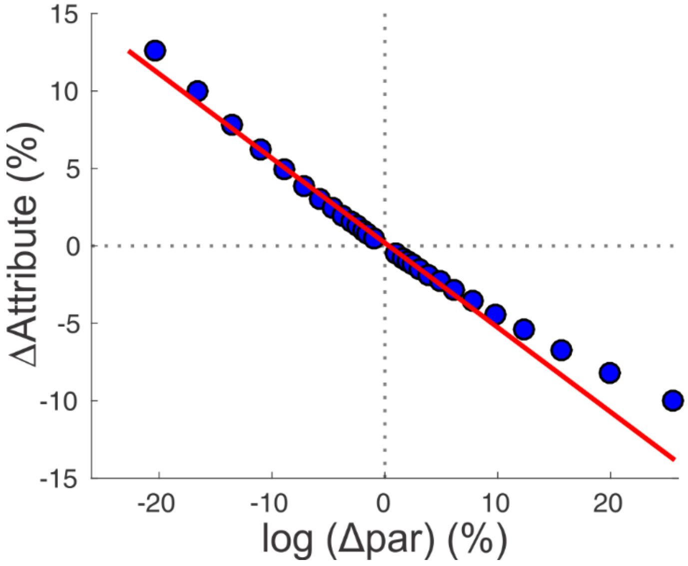

Figure 2.2 Linear fits used to assess the Sensitivity of Impedance Attributes on Changes in Parameters. Each model parameter was changed from the optimal value (origin) in both directions on a logarithmic scale to characterize parameter sensitivity. The slope of a linear fit of the relative change in the *Z*(f) attribute and the parameter was measured as sensitivity. The parameter was changed until the fit was no longer linear (R^2<0.98)

Table 2.1 Limits of Parameter Values Allowed for the PD Neuron Models

	$\bar{g}_L$	$\bar{g}_H$	$\bar{g}_{Ca}$	τ_m^H	$V_{1/2}^{Ca_\infty^m}$	τ_m^{Ca}	$V_{1/2}^{Ca_\infty^h}$	τ_h^{Ca}
Low	0	0	0	0	-75	0	-75	0
High	0.15	0.35	0.35	3000	-30	100	-30	1000

2.3 Results

PD Biological MPR. The PD neuron produces 1 Hz bursting oscillations with a slow-wave approximately -60mV to -30mV (Figure 2.3a). Driving the neuron through this voltage range with a ZAP function in voltage clamp (Figure 2.3b top panel) produces a minimum (arrow in Figure 1b bottom panel) in the amplitude of the current response (Figure 2.3b). The input frequency at which this minimum occurs corresponds to a peak in the Z-profile (f_{res}, Z_{max}; Figure 2.3c1). The value of f_{res} was 0.86 ± 0.05Hz producing Z_{max} values of 10.23 ± 0.51 MΩ (N = 18; Figure 1d). The φ-profile shows a phasonant frequency $f_{\varphi=0}$ = 0.81 ± 0.05Hz, which in most cases matched f_{res} (Figure 2.3c2). The PD neuron had a Q_Z of 2.77 ± 0.71 MΩ and $\Lambda_{1/2}$ of 0.53 ± 0.04 Hz. Across preparations, Q_Z showed considerable variability, whereas f_{res}, $\Lambda_{1/2}$, and $f_{\varphi=0}$ were relatively consistent (Figure 2.3d). The corresponding median values for f_{res}, $Q_{Z,}$ $\Lambda_{1/2}$, and $f_{\varphi=0}$ were 0.83 Hz, 2.77 MΩ, 0.5 Hz, 0.79 Hz, respectively.

To obtain model parameter combinations constrained by the PD neuron Z- and φ -profiles, we generated a population of models using an NSGA-II algorithm (see Methods). The attributes of a single PD neuron Z- and φ -profiles (Figure 2.4), filled red circles) constrained the optimization of the parameter values. This resulted in a population of ~9000 sets of parameters (“optimal” dataset). All models in the optimal dataset captured the attributes of Z and φ to within 5% of the target (light blue lines in Figure 2.4), with the exception of φ_{max}, which may be due to the anatomical structure of the PD neuron, a property that is omitted in our single-compartment model, or due to additional ionic currents, such as the potassium A current, which are not included in our model [43, 91].

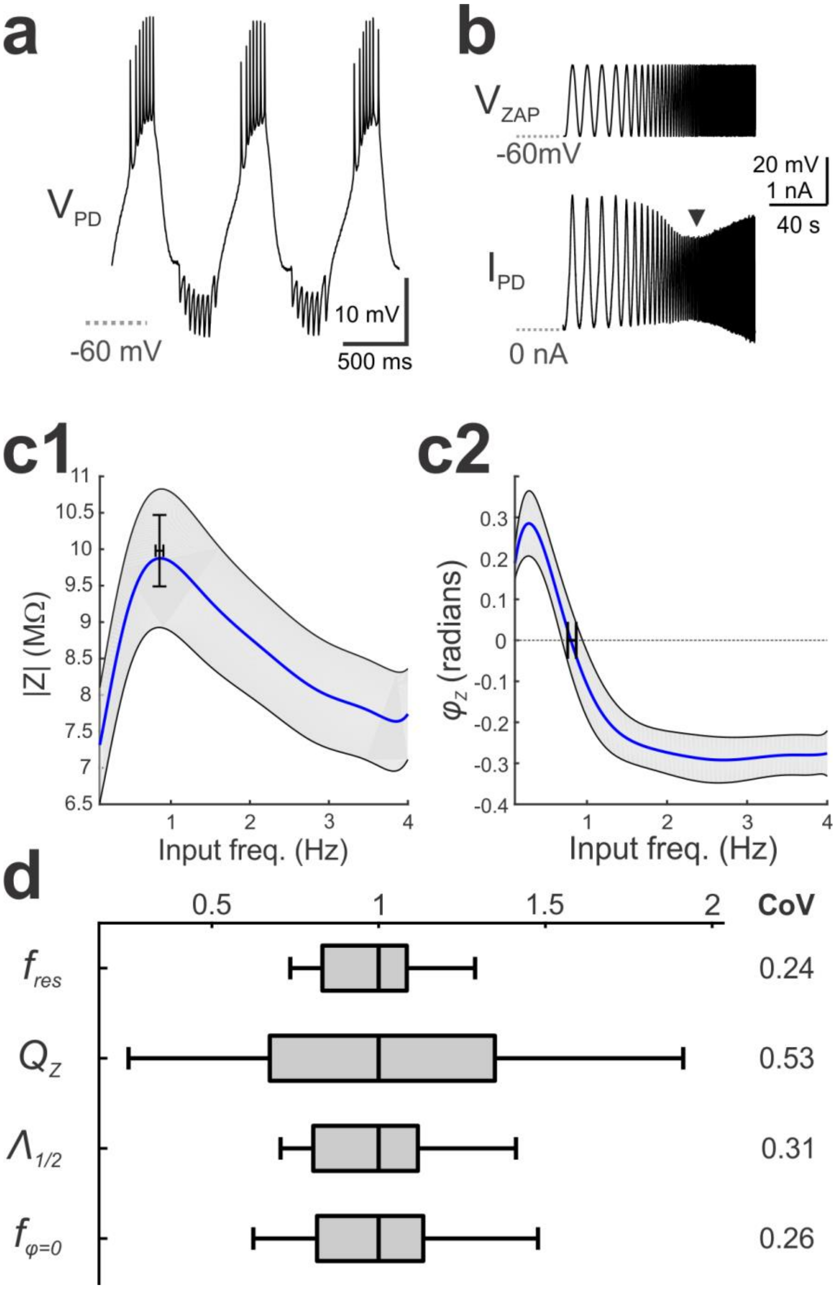

Figure 2.3 MPR of the PD neuron is relatively stable across preparations. a, During ongoing activity, the PD neuron shows a slow-wave voltage waveform ranging approximately between -60 and -30 mV. b, The membrane potential (V_{zap}) and the injected current (I_{PD}) were recorded when the PD neuron was voltage-clamped using a ZAP function between -60 and -30mV and sweeping frequencies between 0.1 and 4 Hz. The arrowhead indicates resonance, where the current amplitude is minimal. c, The Z amplitude profile (c1) and phase φ_Z profile (c2) measured at each frequency of the PD neuron measured in 18 preparations. The cross bars show the mean and SEM of f_{res} and Z_{max} (c1) and $f_{\varphi=0}$ (c2). The shaded region indicates the 95% confidence interval. d, The range of three $Z(f)$ attributes f_{res}, Q_Z, and $\Lambda_{1/2}$ and one $\varphi(f)$ attribute $f_{\varphi=0}$. Each attribute was normalized to the median of its distribution for cross comparison. CoV is the coefficient of variation.

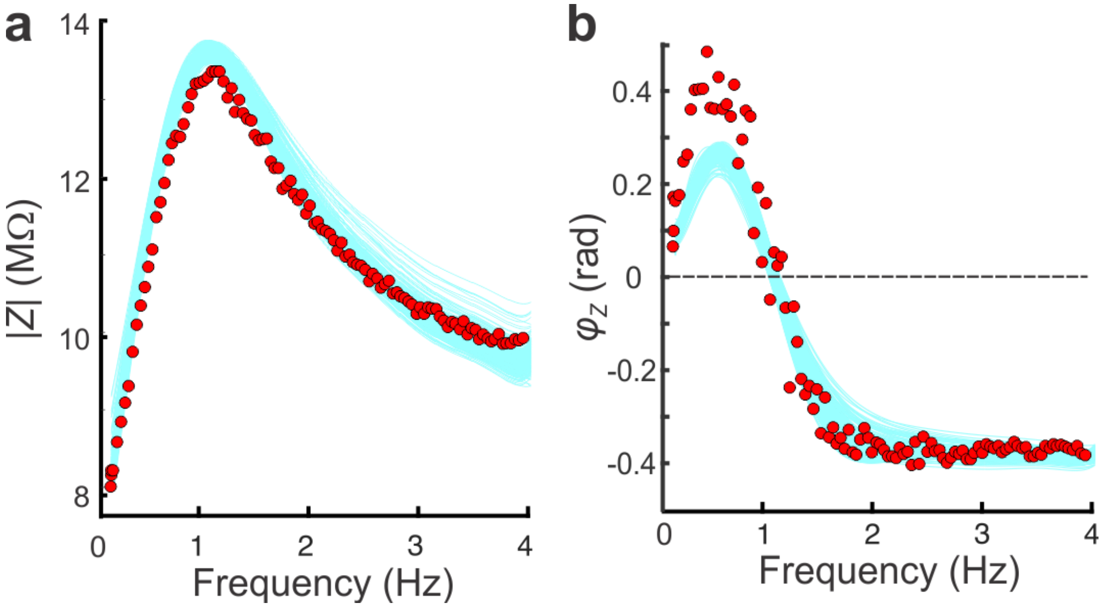

Figure 2.4 Optimal models capture the impedance attributes of a single PD neuron. The *Z*- (a) and *φ*- (b) profiles of 500 randomly selected models from the optimal dataset (light blue curves) are compared to the target neuron's impedance profiles (red circles). All attributes (except φ_{max}) were captured to within 5% accuracy. The values of the biological target impedance amplitude attributes (in Hz, MΩ) were: (f_0, Z_0) = (0.1, 8.2), (f_{res}, Z_{max}) = (1, 13.7), (0.4, 11.65), (2.5, 11.65) and (4, 9.6). The target impedance phase attributes (in Hz, rad) were: (0.1, 0), ($f_{\varphi\text{max}}$, φ_{max}) = (0.4, 0.5), ($f_{\varphi=0}$, 0) = (1.05, 0), (2, -4), ($f_{\varphi\text{min}}$, φ_{min}) = (4, -0.4)

The Generation of MPR by the Interaction of Two Resonant Voltage-gated Currents. To understand how *Z* is generated by the dynamics of individual ionic currents at different voltages and frequencies, we examined the amplitude and kinetics of ionic currents in a representative model. In voltage clamp, *Z* is shaped by active voltage-gated currents, interacting with the passive leak and capacitive currents, in response to the voltage inputs. To understand the contribution of different ionic currents, we measured these currents in response to a constant frequency sine wave voltage inputs (Figure 2.5a inset) using three different frequencies: 0.1 Hz, 1 Hz (f_{res}), and 4 Hz (Figure 2.5). For each of these frequencies, we plotted the steady-state current as a function of voltage (Figure 2.5b-d left) and normalized time (or cycle phase = time x frequency; Figure 2.5b-d right). At 0.1 Hz, the amplitudes of I_{H} and I_{L} + I_{Cm} sets I_{total} at low (~ -60 mV) and high (~ -30 mV) voltages, respectively (Figure 2.5b left). Since I_H deactivation is slow, it also contributes to I_{total} at high voltages (Figure 2.5b right). At 1 Hz (= f_{res}), I_H still sets the minimum of the total current, but, because of its slow kinetics, its steady-state dynamics are mostly linear (Figure 2.5c left). However, now I_{Ca} peaks in phase (Figure 2.5c right) with the passive $I_L + I_{Cm}$ at high voltages, thus producing a smaller I_{total} (magenta bar in Figure 2.5c). The values of I_H at 4 Hz are not much different from 1 Hz (Figure 2.5d). However, I_{Ca} peaks at a much later phase (Figure 2.5d right), which does not allow it to compensate for $I_L + I_{Cm}$ at high voltages, thus resulting in a larger I_{total} (magenta bar in Figure 2.5d). Note that at 1 Hz, the total current peaks at a cycle phase close to 0.5, thus implying that that the f_{res} and $f_{\varphi=0}$ are very close or equal (Figure 2.5c right). Although Figure 2.5 shows the results for only one model in the optimal dataset, these results remain nearly identical for all models in the optimal dataset. The standard deviation of the currents measured, including the total current was never above 0.15 nA over all models. The inset in Figure 2.5c shows one standard deviation around the mean for the data shown in the right panel, calculated for 200 randomly selected models.

An important collective property of the models we found is that the two frequencies, f_{res} and $f_{\varphi=0}$ coincide (Figure 2.6a-b). We analyzed the experimental data, and confirmed that the coincidence of MPR and phasonance frequencies also occurs in the biological system (Figure 2.6b inset). This is typically not the case for neuronal models (and for dynamical systems in general), not even for linear systems [73-75], with the exception of the harmonic oscillator. However, the fact that it occurs in this system, allows us to use the current vs. cycle phase (current-phase) diagrams to understand the dependence of f_{res} and $f_{\varphi=0}$ on the model parameters (Figure 2.6c).

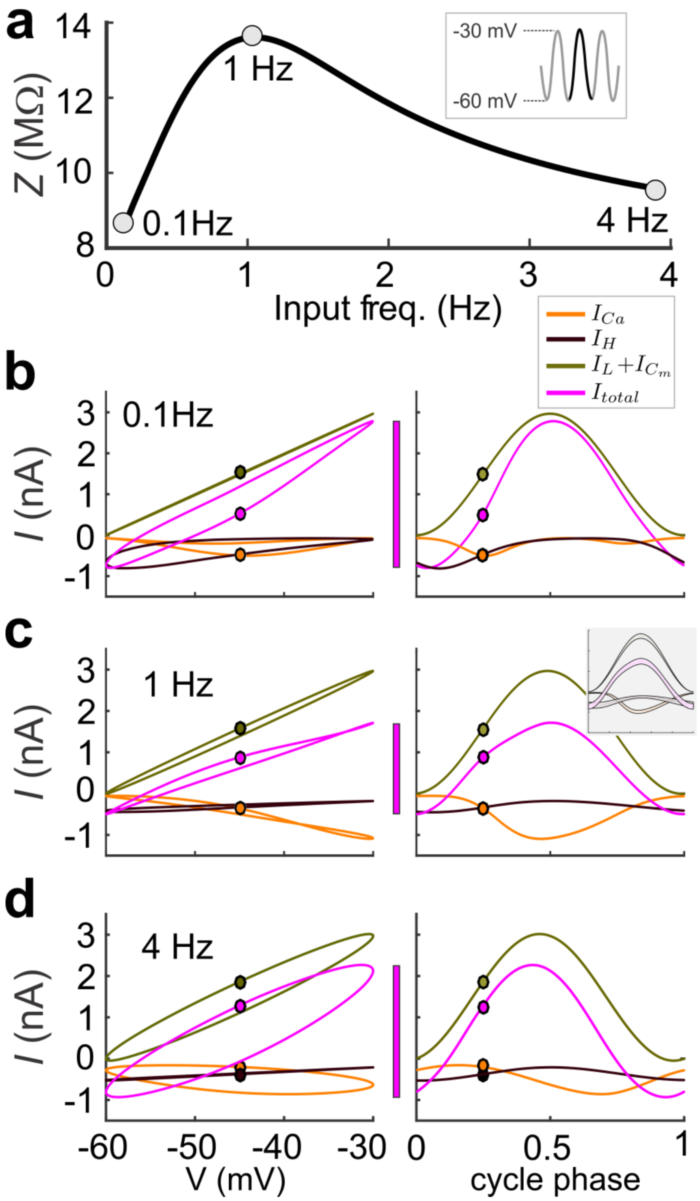

Figure 2.5 Passive and voltage-gated currents contribute to the generation of MPR. (a) *Z*(*f*) for a random model from the optimal dataset. We measured the steady-state response to sinusoidal voltage inputs (inset) at 0.1 Hz, f_{res}=1 Hz, and 4 Hz. Voltage-gated (I_{Ca} and I_{H}) and passive currents (I_{L} + I_{Cm}) are plotted as a function of voltage (left) and normalized time or cycle phase (right) at 0.1 Hz (b), 1 Hz (c), and 4Hz (d). The inset in 5c shows one standard deviation around the mean for the data shown in the right panel, calculated for 200 randomly selected models.

The current-phase diagrams are depicted as in Figure 2.6b-d, as graphs of I_{total}, I_{L} and I_{Ca} as a function of the cycle phase for each given specific input frequency (Figure 2.6c). We do not show I_{H} and I_{Cm} in this plot, because at frequencies near f_{res} they do not change much with input frequency. Note that I_L is independent of the input frequency (five panels in Figure 2.6c) because it precisely tracks the input voltage.

In voltage clamp, $f_{\varphi=0}$ = 1Hz is where I_{total} is at its minimum amplitude exactly at cycle phase 0.5, coinciding with the peak of the input voltage (Figure 2.6c, middle). The fact that I_L precisely tracks the input voltage imposes a constraint on the shapes of I_{Ca} and I_{total}. Therefore, by necessity, if the I_{Ca} trough occurs for a cycle phase below 0.5, the I_{total} peak must occur for a cycle phase above 0.5 (Figure 2.6c, top two panels) and vice versa (Figure 4c, bottom two panels). This is shown by the slope of the line joining the peaks of I_{total} and I_{Ca} and, at f_{res} this line is approximately vertical (Figure 2.6c middle panel).

We use this tool to explain the dependence of the Z-profile on the time constants τ_m^{Ca} (Figure 2.7a) and τ_h^{Ca} (Figure 2.7b). The corresponding current-phase diagrams are presented in figures 2.7c and 2.7d, respectively. In each panel we present the current-phase diagrams for f at 1 Hz (=f_{res} when the parameter is at 100%; middle) and $f = f_{res}$ (sides) when f_{res} is different from 1 Hz.

To understand the dependence of Z on changes in τ_m^{Ca} and τ_h^{Ca} we have to primarily explain the dependence of the two attributes Z_{max} and f_{res} on these parameters. While f_{res} has a similar monotonic dependence on τ_m^{Ca} and τ_h^{Ca} (as these parameters increase, f_{res} decreases), Z_{max} has the opposite dependence on τ_m^{Ca} and τ_h^{Ca}. The opposite dependence of Z_{max} on τ_m^{Ca} and τ_h^{Ca} is a straightforward consequence of the opposite feedback effects (positive for τ_m^{Ca} and negative for τ_h^{Ca}) that these parameters exert on I_{Ca}. An increase in τ_m^{Ca} (for fixed values of τ_h^{Ca}) results in a smaller I_{Ca} in response to a given voltage clamp input. Because I_{Ca} is smaller and negative, this leads to an increase in I_{total}

and a decrease in Z at all frequencies. Similarly, an increase in τ_h^{Ca} (for fixed values of τ_m^{Ca}) results in a larger I_{Ca}, leading to a decrease in I_{total} and an increase in Z.

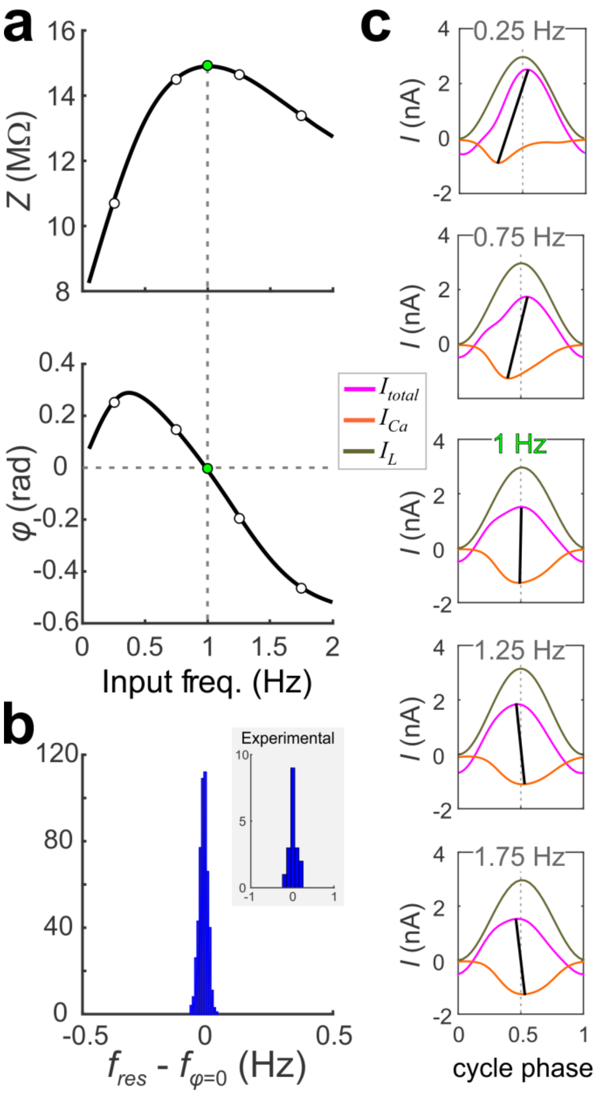

Figure 2.6 The Impedance Attributes f_{res} and $f_{\varphi=0}$ of the optimal models and biological neurons are nearly identical (a) $Z(f)$ (top) and $\varphi(f)$ (bottom) for a representative optimal model. Green dots indicate f_{res} (top) and $f_{\varphi=0}$ (bottom). (b) Histogram showing the difference between f_{res} and $f_{\varphi=0}$ for 500 randomly selected models. A comparison of f_{res} and $f_{\varphi=0}$ of the experimental data of the PD neuron shows a similar distribution (inset, N=18). (c) Plots of steady-state responses of I_{Ca}, I_{L}, and I_{total} to sinusoidal voltage inputs at the frequencies marked in panel a shown as a function of normalized time (cycle phase). Dotted vertical line indicates cycle phase 0.5 where the passive currents peak. Solid lines connect the minimum of I_{Ca} to the peak of I_{total}. The two lines nearly align at $f_{\varphi=0}$.

For a fixed value of the input frequency f (e.g. f = 1 Hz as in Figure 2.7), for Z_{max} to decrease as τ_m^{Ca} increases (Figure 2.7-a), the cycle phase of peak I_{Ca} is delayed thereby subtracting less from I_{L} on the depolarizing phase. This leads to I_{total} to phase advance relative to I_{L} (Figure 2.7c) and causes f_{res} to decrease. Similarly, for Z_{max} to increase as τ_h^{Ca} increases (Figure 2.7b), I_{Ca} has to peak later in the cycle thereby subtracting less from I_{L} on the depolarizing phase, which causes I_{total} to peak earlier in the cycle, which in turn causes the bar also to swing from the left to the right (Figure 2.7d). Therefore, f_{res} decreases.

Parameter Constraints and pairwise Correlations. Previous studies have shown that stable network output can be produced by widely variable ion channel and synaptic parameters [60, 92]. Our biological data, similarly, showed that many of the Z- and φ-profile attributes, such as f_{res}, $\Lambda_{½}$ and $f_{\varphi=0}$ are relatively stable across different PD neurons whereas Q_{Z} shows the most variability (Figure 2.3d). To determine whether the Z- and φ-profile attributes constrain ionic current parameters, we examined the variability of the model parameters in the optimal dataset. We found that some parameters were more constrained while others were widely variable, as measured by the coefficient of variation (CoV; Figure 2.8a). Parameters showing large CoVs were $\bar{g}_{Ca}$, τ_m^h , $\bar{g}_h$, τ_h^{Ca} , and $V_{1/2}^{Ca_\infty^h}$; those showing small CoVs were $\bar{g}_L$ and the time constant of activation of $\mathrm{I_H}$ and $\mathrm{I_{Ca}}$ and half-activation voltage of I_{Ca}: τ_m^{Ca} , $V_{1/2}^{Ca_\infty^m}$, $\bar{g}_L$ (in increasing order of CoV value). A small CoV value implies that the parameter is tightly constrained in order to produce the proper Z- and φ-profiles.

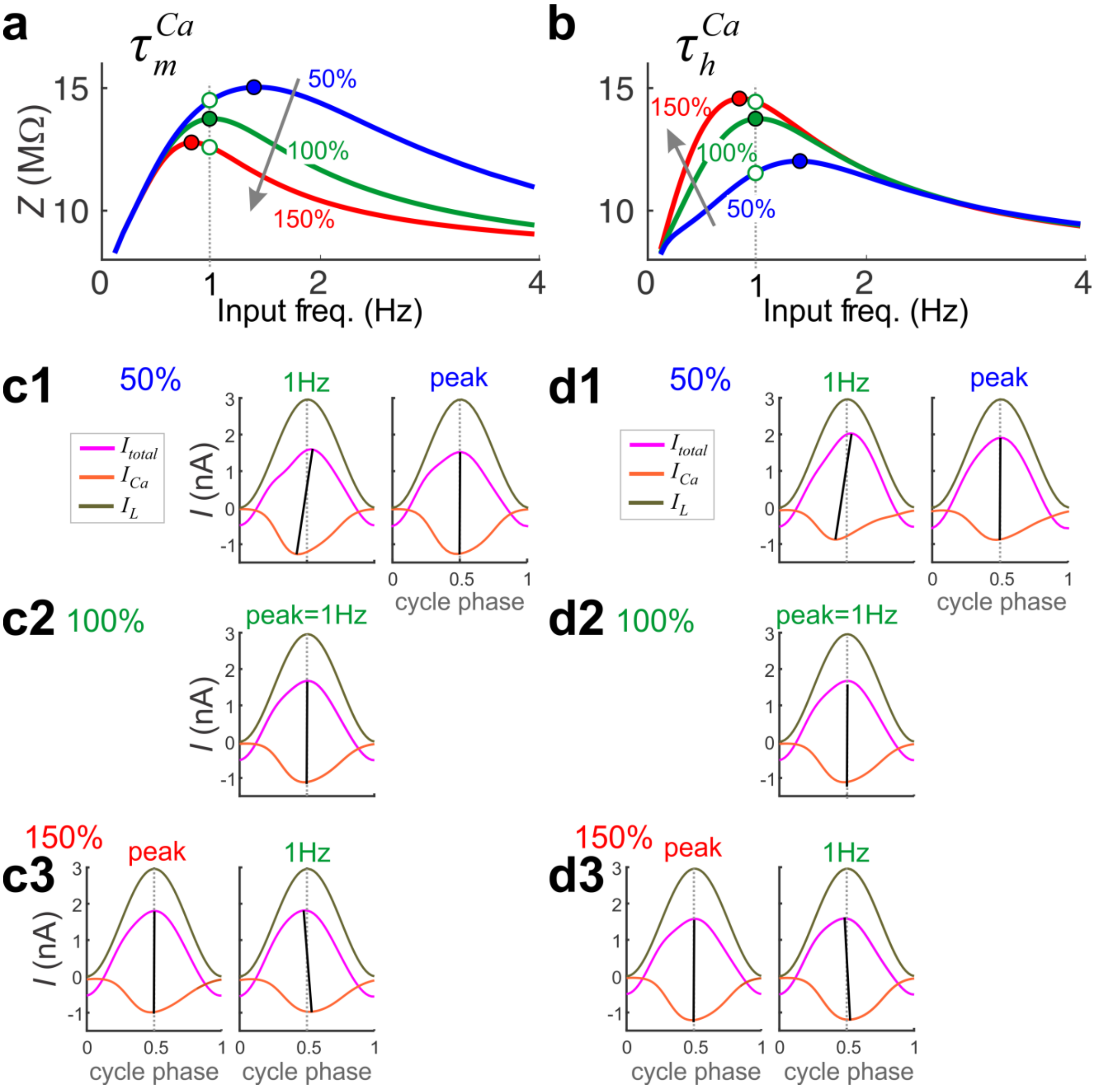

Figure 2.7 The time constants of I_{Ca} activation and inactivation control f_{res} and Z_{max}. The $Z(f)$ profiles are plotted for a randomly selected optimal model (green) at different values of τ_m^{Ca} (a) and τ_h^{Ca} (b). Note that f_{res} of the control (100%) values are at 1 Hz (dashed vertical line). The currents I_{Ca}, I_L and I_{total} plotted as a function of cycle phase at 50% (c1, d1), 100% (c2, d2), and 150% (c3, d3) of the control values of τ_m^{Ca} (c) and τ_h^{Ca} (d). In each panel of c and d, the currents are shown at 1 Hz (along the dashed lines in a, b) and at f_{res} (filled circles in a, b)

A number of studies have indicated that the large variability in ion channel parameters is counter-balanced by paired linear covariation of these parameters [46, 47, 60, 93, 94]. Considering the large variability, we identified parameter pairs that co-varied (Figure 6b). For this, we carried out a permutation test for the Pearson's correlation coefficients, followed by a Student’s t-test on the regression slopes, to identify significant correlations between pairs of parameters (see Methods). The strongest correlations were between the following parameters: $\bar{g}_L$ - $\bar{g}_H$ (r=-0.93), $\bar{g}_L$ - τ_m^{Ca} (R = 0.73), $\bar{g}_L$ - τ_h^{Ca} (R = 0.88), $\bar{g}_H$ - τ_m^{H} (R = 0.68), $\bar{g}_H$ - τ_h^{Ca} (R = -0.82), $\bar{g}_H$ -$V_{1/2}^{Ca_\infty^h}$ (R = 0.76), $\bar{g}_{Ca}$ -$V_{1/2}^{Ca_\infty^h}$ (R = -0.94), and τ_m^{Ca} - τ_h^{Ca} (R = -0.80) (correlations selected with $p < 0.01$; Figure 2.8b).

In our experiments, $V_{1/2}^{H_\infty^m}$ was fixed at -70 mV, using data from experimental measurements in crab [86] (see Methods). However, we also repeated the MOEA with $V_{1/2}^{H_\infty^m}$ set to -96 mV, as reported in lobster experiments [95], and found that all correlations observed with the former value of $V_{1/2}^{H_\infty^m}$ remain intact, but simply with a much larger maximal conductance of I_H (Figure A1). In other words, shifting $V_{1/2}^{H_\infty^m}$ to the left simply results in larger $\bar{g}_H$ in the optimal models without qualitatively changing the other findings.

In particular, we found that the $\bar{g}_{Ca}$ -$V_{1/2}^{Ca_\infty^h}$ correlation appeared nonlinear, but there were strong and distinct linear correlations in the two regions $\bar{g}_{Ca}$ > 0.05μS (low $\bar{g}_{Ca}$) and $\bar{g}_{Ca}$ < 0.05μS (high $\bar{g}_{Ca}$; Figure 2.8c). To ensure that our partitioning of the population into different levels of $\bar{g}_{Ca}$ was valid, we ran the MOEA two additional times, each time using only the mean values of $\bar{g}_L$, τ_m^{H} , $V_{1/2}^{Ca_\infty^m}$, and τ_m^{Ca} for either the low or the high $\bar{g}_{Ca}$ values. These optimal models consistently separated into two non-overlapping model parameters, consistent with the low and high $\bar{g}_{Ca}$ models in Figure 2.8c.

We examined if the low and high $\bar{g}_{Ca}$ models separated or showed distinct correlations in the remaining parameters. The two groups produced non-overlapping subsets of model parameters in the $\bar{g}_{Ca}$-$V_{1/2}^{Ca_{\infty}^{h}}$ graph. We calculated the Pearson's correlation coefficient for each pair of parameters in the low and high $\bar{g}_{Ca}$ groups and tested for significance as before (see Table 2.2). We found that only the high $\bar{g}_{Ca}$ group showed a significant τ_{m}^{Ca} - τ_{h}^{Ca} and $\bar{g}_{H} - \tau_{h}^{Ca}$ correlations (Table 2.2). Additionally, both low and high $\bar{g}_{Ca}$ groups showed the following correlations: $V_{1/2}^{Ca_{\infty}^{h}} - \tau_{h}^{Ca}$, $\bar{g}_{L}$ - $\bar{g}_{H}$, $\bar{g}_{Ca}$-$V_{1/2}^{Ca_{\infty}^{h}}$, and $\bar{g}_{H} - \tau_{m}^{H}$, $\bar{g}_{Ca} - \tau_{h}^{Ca}$. Furthermore, when we ran the MOEA on models where $\bar{g}_{H}$ was set to 0, the only optimal models obtained fell within a narrow range of the high $\bar{g}_{Ca}$ group (Figure A2), which is consistent with the distribution of high $\bar{g}_{Ca}$ models in the $\bar{g}_{H} - \bar{g}_{Ca}$ panel of Figure 2.8d.

Decreasing the Low Bound of Voltage Oscillation Influences the Measured f_{res} and Z_{max}

The lower voltage range of the PD bursting oscillation is strongly influenced by the inhibitory synaptic input from the lateral pyloric neuron (LP), and previous work has shown that f_{res} in the PD neuron is influenced by the minimum of the voltage oscillation (V_{low}) [62]. In order to explore which subset of our optimal models faithfully reproduces the influence of the minimum voltage range, we measured the *Z*-profile when V_{low} was changed from -60 to -70 mV (Figure 2.9a). Decreasing V_{low} significantly decreased f_{res} (by 0.24±0.8Hz), while there was no significant difference in the mean Z_{max} (-0.15±0.81MΩ) (two-way RM-ANOVA; N = 8, $p < 0.001$; Figure 2.9b, left panel).

Table 2.2 Statistical p-values of Pairwise Comparisons for Low and High $\bar{g}_{Ca}$

	$\bar{g}_L$	$\bar{g}_H$	$\bar{g}_{Ca}$	τ_m^H	$V_{1/2}^{Ca_\infty^m}$	τ_m^{Ca}	$V_{1/2}^{Ca_\infty^h}$	τ_h^{Ca}
$\bar{g}_L$		0.003	0.358	0.147	0.272	0.002	0.347	< 0.001
$\bar{g}_H$	0.003		0.288	0.03	0.442	0.104	0.21	0.004
$\bar{g}_{Ca}$	0.349	0.046		0.449	0.512	0.485	<.001	0.129
τ_m^H	0.054	0.001	0.002		0.349	0.470	0.417	0.121
$V_{1/2}^{Ca_\infty^m}$	0.233	0.496	0.138	0.277		0.378	0.452	0.037
τ_m^{Ca}	0.133	0.510	0.191	0.253	0.05		0.318	0.036
$V_{1/2}^{Ca_\infty^h}$	0.368	0.07	<0.001	< 0.001	0.068	0.092		0.27
τ_h^{Ca}	0.307	0.452	0.008	0.05	< 0.001	< 0.001	0.001	

Low $\bar{g}_{Ca}$ shown in lower triangle and high $\bar{g}_{Ca}$ shown in upper triangle

We consequently filtered the full optimal dataset (black dots Figure 2.9c) to find a subset of models that reproduced the change in f_{res} and $Z_{\max}$ (to within 5% of the representative experimental $Z(f)$ shown in Figure 2.9a) when V_{low} was decreased to -70mV. Of the ~9000 models in the population, we found ~1000 models that produced the desired change. Interestingly, the resulting models showed a trade-off in values for $\bar{g}_{Ca}$ and $V_{1/2}^{Ca_\infty^h}$ parameters that showed little overlap with the low and high $\bar{g}_{Ca}$ model groups (Figure 2.9c).

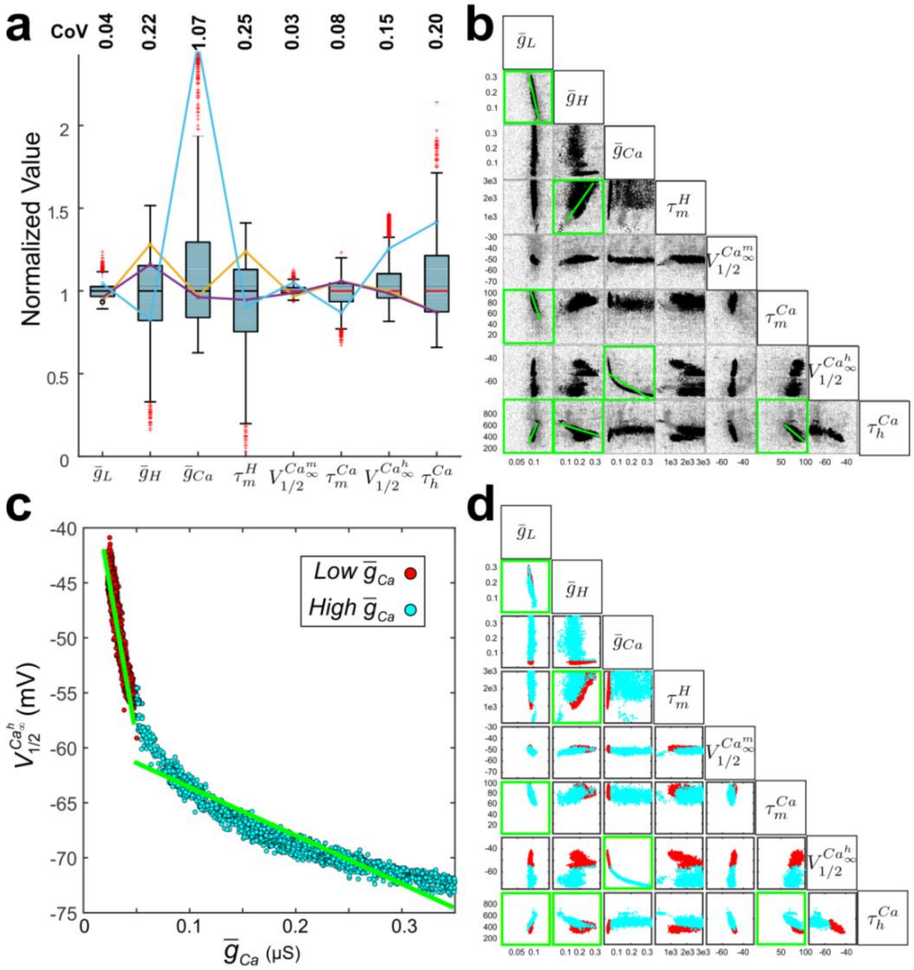

Figure 2.8 The optimal models show variability in individual and pairs of parameters. a, The range of parameters for all optimal models (~9000). Each parameter is normalized by its median value for cross comparison. The median values were $\bar{g}_L = 0.096\mu S$, $\bar{g}_H = 0.164\mu S$, $\bar{g}_{Ca} = 0.172\mu S$, $\tau_m^h = 2179ms$, $V_{1/2}^{Ca_m^\infty} = -51mV$, $\tau_m^{Ca} = 70ms$, $V_{1/2}^{Ca_h^\infty} = -67mV$, $\tau_h^{Ca} = 458ms$. Three representative optimal model parameter sets are shown (cyan, orange, purple solid line segments) indicating that widely different parameter combinations can produce the biological *Z*- and φ-profiles. CoV is coefficient of variation. b, Pairwise relationships among parameters of all optimal models (black dots). The range of parameter space was sampled within the prescribed limits given to the optimization routine, shown by including the sampled non-optimal models (grey). Permutation test showed significant pairwise correlations (green highlighted boxes with linear fits shown as green lines). c, Optimal models could be separated into two highly significant linear fits (green lines) in $\bar{g}_{Ca}$ - $V_{1/2}^{Ca_\infty^h}$ according to whether $\bar{g}_{Ca} < 0.05$ (red; Low $\bar{g}_{Ca}$) or $\bar{g}_{Ca} > 0.05$ (cyan; High $\bar{g}_{Ca}$). d, All pairwise relationships, separated on the low or high $\bar{g}_{Ca}$ (colors as in panel c). Green boxes are the same as in b.

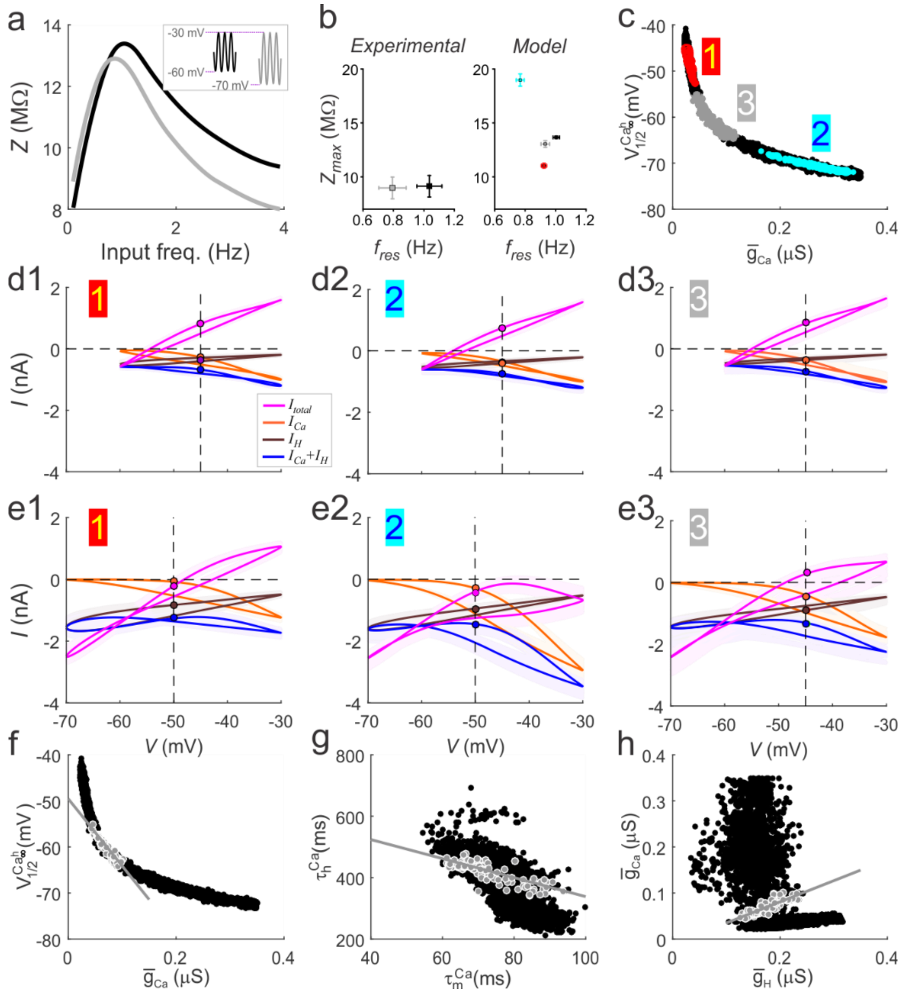

Figure 2.9 The effect of lower voltage bound V_{low} on f_{res} and Z_{max} (a) An example of the change in $Z(f)$ measured in the biological PD neuron for V_{low} =-60mV (black line) and V_{low} =-70mV (grey line). Inset shows the bounds of voltage clamp inputs in the two cases. b. Decreasing V_{low} to -70 mV decreases f_{res} without affecting Z_{max}. (b) Experimental f_{res} and Z_{max} values measured in a random subset of models corresponding to low or high $\bar{g}_{Ca}$ values produced the same f_{res} and Z_{max} values at V_{low} = -60mV (black dots), but distinct f_{res} and Z_{max} values at V_{low} = -70mV (low $\bar{g}_{Ca}$: red dots; high $\bar{g}_{Ca}$: cyan dots). A subset of models shift f_{res} without affecting Z_{max} (grey dots). (c) Different models as seen in $\bar{g}_{Ca}$ -$V_{1/2}^{Ca_\infty^h}$ respond differently to changes in V_{low} (colors correspond to b Model panel). Models depicted by grey dots are referred to as intermediate $\bar{g}_{Ca}$ models. (d1-e3) Average voltage-gated ionic currents I_{Ca}, I_H and $I_{Ca}+I_H$ and I_{total}, shown as a function of voltage for V_{low} =-60 mV (d1-d3) and V_{low} = -70 mV (e1-e3). Numbers are the same as in c. The intermediate $\bar{g}_{Ca}$ models (grey dots) show a strong linear correlation in $\bar{g}_{Ca}$ -$V_{1/2}^{Ca_\infty^h}$ (f) and τ_m^{Ca} - τ_h^{Ca} (g). (h) Intermediate $\bar{g}_{Ca}$ models (grey dots) show a strong $\bar{g}_{Ca}$ - $\bar{g}_H$ linear correlation (black dots).

To understand why this particular group (which we will term intermediate $\bar{g}_{Ca}$) produced small changes in Z_{max} when V_{low} was decreased, we plotted the current-voltage relationships for I_{Ca}, I_H, $I_{Ca}+I_H$ and I_{total} for V_{low} = -60 and -70 mV, measured at f=1Hz (f_{res} at V_{low} = -60mV) and compared these models with the low and high $\bar{g}_{Ca}$ models. For V_{low} =-60mV, the ionic currents behaved similarly for all model groups and I_{total} was maximal at -30mV (magenta curve in Figure 2.9d1-3), indicating the similarity of all models in the optimal dataset. However, when V_{low} was at -70mV revealed differences in peak I_{Ca}, without affecting the peak amplitude of I_H across the different $\bar{g}_{Ca}$ groups (Figure 2.9e1-3). The differences in peak I_{Ca} accounted for most of the changes in I_{total} across the different $\bar{g}_{Ca}$ groups. The Z_{max} values for intermediate $\bar{g}_{Ca}$ models reproduced the small shift seen in experiments because I_{Ca} were at the correct level at high voltages (-30 mV) when V_{low} was at -70mV (Figure 2.9e3). The other two groups did not produce appropriate Z_{max} for V_{low} = -70mV because either I_{Ca} was too small (and hence I_{total} too large), resulting in a smaller Z_{max} (Figure 2.9e1) or vice versa (Figure 2.9e2). It was also clear that the more negative voltages allowed for an increase in I_H levels and therefore larger contribution to the total current. With V_{low} at -70mV, not only was there a larger peak amplitude of I_H at the lower voltages, but the current at positive voltages also increased because of the very slow deactivation rate. Consequently, I_H did not fully turn off when I_{Ca} peaked, so that it also contributes to shaping the upper envelope of the total current. I_H kinetics were also different across the groups (Figure 2.9e1-e3). Taken together with the fact that when I_H was removed produced only parameter values with very high $\bar{g}_{Ca}$ and very low $V_{1/2}^{Ca_\infty^h}$ (Figure A1), these data suggest that I_H could extend the range of I_{Ca} parameters over which MPR could be generated through compensation for variable levels of I_H.

The I_{Ca} in low $\bar{g}_{Ca}$ models was too small when V_{low} was -70 mV, because the low conductance did not allow for a significant contribution from the additional de-inactivation (considering the higher $V_{1/2}^{Ca_\infty^h}$ in this group) and therefore the peak current did not increase enough. Consequently, the contribution of I_H at low voltages was greater than that of I_{Ca} at higher voltages (Figure 2.9e2). Conversely, in the high $\bar{g}_{Ca}$ group, $V_{1/2}^{Ca_\infty^h}$ was more negative and so many more channels were available for de-inactivation and the contribution of I_{Ca} at higher voltages was much larger than that of I_{H} at low voltages (Figure 2.9e3). These findings suggest that the balance between these two currents, that shape the lower and upper envelope of the total current response to voltage inputs, is necessary to produce the appropriate shift in f_{res} without influencing $Z_{\max}$ significantly.

The intermediate $\bar{g}_{Ca}$ models were strongly correlated in $\bar{g}_{Ca}$-$V_{1/2}^{Ca_\infty^h}$ ($R^2 = 0.89$; $p < 0.001$ Figure 2.9f1, and had a stronger correlation in the τ_m^{Ca} - τ_h^{Ca} parameters compared to all models ($R^2 = 0.65$; $p < 0.001$; Figure 2.9g). Limiting the optimal models to the intermediate $\bar{g}_{Ca}$ group also revealed a correlation in the $\bar{g}_{Ca}$ - $\bar{g}_H$ parameters ($R^2 = 0.79$; $p < 0.001$; Figure 2.9h). This new correlation may be produced by the balance of the amplitudes of I_{H} and I_{Ca} at the lower and higher voltages, respectively.

The Impedance Profile Attributes f_{res} and Q_Z are maintained by Distinct Pairwise Correlations. To determine if any of the MPR attributes were sensitive to the correlations, we ran a 2D sensitivity analysis on a random subset of 50 models. We tested for significant difference in sensitivity across low, intermediate and high levels of $\bar{g}_{Ca}$. In particular, we tested for significant sensitivity of f_{res} *and* Q_Z when parameters were co-varied in directions parallel ($L^{\parallel}$) or perpendicular ($L^{\perp}$) to their respective population correlation lines.

We first examined whether f_{res} and Q_Z were sensitive to τ_m^{Ca} - τ_h^{Ca} for both high (Figure 2.10a1), low (Figure 2.10a2), and intermediate $\bar{g}_{Ca}$ (Figure 2.10a3) when parameters were moved along $L^{\parallel}$ and $L^{\perp}$ (blue and green line; Figure 2.10a1-a3). For high and intermediate $\bar{g}_{Ca}$ models, f_{res} sensitivities in the $L^{\parallel}$ group were negative and not significantly different (3-way RM ANOVA; N=50, $p > 0.05$), but both groups were significantly different from the low $\bar{g}_{Ca}$ group (3-way RM ANOVA; N=50, $p < 0.001$), which had a positive sensitivity (Figure 2.10b). This result indicates that the correlation did a better job at maintaining the value of f_{res} when the value of $\bar{g}_{Ca}$ is intermediate or high. For all $\bar{g}_{Ca}$ groups, we found that there was a significant interaction between the Z attribute and direction (2-way RM ANOVA; F(1, 49) = 853.52, $p < 0.001$). When carrying out a pairwise comparison for each direction within an attribute, we found a significant difference in sensitivity between $L^{\parallel}$ and $L^{\perp}$ for f_{res} (t(93.57)=28.251, $p<0.001$). Similarly, for all $\bar{g}_{Ca}$ groups, significant difference in sensitivity between $L^{\parallel}$ and $L^{\perp}$ for Q_Z (t(93.57)=-8.294, $p<0.001$). Because the difference between $L^{\parallel}$ and $L^{\perp}$ for Q_Z was negative, these results suggest that the τ_m^{Ca} - τ_h^{Ca} correlation determines f_{res} and not Q_Z (Figure 2.10b).

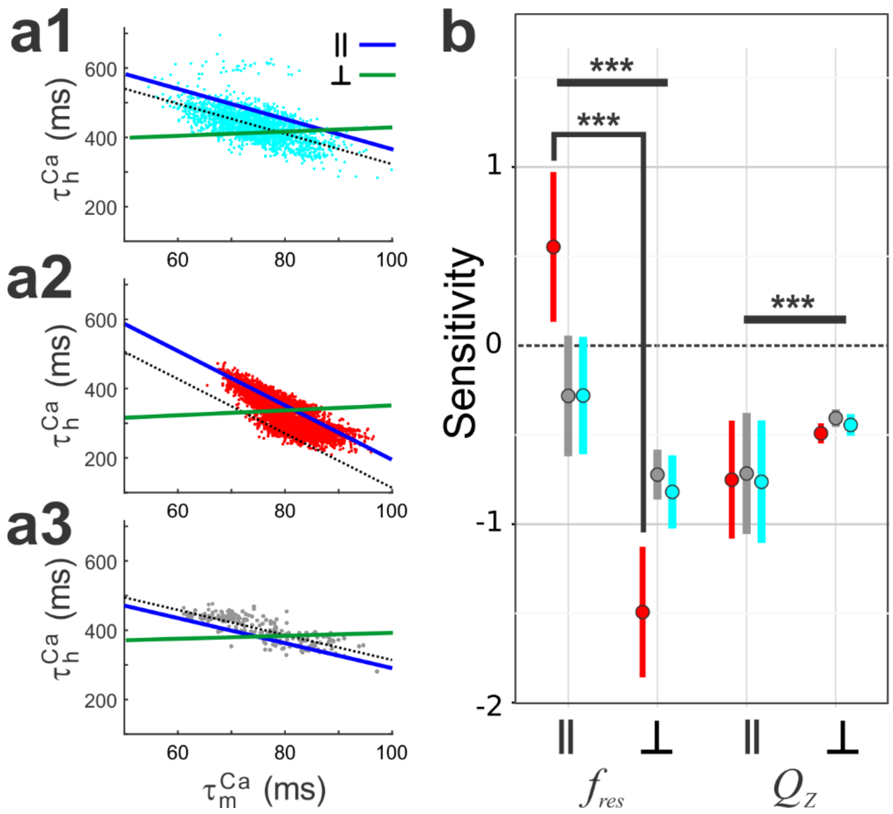

Figure 2.10 Assessing the Dependence of f_{res} and Q_Z on the τ_m^{Ca} - τ_h^{Ca} Linear Correlation.(a) Parameter values for each model were changed along a line parallel (∥, blue) to the correlation line (black) or along a perpendicular line (⊥, green). This was done for models with high (cyan; a1), low (red; a2) and intermediate (grey; a3) $\bar{g}_{Ca}$ models. For each model and each line, ∥ or ⊥, we fit a line to the relative change in either f_{res} or Q_Z as a function of the relative change in $\bar{g}_{Ca}$. (b) The sensitivity values of f_{res} or Q_Z to ∥ or ⊥ are shown for the three groups. Note that on first inspection ⊥ lines do not seem perpendicular, this is because correlated parameters span different data unit lengths along their respective axis. Horizontal bars spanning ∥ and ⊥ indicate that the sensitivity was significantly different between ∥ and ⊥ for all $\bar{g}_{Ca}$ groups.

We next examined whether f_{res} and Q_Z were sensitive to the $\bar{g}_{Ca}$-$V_{1/2}^{Ca_\infty^h}$ correlation for the three model groups (Figure 2.11a1-3). For all $\bar{g}_{Ca}$ groups, we found that there was a significant interaction between the Z attribute and direction (2-way RM ANOVA; F(1, 49) = 1262.73.2, $p < 0.001$). When carrying out a pairwise comparison for each direction within an attribute, we found a significant difference in sensitivity between $L^{\parallel}$ and $L^{\perp}$ for f_{res} (t(95.18)=10.10, $p<0.001$). Similarly, for all $\bar{g}_{Ca}$ groups, we found a significant difference in sensitivity between $L^{\parallel}$ and $L^{\perp}$ for Q_Z (t(95.18)=-35.62, p<0.001). Therefore, these results suggest that the $\bar{g}_{Ca}$-$V_{1/2}^{Ca_\infty^h}$ correlation determines Q_Z and not f_{res} (Figure 2.11b).

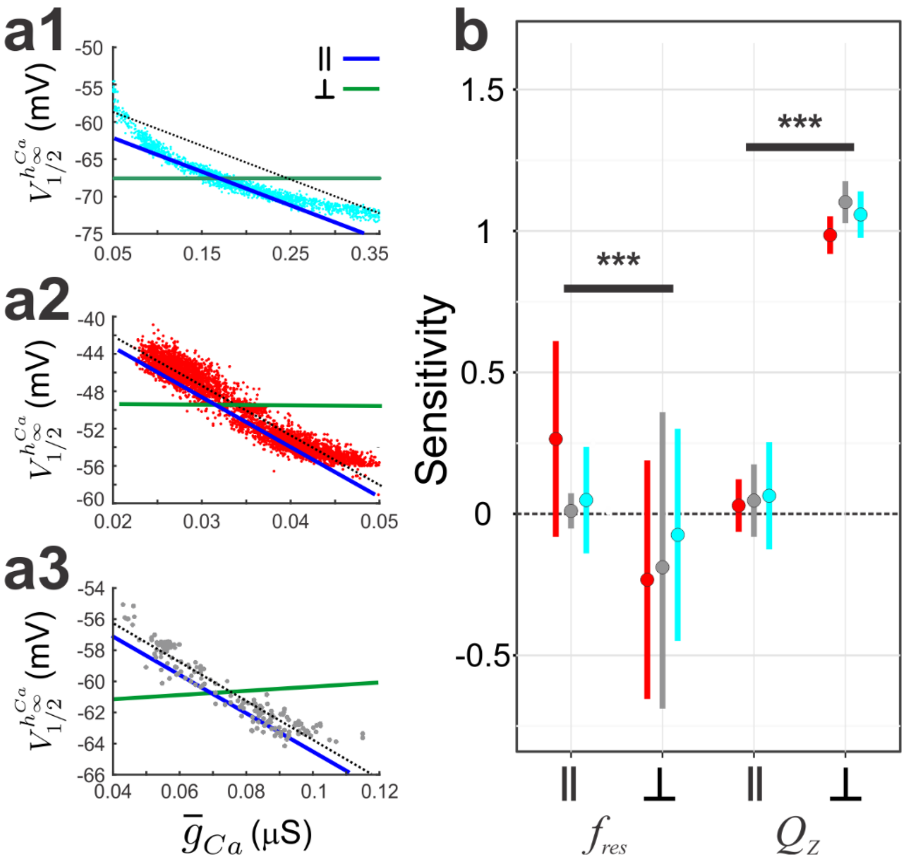

Figure 2.11 Assessing the dependence of f_{res} and Q_Z on the linear $\bar{g}_{Ca}$ - $V_{1/2}^{Ca_h^\infty}$ correlation (a) Parameter values for each model were changed along a line parallel (∥, blue) to the correlation line (black) or along a perpendicular line (⊥, green). This was done for models with high (cyan; a1), low (red; a2) and intermediate (grey; a3) $\bar{g}_{Ca}$ models. For each model and each line, ∥ or ⊥, we fit a line to the relative change in either f_{res} or Q_Z as a function of the relative change in $\bar{g}_{Ca}$ b. The sensitivity values of f_{res} or Q_Z to ∥ or ⊥ are shown for the three groups. Note that on first inspection ⊥ lines do not appear perpendicular because correlated parameters span different data unit lengths along their respective axis. Horizontal bars spanning ∥ and ⊥ indicate that the sensitivity was significantly different between ∥ and ⊥ for all $\bar{g}_{Ca}$ groups.

Finally, we tested the sensitivity of f_{res} and Q_Z to the $\bar{g}_{Ca}$ - $\bar{g}_H$ correlation in the intermediate $\bar{g}_{Ca}$ group (Figure 2.12a). We found that there was a significant interaction between the *Z* attribute and direction (Two-way RM ANOVA; F(1, 11.12) = 2236.2, p < 0.001). When carrying out pairwise comparisons between directions for each attribute, we found there was a significant difference in f_{res} sensitivity between $\mathrm{L}^{\parallel}$ and $\mathrm{L}^{\perp}$ (t(93.93) = 2.65, p = 0.0095; Figure 2.12). Although the sensitivity of Q_{Z} was not 0 for $\mathrm{L}^{\parallel}$, the difference in sensitivity values between $\mathrm{L}^{\parallel}$ and $\mathrm{L}^{\perp}$ was also significantly different (t(93.93) = 62.157, p < 0.0001; Figure 2.12b). These results suggest that, when V_{low} is at -70 mV, for this subset of models to shift f_{res} with only small shifts in Z_{max}, $\bar{g}_{H}$ and $\bar{g}_{Ca}$ values must be balanced. It may be possible that the Q_{Z} sensitivity is not closer to zero along $\mathrm{L}^{\parallel}$ because $V_{1/2}^{Ca_{\infty}^{h}}$, which is also negatively correlated with $\bar{g}_{Ca}$, should decrease too to compensate for changes in $\mathrm{Q_Z}$.

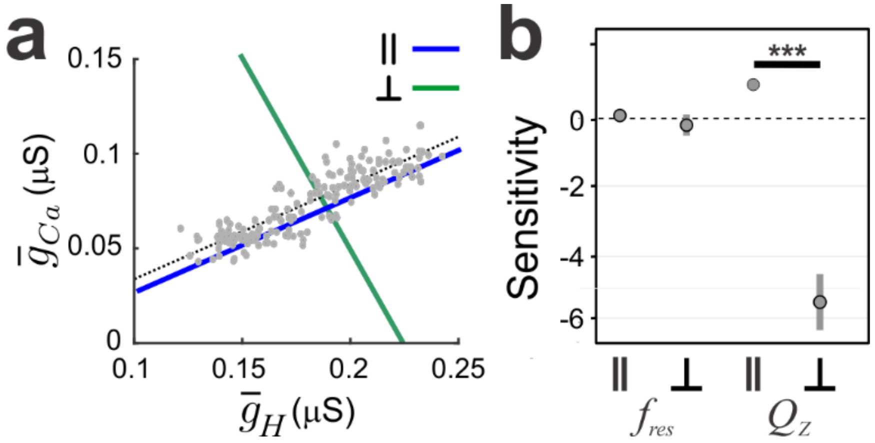

Figure 2.12 Assessing the dependence of f_{res} and Q_{Z} of the intermediate $\bar{g}_{Ca}$ models on the linear $\bar{g}_{Ca}$ - $\bar{g}_{H}$ correlation (a) Parameter values for each model were in the intermediate $\bar{g}_{Ca}$ group (see fig 7) were changed along a line parallel (‖, blue) to the correlation line (black) or along a perpendicular line (⊥, green). For each model and each line, ‖ or ⊥, we fit a line to the relative change in either f_{res} or Q_{Z} as a function of the relative change in $\bar{g}_{Ca}$. (b) The sensitivity values of f_{res} or Q_{Z} to ‖ or ⊥ are shown for the three groups. c. Impedance profiles showing how Q_{Z} changes when the parameters vary along a line parallel (blue) or perpendicular (grey) to the $\bar{g}_{Ca}$ - $\bar{g}_{H}$ correlation line in one optimal model. Arrows show the direction of the movement of Z_{max} and f_{res} for the change in parameters along ‖ or ⊥.

2.4 Discussion

Many neuron types exhibit membrane potential resonance (MPR) in response to oscillatory inputs. Several studies have shown that the resonant frequency of individual neurons is correlated with the frequency of the network in which they are embedded [4, 9, 62, 63, 66, 96]. Moreover, networks of resonant neurons have been proposed to generate network oscillations with more stable frequency than neurons with low-pass filter properties [2, 78]. In several cases, the underlying nonlinearities and time scales that shape the *Z*-profile also shape specific properties of the spiking activity patterns, thus leading to a link between the subthreshold and supra-threshold voltage responses [79, 97].

Previous work in the crustacean stomatogastric pyloric network has shown that the resonance frequency of the pyloric pacemaker PD neurons is correlated with the pyloric network frequency and is sensitive to blockers of both I_{H} and I_{Ca} [4, 29, 62]. However, it was not clear how these voltage-gated ionic currents and the passive properties could interact to generate MPR in the PD neurons. Previous modeling work showed that these currents participate in the generation of resonance in CA1 pyramidal neurons [43, 72]. However, due to the differences in I_{Ca} time constants, the interaction between its activating and inactivating gating variables did not produce phasonance in CA1 pyramidal neurons, while it does in PD neurons. On a more general level, it is not well understood how the nonlinear properties of ionic currents affect their interplay. Previous studies have shown such interactions may lead to unexpected results, which are not captured by the corresponding linearization [43, 72, 74, 75]. This complexity is expected to increase when two currents with resonant components are involved [43, 98]. We therefore set out to investigate the biophysical mechanism underlying such interactions by using a combined experimental and computational approach, with the biological PD neuron as a case study. The two PD neurons are electrically coupled to the pacemaker anterior burster neuron in the pyloric network and their MPR directly influences the network frequency through this electrical coupling [9]. Consequently, our findings have a direct bearing on how the pyloric network frequency is controlled.

Many studies of biophysical models have explored the parameter space using a brute-force technique, by sampling the parameters on a grid [92, 99]. Although this technique provides a rather exhaustive sampling of the parameter space, using a fine grid on a large number of free parameters could lead to combinatorial explosion and result in a prohibitive number of simulations. On the other hand, a sparse sampling may miss “good” solutions. An MOEA can generate multiple trade-off solutions in a single run and can handle large parameter spaces very well. In contrast to a brute-force approach, the MOEA can potentially cover a much larger range with possibly hundreds of values [84]. One disadvantage of the MOEA is that, as the number of objectives increases, the search may miss a large portion of the parameter space. This occurs because randomly generated members often tend to be just as good as others, which means that the MOEA would run out of room to introduce new solutions in a given generation. To try to overcome this problem, we carefully chose the parameters of the MOEA such as population size, mutation and crossover distribution indices (100, 20 and 20, respectively) and ensured that the sampled population covered the parameter space evenly. Additionally, we ran the MOEA multiple times, each time collecting all the good parameter sets until one has exhausted all regions of the parameter space where good models exist.

In previous work, we and other authors have examined how the additive interaction of ionic currents with resonant and amplifying gating variables shape the Z and φ profiles at both the linear and nonlinear levels of description [7, 44, 66, 73, 75, 82, 100]. However, the role of inactivating currents in the generation of MPR remained unclear. Authors have established that I_{Ca} can generate MPR in the absence of additional ionic currents [45], that the activation variable diminishes the propensity for MPR and the interaction with I_{H} enhances the dynamic range of parameters producing I_{Ca}-mediated resonance [43]. Even so, to date, only a descriptive explanation of how the ionic current parameters affect certain attributes of MPR has been provided, and no study has provided a mechanistic understanding in terms of the parameters of I_{Ca} that go beyond numerical simulations.

Similar to [43], the model we used in this paper involves the interaction between resonant and amplifying components. Specifically, this model includes a calcium current with both activation (amplifying) and inactivation (resonant) gating variables, and an H-current with a single activation (resonant) gate. Since I_{H} and I_{Ca} shape the lower and upper envelopes of the voltage response to current inputs, respectively [4], given the appropriate voltage-dependence and kinetics of the currents both could play equal roles at different voltage ranges. In fact, either I_{Ca} inactivation or I_{H} is capable of producing MPR [45, 63]. For example, In CA1 pyramidal neurons, the differences in Z-profiles are due to the passive properties and the kinetics of I_{H} [64]. It is possible that the kinetic parameters of I_{H} and I_{Ca} are tuned so that they contribute nearly equally to shaping the envelopes of the voltage-clamp current.

By tracking the current response to sinusoidal voltage inputs at various frequencies, we found that the f_{res} and $f_{\varphi=0}$ are driven by the peak phase of $I_{Ca,}$ and that f_{res} and $f_{\varphi=0}$ are nearly equal because of the phase matching of I_{Ca} with I_{L}. This is not always the case for neuronal models, and dynamical systems in general, not even for linear models, except for the harmonic oscillator [73-75]. In fact, as we mentioned above, this is not the case for the I_{Ca} model used in [43], although our results on the I_{Ca} inactivation time constant are consistent with that study. In these models a phase advance for low input frequencies required the presence of I_H. The underlying mechanisms are still under investigation and are beyond the scope of this paper. However, the fact that it occurs allowed us to investigate the dependence of the resonant properties on the biophysical properties, particularly the dependence of f_{res} on the I_{Ca} time constants, using phase information. To date, no other analytical method is available to understand the mechanisms underlying this type of phenomenon in voltage clamp. The tools we developed are applicable to other neuron types for which f_{res} is equal to or has a functional relationship with $f_{\phi=0}$. However, the conditions under which such a functional relationship exists still needs to be investigated.

Linear correlations between biophysical parameters of the same or different currents have been reported [60] and may be important in preserving the activity of the model neuron and its subthreshold impedance profile attributes [94]. Previous studies examined combinations of parameters in populations of multi-compartment conductance-based models fit to electrophysiological data [36, 43] and found only weak pairwise correlations, suggesting that the correlations do not arise from electrophysiological constraints. In contrast, constraining the parameters of the ionic currents found to be essential for MPR in PD neuron by MPR attributes, we observed strong correlations between underlying parameters when the Z and φ were constrained by the experimental data. We found that constraining the model parameters by f_{res} produced a correlation between the values of time constants of I_{Ca} among the population of ~9000 optimal parameter sets. Furthermore, running a 2D sensitivity analysis confirmed that the time constants were constrained so that the effect of making inactivation slower was compensated for by making activation faster to maintain f_{res} constant.

The optimal model parameter sets showed a nonlinear co-variation relationship between the values of $\overline{g}_{Ca}$ and half-inactivation voltage of I_{Ca}. However, the models could be divided into two groups, low and high $\overline{g}_{Ca}$ in each of which this co-variation was close to linear. Interestingly, although I_{Ca} alone was the primary current underlying MPR, in the absence of I_{H} (with $\overline{g}_{H} = 0$) the models were restricted to the high $\overline{g}_{Ca}$ group. A 2D sensitivity analysis showed that co-varying parameters in each group along their respective correlation lines preserved Q_{Z} without affecting f_{res}, indicating that each group requires a distinct change in one parameter to compensate for effects of changes in the other. Local sensitivity analysis showed that changes in $V_{1/2}^{Ca_{\infty}^{h}}$ had opposite effects on f_{res} between high and low $\overline{g}_{Ca}$ groups. Increasing $V_{1/2}^{Ca_{\infty}^{h}}$ decreased f_{res} in high $\overline{g}_{Ca}$ models but increased it in low $\overline{g}_{Ca}$ models. A previous modeling study has found that changes in $V_{1/2}^{Ca_{\infty}^{h}}$ greatly influenced the amplitude of MPR with little effect on post-inhibitory rebound in thalamic neurons [45]. It would be interesting to verify whether the mechanisms that generate MPR overlap with those that contribute to post-inhibitory rebound properties in both model and biological PD neurons.

Previous work in our lab has shown that the voltage range of oscillations significantly affects f_{res} [29]. Here we show that decreasing, V_{low}, from -60 to -70 mV, significantly shifted f_{res} to smaller values without affecting Z_{max}. Within our optimal model parameter sets, we obtained a set of ~1000 models in the intermediate $\overline{g}_{Ca}$ range that produced a similar shift in f_{res} but no change in Z_{max}. Because $\mathrm{V}_{\mathrm{low}}$ greatly affects both I_{Ca} inactivation and I_{H} activation, this indicated a potential interaction between these two currents. In fact, we found that because I_{H} and I_{Ca} are activated preferentially in different voltage ranges, their amplitudes needed to be balanced to keep Z_{max} unchanged when $\mathrm{V}_{\mathrm{low}}$ was decreased. If the ratio of I_{H} to I_{Ca} amplitudes is incorrect, then Z will amplify (for high $\bar{g}_{Ca}$ models) or attenuate (for low $\bar{g}_{Ca}$ models). The intermediate $\bar{g}_{Ca}$ models also showed a stronger τ_m^{Ca} - τ_h^{Ca} correlation, which may be important in matching the phase of I_{Ca} with that of I_{L}. This group also showed a strong $\bar{g}_H - \bar{g}_{Ca}$ correlation, which may provide a mechanism for controlling the changes in I_{H} amplitude at more negative voltage with similar changes in I_{Ca} amplitude at more positive voltages.

In contrast to the findings of Rathour and Narayanan [43], in our optimal models the I_{H} peak amplitude was not different across the groups with different I_{Ca} properties. However, since I_{Ca} and I_{H} are differentially modulated [95, 101], their functional role may overlap when their voltage thresholds and time constants are shifted by neuromodulation. Therefore, we expect that under certain neuromodulatory contexts, I_{H} may play more of an active role in the generation of MPR. A similar effect of two ionic currents on resonance has been observed in the hippocampal pyramidal cells that participate in the theta rhythm, in which two currents, the slow potassium M-current and I_{H}, were found to operate at the depolarized and hyperpolarized membrane potentials respectively to generate theta-resonance [63].

In general, unconstrained variability of ionic current expression in any specific neuron type should lead to great variability in network output. Yet, network output in general, and specifically the output of the crustacean pyloric network is remarkably stable across animals [49, 52, 80]. Our results suggest that in oscillatory networks constraint is provided by tuning different ionic currents in an individual neuron in a way that reduces the variability of the output in response to oscillatory inputs. Although our computational study may provide some insight into how such stability is achieved, it also indicates a need for additional mathematical analysis to elucidate the underlying mechanisms.

CHAPTER 3

BIOPHYSICAL MECHANISMS OF MODULATOR-INDUCED ANTIRESONANCE AND FUNCTIONAL ROLE WITHIN A NETWORK

3.1 Introduction

Network oscillations at different frequencies bands are observed in many brain regions and are thought to be crucial for motor and cognitive behavior [96, 102]. Previous work suggests the frequency of such networks may depend on the preferred frequencies of individual neurons [4, 5, 9]. The response of a neuron to oscillatory inputs can be characterized by the so-called impedance (Z) profile, which is a curve of the impedance amplitude (or simply impedance) as a function of frequency (f) [7, 42, 73]. Neurons exhibit membrane potential resonance (MPR) if they show a maximum in the Z-profile at some nonzero input (resonant) frequency (f_{res}).

In many oscillatory networks, the resonant frequency of single neurons has been shown to correlate with the network frequency of the networks in which they are embedded [1, 4-6, 103]. Networks composed of neurons exhibiting MPR [6, 64, 78] may generate more stable network output [2]. For instance, resonant inhibitory interneurons promote network rhythms with more stable frequency [2]. Furthermore, oscillatory inputs reliably produce spikes at frequencies around the resonance frequency [104]. Moreover oscillatory inputs may enhance or suppress activity in different frequency bands in distinct neuron types, which suggests that external oscillatory inputs may alter the contribution of distinct neurons to network activity in a specific frequency band [6].

MPR arises as a consequence of the interaction between positive and negative feedback effects provided by relatively fast amplifying currents and slower resonant currents [7, 42, 73]. Resonant currents are those that counter voltage change on the slow timescale relative to the membrane time constant, such as the H-current (I_{H}) or a slow outward K^{+} current (I_{M}) [44, 73, 100]. Amplifying currents, which include the persistent sodium current (I_{Nap}), enhance voltage change [5]. Studies using models having only one resonant and one amplifying current have shown that amplifying currents has to be fast relative to the resonant current, and in the limiting case of an instantaneous amplifying current the amplification of the voltage response is the strongest. [8]. Although ionic currents have previously been labeled as resonant or amplifying, this property is a manifestation of the voltage- and time-dependent properties of gating variables.

For 2D linear systems, the Z-profile is either a decreasing function of f (red curve in Figure 3.1A), which represents a low-pass filter, or it can be a non-monotonic graph exhibiting a local maximum Z_{max} at some nonzero frequency, f_{res} (blue curve in Figure 3.1A). In higher dimensional systems, additional currents operating at various time scales may modulate the existing 2D MPR to produce more complex shapes in the Z-profile [7, 8]. When 2D models have an ionic current with an amplifying gating variable with instantaneous activation they produce MPR with a single maximum Z. On the other hand, 3D models with slower amplifying variables (slower than the resonant gating variable) have been shown to produce a minimum Z at low nonzero frequency in addition to a maximum Z at higher frequencies [7, 8] (green curve in Figure 3.1B). We refer to a minimum in the Z-profile at nonzero frequencies as antiresonance [8].

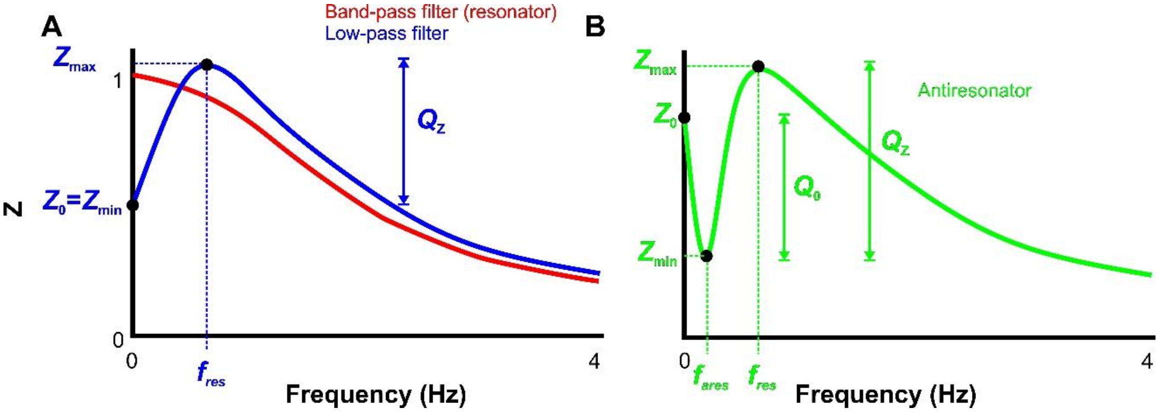

Figure 3.1 Representative Z-profiles (curves of Z vs. input frequency, f) for 2D (A) and 3D (A, B) linear systems. A, Z is characterized by three attributes: the resonance frequency, f_{res}, the maximum Z, Z_{max}, and the resonance amplitude, $Q_Z = Z_{max} - Z_0$. B, Z is characterized by additional attributes: the antiresonance frequency, f_{ares} and the impedance local minimum Z_0. The resonance amplitude is defined as $Q_Z = Z_{max} - Z_{min}$ and it coincides with the definition in panel A when $Z_{min} = Z_0$.

Neuromodulation alters neuronal excitability by modifying the properties of voltage-dependent currents [105]. The neuromodulatory state reflects the behavioral context and determines the expression of MPR [106]. MPR depends on several voltage- and time-dependent ionic currents, which are targets of neuromodulators. For example, norepinephrine modulates I_H [30, 107] and acetylcholine modulates I_M [108]. Any modification of these currents will also affect the MPR [30]. In some cases, neuromodulators may target resonant ionic currents producing shifts in resonance frequency [30] and in other cases it will amplify existing resonances [29]. Another example is seen in the activation of the modulatory-inward current (I_{MI}) by proctolin in the lateral pyloric (LP) neuron of the crab pyloric network [29] (see below). Computational modeling has demonstrated that modulation of resonant currents in the presence of amplifying currents can lead to changes in the resonance frequency and other Z-profile attributes [73, 74]. Additionally, neurons that generate MPR at the same or different resonance frequency with different ionic mechanisms may respond differently to the same neuromodulator.

We examine the hypothesis that neuromodulators produce different responses in distinct neurons types that interact in an oscillatory network. We address this hypothesis using identified neurons and synapses in a reciprocally inhibitory network. The pyloric network in the crustacean stomatogastric ganglion (STG) produces a stable triphasic rhythm (~1 Hz). The output is characterized by stable oscillations produced by a pacemaker group. This pacemaker group involves two neuron types, the Anterior Burster (AB) and the Pyloric Dilator (PD), which are strongly electrically coupled and produce synchronized bursting activity. This pacemaker group drives follower neurons with strong inhibitory synapses [109]. The LP follower neuron provides inhibitory feedback to the PD neurons [18, 110]. The PD neuron exhibits resonance at ~1Hz and is correlated with the network frequency [4]. The LP neuron shows resonance at higher frequencies of ~1.4Hz [29]. Furthermore both the PD and LP neurons respond to the endogenously released peptide neuromodulator proctolin [27].Earlier reports have shown that bath application of proctolin increases the amplitude of MPR in these neurons [29].

We demonstrate experimentally that the neuropeptide proctolin produces differential effects on the *Z*-profiles of PD and LP neurons. Using a nonlinear conductance-based model, we provide a biophysical mechanism to explain the difference in the effects of proctolin on the MPR of these neurons in voltage clamp. These effects are dependent on an increase in I_{Ca}.by proctolin and the interaction with the properties of calcium-dependent K^+ current, I_{KCa}. This approach is justified because peptides have been shown to activate low-threshold inward currents that are voltage-, time- and calcium-dependent in other stomatogastric neuron types in addition to I_{MI} [41]. We show that the differences in the *Z*-profiles, seen in voltage clamped nonlinear models, are reproduced in linear conductance-based models in current clamp. The use of linear models is justified because previous work showed that the response of the model neuron to oscillatory voltage inputs is quasi-linear and voltage clamp and current clamp produce identical f_{res} values for linear systems [111].

Using linearized conductance-based models, we examine the effects of antiresonance in the so-called follower neurons on the network dynamics of a two-cell reciprocal inhibitory network (pacemaker and follower). We demonstrate that the decrease in the voltage amplitude response of the (follower) neuron to feedforward oscillatory synaptic inputs (due to antiresonance) would result in corresponding decreases in the amplitude of feedback inputs. This decrease in feedback input amplitude restricts increases in Z of postsynaptic neurons to frequencies outside the antiresonance frequency range. Finally, we show that antiresonance in response to feedforward inputs from an oscillator neuron produces smaller changes in cycle period of an oscillator neuron cycling in the antiresonance frequency band.

3.2 Methods

Experimental protocols. Adult male crabs (*C. borealis*) were purchased from local seafood markets and stored in tanks filled with artificial seawater at 10-13ºC until use. Crabs were anesthetized by placing them in ice for at least 20 minutes prior to dissection. Dissection was performed following standard procedure [4]. The stomatogastric nervous system – including the commissural ganglia, the esophageal ganglion, the STG and the nerves connecting the ganglia – was pinned down in a 100mm Petri dish coated with clear silicon elastomer Sylgard (Dow Corning). The STG was desheathed to expose the pyloric neurons PD and LP for impalement. During the experiment, the preparation was superfused with normal *Cancer* saline (11 mM KCl, 440 mM NaCl, 13 mM $CaCl_2$, 26 mM $MgCl_2$, 11.2 mM Trizma base, and 5.1 mM maleic acid, pH 7.4 –7.5) at 10-13°C. The PD and LP neurons were identified by matching the spikes in intracellular activity at the cell body with the extracellular spikes as measured on the corresponding motor nerves.

Intracellular recordings were done using Axoclamp 2B amplifiers (Molecular Devices). Intracellular glass electrodes were prepared using a Flaming–Brown micropipette puller (P97; Sutter Instrument) and then filled with the electrode solution (0.6 M K2SO4 and 0.02 M KCl; electrode resistance 15–30). Extracellular recordings from identified motor nerves were obtained using stainless steel wire electrodes, inserted inside and outside of a petroleum jelly well, built to electrically isolate a small section of the nerve. Extracellular recordings were obtained using a differential AC amplifier (A-M Systems 1700).

Logarithmic ZAP function. To examine the properties of the neurons and synapses at a range of frequencies, a ZAP (chirp) function was applied to the presynaptic neuron. This function can be described as follows:

$$Z(t) = B + A\sin(2\pi f(t)), \tag{3.1}$$

where B is the baseline, A is the amplitude, and *f*(t) is a monotonically increasing function that determines the frequency range to be covered. When the ZAP function was applied in voltage clamp, B = V_{low} and A = V_{high} -V_{low} (see next section). To obtain a larger sample set at the lower frequency range, we used a logarithmic ZAP function by setting *f*(t) to be the following:

$$f(t) = F_{beg} t \left(\frac{F_{end}}{F_{beg}} \right)^{t/T} , \tag{3.2}$$

where F_{beg} and F_{end} are the initial and final frequencies in the sweep, and T is its total duration. For the voltage range experiments, we used a frequency range from $F_{\text{beg}} = 0.1$ to $F_{\text{end}} = 4$ Hz

Measurement of membrane potential resonance in the PD and LP neurons. After identifying the neurons, we used 10^{-7}M TTX (Biotium) to block action potentials, which also blocks neuromodulatory release from projection neurons and therefore ongoing oscillations. We used two-electrode voltage clamp to clamp the PD and LP neurons and applied the ZAP function while measuring the injected current. In each sweep, each neuron was clamped at a holding value equal to the minimum of the ZAP function, $V_{\text{low}} = -60$ mV followed by the ZAP function protocol (see above). The voltage range was $V_{\text{low}} = -60$ mV to $V_{\text{high}} = -30$ mV. The *Z*-profiles for the PD and LP neurons were generated in MATLAB (MathWorks) by calculating the ratio of the voltage amplitude to the current amplitude as a function of frequency.

Neuromodulation by proctolin. We examined the effects of the modulatory peptide proctolin on the *Z*-profiles of the PD and LP neurons. Proctolin (American Peptide) was dissolved as a stock solution in distilled water and stored in aliquots of a concentration 10^{-3}M and frozen at -20°C. We used two separate final concentrations of 10^{-7} M and 10^{-6} M, prepared by dissolving the stock solution in *Cancer* saline. Proctolin was perfused for 20 minutes before clamping the neurons with the ZAP function.

Conductance-based models. We used a single-compartment biophysical model containing I_{Ca}, which can independently generate MPR in pyloric neurons [37]. We added I_{KCa} to the model because in experiments it is hard to tease apart the collective roles of I_{Ca} and I_{KCa} in producing MPR. We performed simulations in voltage clamp and measured the current as:

$$I_{clamp} = I_{Cm} + I_L + I_{Ca} + I_{KCa} + I_{MI}\,, \tag{3.3}$$

where I_{Cm} is the capacitive current, I_{L} is the leak current, (all currents are in nA).The currents were computed according to the following equations:

$$\begin{aligned} I_j &= \bar{g}_j m^p h^q (V - E_x) \\ \tau_x \frac{dx}{dt} &= x_\infty(V) - x \end{aligned}\,, \tag{3.4}$$

where V is the membrane potential in mV, the gating variable x represents either m (activation) or h (inactivation), p and q are either 0 or 1, except for I_{Ca}, where p = 3 (see Table 3.1). The exact forms for x_∞ and the time constants are given in Table 3.1.

In the model, we assumed that I_{Ca} and I_{KCa} channels were clustered together, and each cluster was associated with a calcium micro-domain [112]. The diffusion of calcium ions entering through voltage-gated calcium channels is limited by buffers, which spatially restricts calcium changes to small domains. There is no evidence either for or against this hypothesis in the STG, but it is common in other systems [112]. The dynamics of Ca^{2+} were simulated in an average small volume associated with a micro-domain. The equation governing the intracellular calcium concentration C was given by:

$$\frac{dC}{dt} = -\frac{I_{Ca}}{zFv} - \tau_{Ca}(C - C_\infty) \tag{3.5}$$

where C_∞ is the steady-state value of *C* in the absence of I_{Ca} (20μM), τ_{Ca} is the rate of constant of calcium buffering/clearance in /ms. We used 10 ms so that C tracks I_{Ca} closely. Robust activation of I_{KCa} requires values of C > 10 μM and occur only in the vicinity of voltage-gated calcium channels. Fast decay time constants in combination. Therefore, we used a small value (3.5µm^3) for the volume v associated with the each microdomain where calcium increases.

Usually the application of proctolin was simulated by increasing the maximum conductance value of I_{MI}. However, there is evidence that peptides may also target an inactivating inward current that is voltage-, time-, and calcium-dependent [41, 113]. Therefore, we simulated proctolin application by increasing the maximal conductance of the existing I_{Ca} or an increase in the maximum conductance of I_{MI}.

Table 3.1 Equations Governing the Voltage-dependence and Kinetics of Currents in the PD and LP Neuron Models in Voltage-clamp.

		m_∞	τ_m	h_∞	τ_m
I_{Ca}	m^{3}h	$\mathrm{lgc}\left(\frac{v+40}{6}\right)$	60	$\mathrm{lgc}\left(\frac{v+60}{8}\right)$	400
I_{KCa}	mh	$\frac{\mathrm{lgc}\left(\frac{v+10}{13}\right)}{1+\left(C/25\right)^{-5}}$	$500-498\,\mathrm{lgc}\left(\frac{v-\left[-50-x\ln(C/20)\right]}{10}\right)$	$\frac{1}{1+\left(C/7.2\right)^{5/4}}$	12
I_{MI}	m	$\mathrm{lgc}\left(\frac{v+55}{5}\right)$	-	-	-

First column gives the name of the current, second column gives the gating factor, third column gives the steady-state activation, fourth column gives the time constant of activation, fifth column gives the steady-state inactivation, and the sixth column gives the time constant of inactivation. Membrane potential V is in mV, intracellular calcium concentration is C is in µM and the time constants are τ_m and τ_h are in ms. The function lgc(x) is equal to 1/[1+exp(-x)]. For I_{MI}, activation was assumed to be instantaneous.

Synaptically-coupled linear models neurons. Here we refer to a model exhibiting resonance with no antiresonance as a resonator and a model exhibiting both resonance and antiresonance as an antiresonator. Using this terminology, the resonator was modeled as a 2D linear neuron [7, 73]. The antiresonator was modeled as a 4D linear neuron. Although antiresonance can be generated in 3D models (with three variables) [7, 8], we needed to generate antiresonance while matching the values of Z_0 and $Z_{\max}$ of a 2D resonator neuron. We were unable to satisfy these two conditions with a 3D linear model.

$$\begin{aligned} C\frac{dv}{dt} &= -g_L v - \sum_{i=1}^{n} g_i w_i - \bar{g}_{syn} s_\infty(v_{pre})(v - E_{syn}) \\ \tau_i \frac{dw_i}{dt} &= v - w_i \end{aligned} , \tag{3.6}$$

here, $v = V\text{-}v^*$ and $w_\mathrm{i} = W\text{-}w_\mathrm{i}^*$ indicating that the model neuron is linearized around steady state values v* and w* for v and w respectively. For the resonator n =2 and for the antiresonator n = 4. The maximum conductance of the synaptic current is given by $\bar{g}_{syn}$ and the reversal potential is given by E_{syn}. The synaptic activation is a function of the presynaptic voltage and was given by the following Boltzmann equation:

$$1/\left[1+\exp\left(\frac{(V_{pre}-V_{1/2})}{k}\right)\right] , \tag{3.7}$$

where $V_{1/2}$ is the half-activation voltage of the synapse and k is the slope factor. The values of these parameters for each synaptic current are given in Table 3.3. Note, that the synapses used in this study are graded synapses, which are activated at low voltages close to the resting membrane potential and produce a synaptic current which is a smooth function of the presynaptic neuron voltage. This choice was motivated by the fact that the inhibitory chemical synapses in the pyloric network are graded synapses and mediate the interactions between pacemaker and follower neurons [110, 114]. The capacitance was kept fixed at 8nF. The resonator parameters are given in Table 3.2.

Table 3.2. The Parameters of 2D Resonator and 4D Antiresonantor Linear Models

	g_L	g_1	g_2	g_3	τ_1	τ_2	τ_3
Resonator	0.075	0.1	-	-	160	-	-
Antiresonator	0.09	0.12	0.45	0.4885	348	680	1200

Examining the contribution of antiresonance to the shape of Z-profiles through feedback inhibition. To examine the functional role of antiresonance, we connected via reciprocal inhibition a reference resonator (and henceforth referred to as neuron A) to another neuron (henceforth referred to as neuron B) which was either a resonator (identical to A) or an antiresonantor. The synaptic parameters are given in Table 3.3.

Table 3.3 Parameters of Synapses Connecting Linear Resonator and Antiresonator Neurons

	E_{syn}	$V_{1/2}$	k
$A \rightarrow B$	-10	-1	1.25
$B \rightarrow A$	-10	2	4

Extended Morris-Lecar oscillator neurons. We examined the influence of antiresonance in model neuron B on network oscillation frequency through reciprocal inhibitory coupling in a two-cell model network consisting of an oscillator and where neuron B is either a linear resonator or antiresonator. As before, the Z-profile of the linear resonator and antiresonator were nearly equal in their values of Z_0, f_{res}, and Z_{max}. The oscillator was modeled as an extended Morris-Lecar neuron that includes I_H, taken from [9] (see references therein), as described by the following equations:

$$
\begin{aligned}
C_m \frac{dV}{dt} &= I_{app} - I_L - I_{Ca} - I_K - I_H - I_{syn} \\
I_x &= \bar{g}_x m^p h^q (V - E_x) \\
\tau_m \frac{dx}{dt} &= m_\infty(V) - m
\end{aligned}
\tag{3.8}
$$

where V is the membrane potential in mV, C_m is the capacitance in nF, $\bar{g}_x$ and E_x are the maximum conductance (in µS) and reversal potential (in mV) of current I_x (in nA). We used the following parameters adapted from [9]: $\mathrm{C_m} = 1$, E_L =-40, E_Ca = 100, E_K =-80, E_H = -20, $\bar{g}_L$ =0.0001, $\bar{g}_{Ca}$ =0.0025, $\bar{g}_K$ =0.042, $\bar{g}_H$ = 0.025. All currents were modeled as ohmic currents with x = m, p = 1, and q = 0. The associated gating variable equations are given in Table 3.4.

To modify the oscillation frequency of the ML neuron, we used different values of y in the equation for the activation time constant of I_K. We measured the relative change in the cycle period of the ML neuron after it was connected to the linear model as:

$$
\Delta P = \frac{\left(P_{new} - P_{old}\right)}{P_{old}} \tag{3.9}
$$

Table 3.4 Equations Governing the Voltage-dependence and Kinetics of Currents in the Extended Morris-Lecar Model Neuron.

		m_∞	τ_m
I_Ca	m	lgc(v-0/10)	-
I_K	m	lgc(v-0/7.5)	y/cosh(v+0/30)
I_H	m	lgc(v-78/-10.5)	270+1500*lgc(v-42/87)

First column gives the name of the current, second column gives the gating variable, third column gives the steady-state activation, fourth column gives the time constant of activation, Membrane potential V is in mV and the time constant τ_m is in ms. The function lgc(x) is equal to 1/[1+exp(-x)]. The parameter y was used to control the frequency of oscillations.

3.3 Results

Oscillatory networks contain neurons that often exhibit distinct f_{res} values, which has been speculated to shape the activity of individual neurons [6] and to influence the way networks process external oscillatory inputs [2, 50]. Previous work reported that both PD and LP neurons in the crab pyloric network show MPR with distinct values of f_{res} [4, 62]. Moreover, activity in the pyloric network requires the presence of neuromodulators and both neurons respond to the application of proctolin [27]. Proctolin activates I_{MI} with properties similar to the persistent sodium current, which has been shown to contribute to the amplitude of Z-profiles [5].

Proctolin shows differential action on the Z-profiles of the PD and LP neurons. At least for the PD neuron, current clamp and voltage clamp produce identical measurements of f_{res} but voltage clamp allows us to measure MPR by precise control of voltage range and without recruiting high-voltage activated ionic currents [62]. We measured the Z-profiles of the LP and PD neurons by voltage clamping the neuron with a ZAP function sweeping a frequency range from 0.1 Hz – 4 Hz and voltage range from -60 mV to -30 mV (Figure. 3.2). Measurement of the Z-profiles show PD and LP neurons exhibit f_{res} values of ~1 Hz and ~1.4 Hz respectively in control conditions consistent with other studies [29] (Figure 3.2A). We examined the effects of the modulatory peptide proctolin on the Z-profile of LP and PD neurons. Previous studies showed that the MPR amplitude is increased without affecting f_{res} in the LP neuron [29]. Here, we report that the proctolin effect on PD MPR is consistent with previous reports; however, proctolin produced antiresonance in LP.

Figure 3.2A shows an example of the response of the LP and PD neurons to a ZAP function voltage waveform in the presence of 10^{-6} M proctolin. Application of proctolin produced a maximum current at low frequencies of the ZAP voltage waveform and a shift in the minimum current to higher frequencies of the ZAP waveform. In contrast, 10^{-6} M proctolin in the PD neuron produced further decreases in the minimum current without shifting the frequency at which this occurred. These changes are seen more clearly by looking at changes in the Z-profile before and after application of the two concentrations of proctolin (Figure 3.2B). We found that, whereas 10^{-7} M proctolin produced no significant changes in Z_{min} or Z_{max} or their corresponding frequencies, application of 10^{-6} M proctolin significantly shifted f_{min} and f_{max} and significantly decreased Z_{min} and increased Z_{max} respectively ($N = 8$; one-way ANOVA; $p < 0.001$; Figure 3.2C). However, the application of 10^{-6} M proctolin on a representative PD neuron Z-profile had no effect on f_{min} or f_{max} but increased the Z_{max} by ~16%. These results suggest that proctolin produces Z-profile changes in the PD neuron that are consistent with activation of I_{MI}, whereas the changes in the Z-profile of the LP neuron by proctolin are mediated by potentially additional voltage- and time-dependent ionic currents. This suggestion is based on the fact that the modulation of underlying 2D MPR to produce antiresonance involves the addition of at least an ionic current with slow activation gating variable, which contributes a slow amplifying variable in linearized conductance-based models.

Slow I_{MI} reproduces antiresonance inconsistent with proctolin modulation. Proctolin modulation was believed to activate I_{MI}, which is fast and amplifying. Previous theoretical results [8] provided the conditions for the generation of antiresonance in linear conductance-based models, which required a third variable (representing a gating variable). This third variable provides a slow positive feedback that modulates the underlying 2D MPR. To test if the slow activation of I_{MI} - which contributes an amplifying variable in linearized models - could reproduce the effect of proctolin on the Z-profile of the LP neuron, we simulated only I_{Ca}, I_{L}, and I_{Cm} given in eq. (3.3) and summed their responses to a ZAP function as in equations eq. (3.1) and eq. (3.2). We increased the maximal conductance of I_{MI} at various activation time constants. Figure 3.3A shows the effects of increasing the maximal conductance when I_{MI} activation was much faster than the inactivation of I_{Ca}. Increasing conductance strengths amplified the Z-profile (an increase in $Q_{\mathrm{Z}} = Z_{\mathrm{max}} – Z_0$) consistent with the effects of the activation of a fast regenerative inward current on the Z-profile [5]. When the time constant of I_{MI} was equal to that of the inactivation of I_{Ca}, resonance was annihilated as the maximal conductance was increased (Figure 3.3B1).

Just as in [8], the current response at non-zero frequencies was not fast enough to rise above Z_0 and, therefore, $Q_{\mathrm{Z}} = 0$. As the activation time constant of I_{MI} increases above the time constant of I_{Ca} inactivation, antiresonance emerged (Figure 3.3B2). For Z_{max} to be unaffected by increasing values of g_{MI} the activation time constant must be an order of magnitude slower than the inactivation of I_{Ca}. Regardless of this fact, these simulations are consistent with [8] indicating that the interaction between a faster negative feedback (I_{Ca} inactivation) and a slower positive feedback (I_{MI} activation) causes Z to decrease below Z_{max}. However, in contrast to [8], antiresonance in this case is generated because there is an increase in the input resistance and the response is not fast enough to rise above Z_0. The experimental modulation of MPR by proctolin suggest a different mechanism for the generation of antiresonance where Z_0 is unaffected and the response is not fast enough for Z to rise above Z_0 causing a suppression in the response for frequency up to f_{res}. Our results indicate that in the LP neuron, one or potentially multiple currents in addition to I_{MI} must be activated by proctolin to provide both slow positive and negative feedback effects in the neuron.

The time-dependent properties of I_{KCa} are sufficient to capture proctolin-induced antiresonance without I_{MI}. The activation of either fast or slow I_{MI} was not sufficient to capture the type antiresonance in the LP neuron induced by proctolin. Our results suggest, thus far, suggest a combination of additional slow positive and negative feedback effects on the MPR in the LP neuron. We already showed that the activation of fast I_{MI}, which contributes an amplifying variable in linearized conductance-based models, was sufficient to reproduce the proctolin effects on PD MPR. We addressed whether the LP response to proctolin could be explained by the activation of a calcium-dependent K+ current and a calcium current, which together contribute additional slow positive and negative feedback effects on the response to oscillatory inputs.

We used a reduced version of an LP model consisting of a calcium-dependent K^+ (I_{KCa}) current modified from [36] and a calcium current (I_{Ca}) for examination of the proctolin action on the biophysical properties underlying the change in MPR of the LP neuron. Figure 3.4 shows the voltage clamp measurement of the Z-profile of this model. Here proctolin modulation was simulated by either an increase in maximal conductance of I_{Ca} or I_{MI}. Our modeling simulations showed that increasing the maximal conductance of I_{Ca} in the presence of I_{KCa} produced antiresonance. In contrast, increasing the maximal conductance of I_{Ca} in the absence of I_{KCa} resulted in an amplification of MPR through an increase in $Z_{\max}$. Furthermore, increases in the maximum conductances of I_{MI} were insufficient to produce antiresonance. These results suggest that proctolin induces antiresonance by an interaction between I_{Ca} and I_{KCa}.

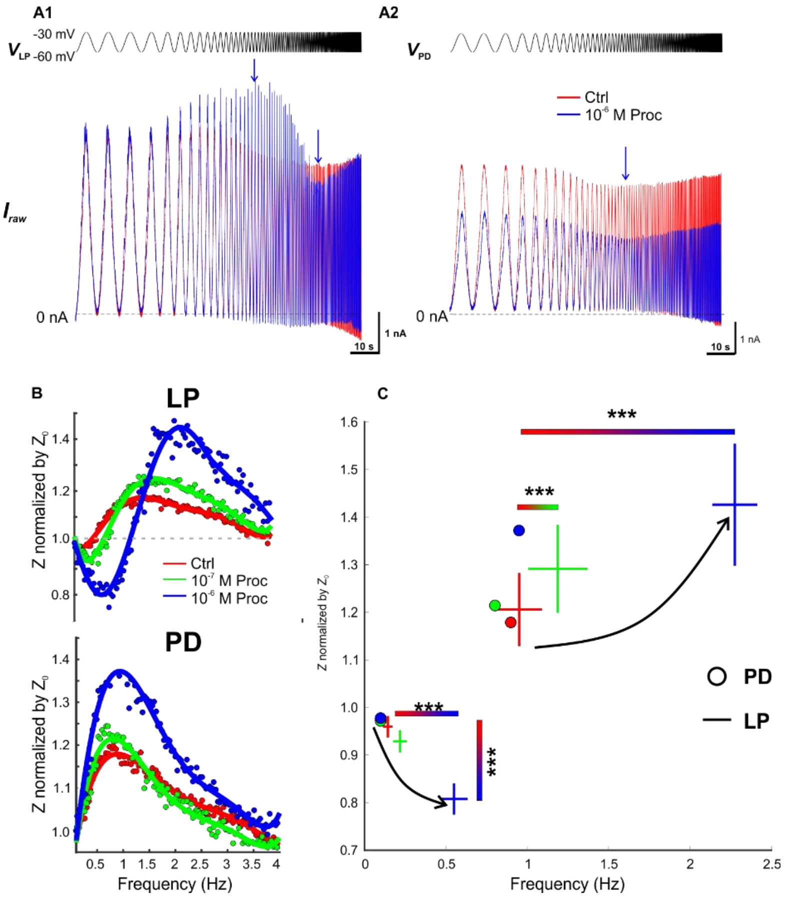

Figure 3.2 The neuropeptide proctolin produces differential effects in the biological neurons PD and LP. A, The biological neurons LP (A1) and PD (A2) were voltage clamped with a ZAP waveform spanning a voltage range of -60 to -30 mV and a frequency of 0.1 – 4 Hz. A1, The neuromodulator proctolin produces a maximum current at a nonzero frequency (antiresonance) and shifts the minimum current (resonance) to higher frequencies in the LP neuron. Vertical blue arrows show the maximum and minimum current in LP during proctolin bath application indicating antiresonance and resonance. A2, The neuromodulator proctolin produces a minimum current at the same nonzero frequency as in control. Vertical arrow indicates the frequency of the minimum current in control and proctolin condition are nearly equal. B, The neuromodulator proctolin produces antiresonance for low concentration (green) and high concentration (blue) seen as a decrease in Z relative to control (red) at low frequencies in LP. In contrast, addition of proctolin does not produce antiresonance in the PD, but only amplifies the maximum Z at f_{res}. C, Average data (mean ± SEM) showing that increasing concentrations of proctolin produce increases in $f_{\min}$ and decreases in $Z_{\min}$, and increases in f_{res} without significantly changing $Z_{\max}$ (N = 8 experiments). In contrast, increasing concentrations of proctolin increase $Z_{\max}$ in PD (N=1).

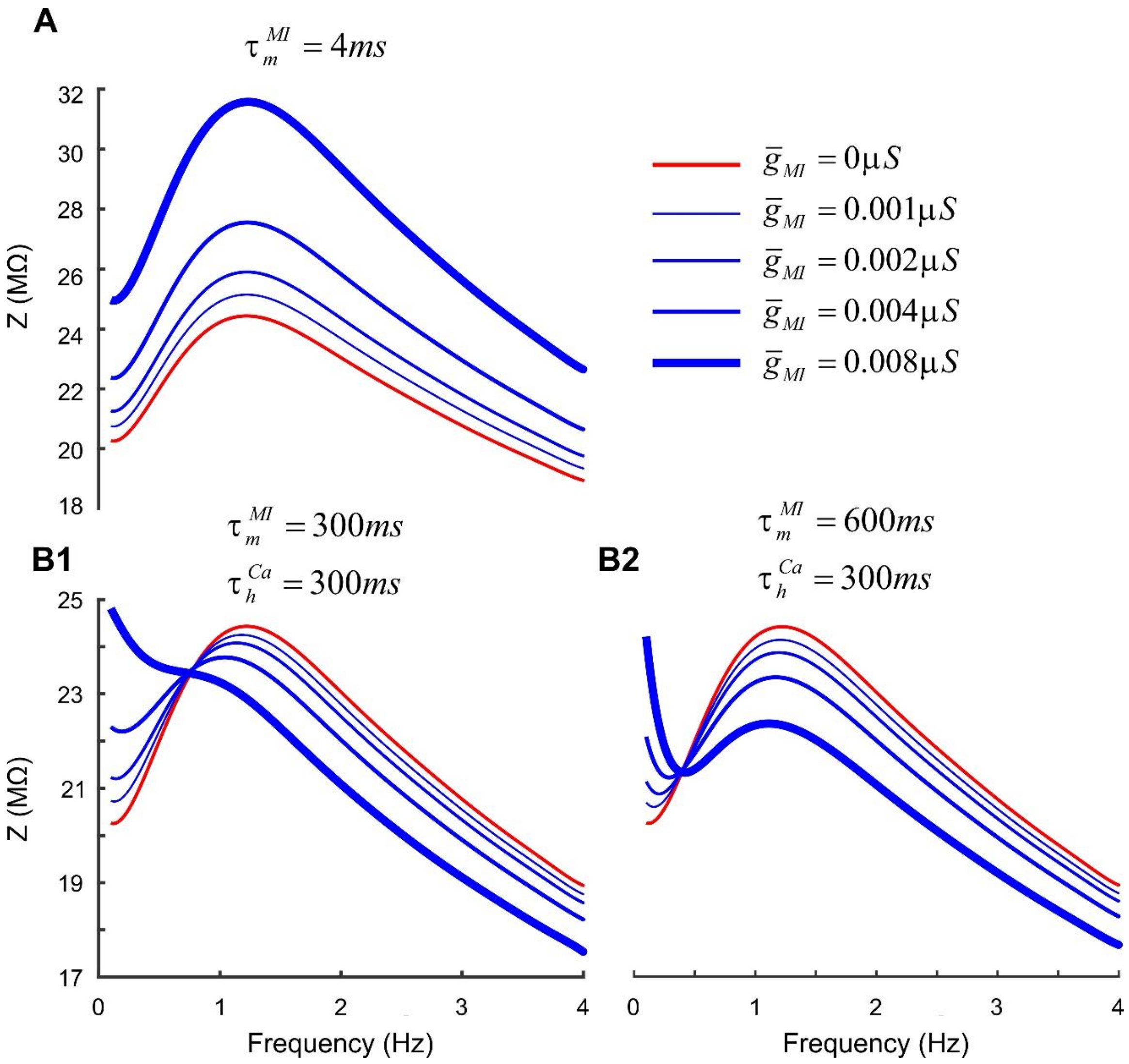

Figure 3.3 Representative *Z*-profiles for the voltage clamp simulation of a model containing I_{Ca}, I_{L}, I_{Cm} and I_{MI} given by eq. (3.3) with g_{KCa} set to 0.A, IMI has fast activation kinetics. B1, The activation rate of I_{MI} is equal to the inactivation rate of I_{Ca}. In linear models, this is equivalent to the additional amplifying variable and underlying resonant variable rates being equal. C, The activation rate of I_{MI} is twice as slow as the inactivation rate of I_{Ca}.

Previous studies indicated that proctolin activates I_{MI} [28] and that the properties of such currents cause an amplification of MPR [5] . Our modeling simulations show the action of proctolin on PD MPR likely results from the activation of I_{MI}. This was demonstrated from the fact that an increase in fast I_{MI} only led to an amplification of MPR in the presence or absence of I_{KCa} (Figure 3.4). Furthermore, the experimental difference current (defined as the difference between the voltage clamp current measured in control and in bath application of proctolin) resembled the current produced by the model equation for I_{MI} (Figure 3.5A2 and 3.5B2). In contrast, the activation of I_{MI} could not reproduce the effects of proctolin on the voltage clamp current or difference current as measured in the biological LP neuron.

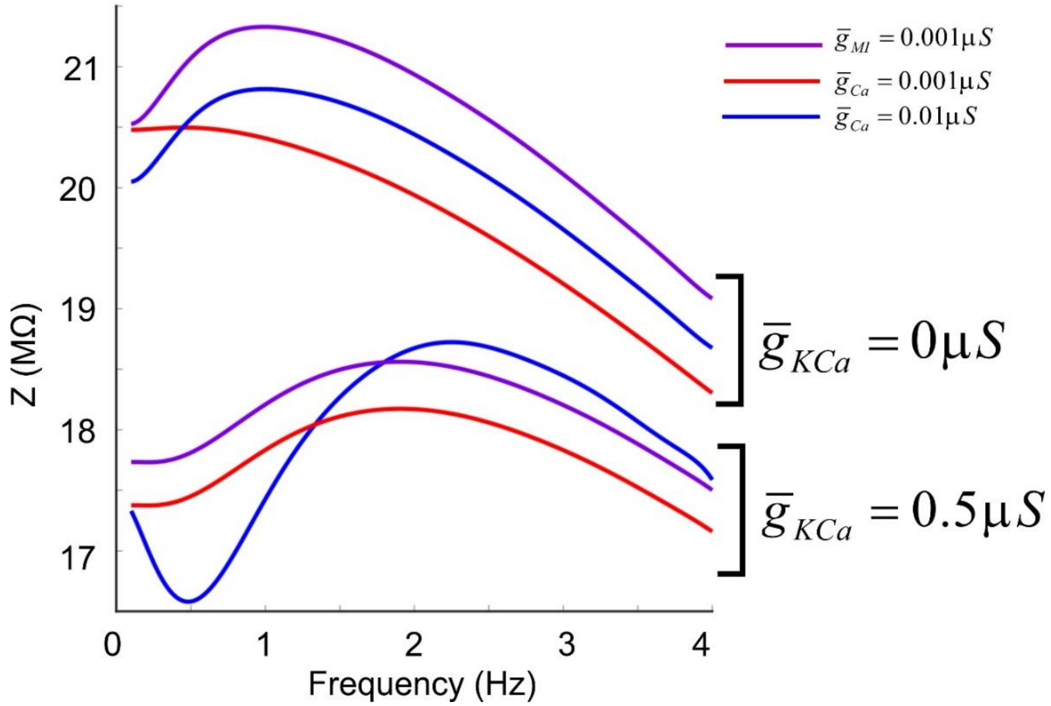

Figure 3.4 The effect of proctolin on the *Z*-profile of the LP neuron is captured by the steady-state properties of I_{KCa} and is independent of I_{MI}. The application of proctolin was simulated as an increase in the value of $\bar{g}_{Ca}$ from 0.001 µS (red) to 0.01 µS (blue). The voltage-dependent steady-state activation function and voltage-dependent time constant and calcium-dependent inactivation were all sensitive to the increase in calcium concentration. An increase in I_{MI} (purple) without increasing the value of $\bar{g}_{Ca}$ in the presence or absence of I_{KCa} does not produce antiresonance.

Modeling in voltage clamp suggests that proctolin increases the maximal conductance of a calcium current, which interacts with the properties of I_{KCa} to produce both a maximum and a minimum in the amplitude of the voltage-clamp current (figure 3.5A1). The difference current obtained as the difference between the current before and after an increase in calcium conductance in the model closely resembled that observed in experiments (Figure 3.5B1). Note this effect could also be achieved by proctolin activating additional calcium currents not necessarily those that generate the underlying MPR. These findings show that proctolin can have divergent actions at the biophysical level by affecting multiple ion channel targets, which is reflected in the MPR of individual neurons. Lastly, this shows that proctolin induces antiresonance by a slightly different mechanism than in [8] whereby additional slow positive and negative feedback effects are produced by the interaction of the gating variable dynamics associated with I_{Ca} and I_{KCa}. These feedback effects contribute amplifying and resonant variables in linearized conductance-based models.

Previous studies indicated that proctolin activates I_{MI} [28] and that the properties of such currents cause an amplification of MPR [5] . Our modeling simulations show the action of proctolin on PD MPR likely results from the activation of I_{MI}. This was demonstrated from the fact that an increase in fast I_{MI} only led to an amplification of MPR in the presence or absence of I_{KCa} (Figure 3.4). Furthermore, the experimental difference current (defined as the difference between the voltage clamp current measured in control and in bath application of proctolin) resembled the current produced by the model equation for I_{MI} (Figure 3.5A2 and 3.5B2). In contrast, the activation of I_{MI} could not reproduce the effects of proctolin on the voltage clamp current or difference current as measured in the biological LP neuron. Modeling in voltage clamp suggests that proctolin increases the maximal conductance of a calcium current, which interacts with the properties of I_{KCa} to produce both a maximum and a minimum in the amplitude of the voltage-clamp current (figure 3.5A1). The difference current obtained as the difference between the current before and after an increase in calcium conductance in the model closely resembled that observed in experiments (Figure 3.5B1). Note this effect could also be achieved by proctolin activating additional calcium currents not necessarily those that generate the underlying MPR. These findings show that proctolin can have divergent actions at the biophysical level by affecting multiple ion channel targets, which is reflected in the MPR of individual neurons. Lastly, this shows that proctolin induces antiresonance by a slightly different mechanism than in [8] whereby additional slow positive and negative feedback effects are produced by the interaction of the gating variable dynamics associated with I_{Ca} and I_{KCa}. These feedback effects contribute amplifying and resonant variables in linearized conductance-based models.

Antiresonance can be generated by adding an amplifying gating variable slower than the existing resonant one in a 2D linear model. However, in these 3D models, the antiresonance is generated by larger increases in the input resistance Z_0 than for Z_{min} [8]. This means that the 3D model shows an amplification relative to the 2D model. Our voltage clamp results indicated that proctolin, through I_{Ca} and I_{KCa}, may induce antiresonance by introducing slow resonant and amplifying effects. A recent study [8] examined the interaction between two negative feedback effects on the Z-profile and found that adding an additional resonant variable slower than the existing one present in the 2D system leads to larger decreases in Z_0 than in Z_{max}. With this knowledge, we added additional slow resonant and slow amplifying variables to the 2D model to reproduce the proctolin effect on LP MPR, i.e. the generation of antiresonance with a decrease in Z at $f < f_{\mathrm{res}}$. The resonant and antiresonant Z-profiles we used in this study have near-identical Z_0, $\mathrm{f}_{\mathrm{res}}$, $\mathrm{Z}_{\mathrm{max}}$. The parameter values generating these profiles are given in Table 2.

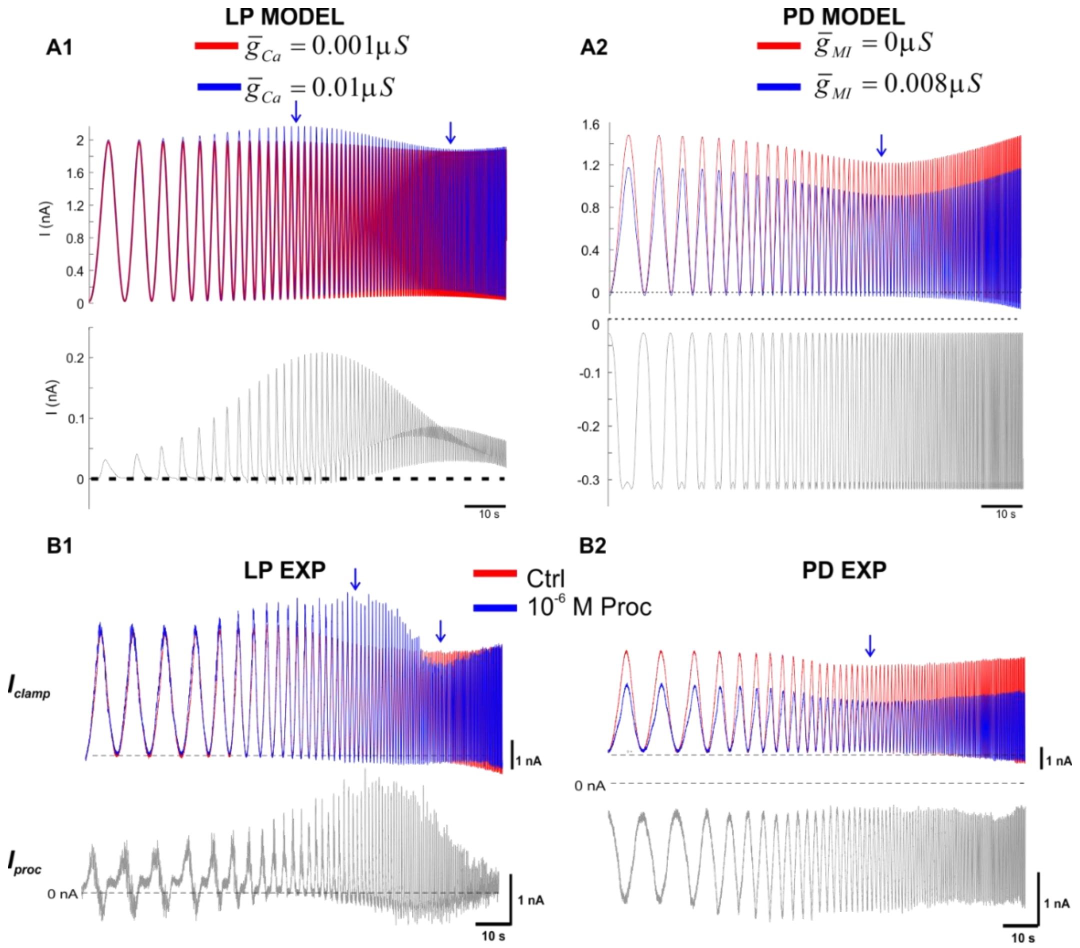

Figure 3.5 The properties of I_{KCa} and I_{MI} are sufficient to reproduce LP and PD responses to proctolin and the proctolin-activated difference current in experiments. A, The model neuron given in eq. (3.3) was voltage clamped with a ZAP waveform spanning a voltage range of -60 to -30 mV and a frequency of 0.1-4 Hz. The total voltage clamp current when is the sum of all of the currents as given in eq. (3.3) during the ZAP waveform. Simulated currents in LP (A1, upper) and PD (A2, upper) models. Proctolin modulation in LP was modeled as an increase in g_{Ca} from 0.001 µS to 0.01 uS and in the PD neuron by an increase of g_{MI} from 0 µS to 0.008 µS. The proctolin-activated current (A1 and A2, lower) is given by the difference between currents in eq. (3.3) when $\bar{g}_{Ca}$ was increased (blue) and the baseline maximum conductance (red). B, The total voltage clamp current in the biological neurons LP (B1) and PD (B2) in control conditions (10^{-7} TTX + 10^{-5} M PTX; red trace) and in the presence 10^{-6} M proctolin (B1 and B2, upper). The associated difference current is shown (B, lower; gray traces).

A four-dimensional linear model captures biological LP resonance. MPR results from the interaction between positive and negative feedback effects provided by relatively fast and slower resonant currents. Recently [8] investigated the mechanisms that govern the modulation of underlying 2D MPR by the interaction between two ionic currents with slow dynamics and either similar or opposite feedback effects. We used knowledge about these interactions to construct a 4D linear model that reproduced the proctolin-induced antiresonance seen in the biological LP neuron. To do this, we first added a slow amplifying conductance, g_2 (Figure 3.6A) slower than the resonant variable generating MPR in the 2D system. As in [8], Z_0 increases and the slower activation relative to g_1 renders $Z_{\max}$ unaffected. However, an increase in g_2 causes Z to increase for values of frequency up to f_{res}. We then recapitulated the effects on the Z-profile from the interaction of an additional slower negative feedback, g_3 with an existing slow negative feedback, g_1. For large values of the time constant of the negative feedback, increasing values of g_3 causes an increase in Q_Z due to mainly a decrease in Z_0 (Figure 3.6B). This change is accompanied by increases in f_{res}.

Antiresonance was generated by combining the effects of the interaction of a slower positive and slower negative feedback with a slow negative feedback that generates 2D resonance (Figure 3.6C). For increasing values of g_2 in the presence of g_3, a minimum in the Z-profile was generated. In constructing the antiresonance Z-profile, we made combined changes to the values of g_l, g_1, g_2, and g_3 such that the sum of these conductances remained identical to g_l and g_1 in a resonator neuron (g_l, g_1, g_2, and g_3 = 0.17) and, therefore, the value of Z_0 remained constant (Figure 3.6D). The values of the conductances were also set so that the $Z_{\max}$ was equal to that of a resonator Z-profile having a single peak.

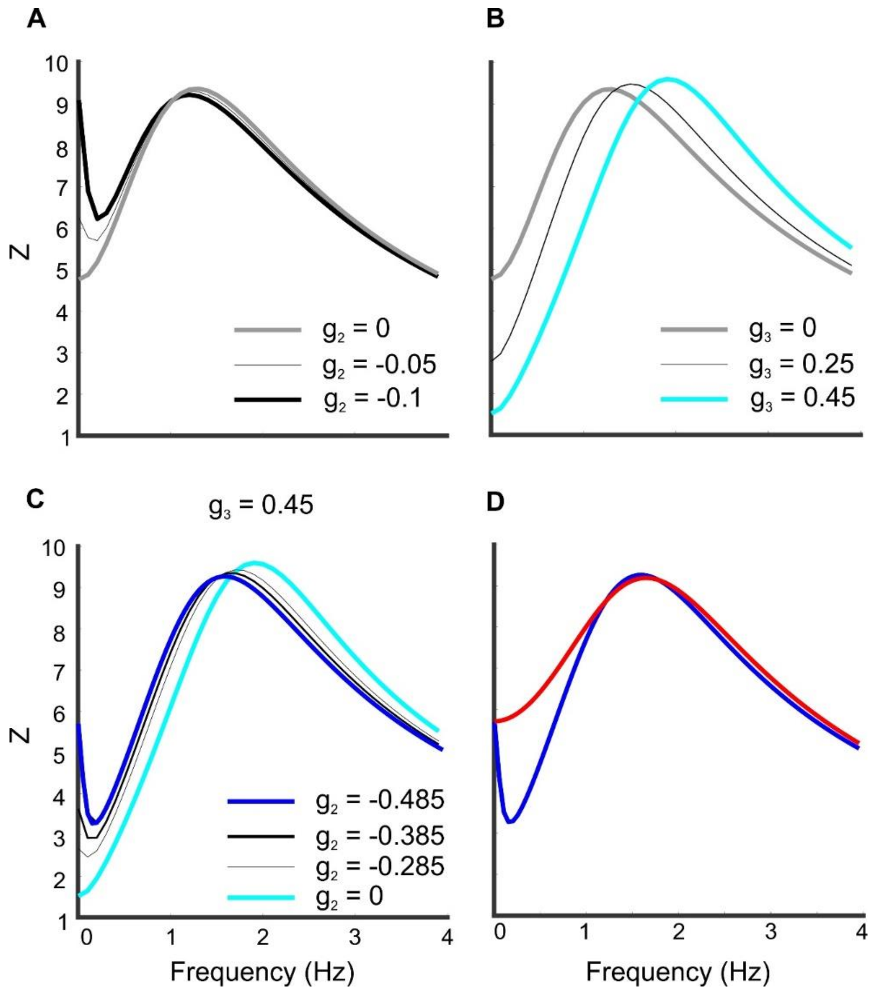

Figure 3.6 Constructing antiresonance with 4D linear models. Impedance profiles for system (6) with g_{syn} set to 0 and additional conductances added to the underlying 2D model. A, interaction between a negative and a positive feedback effect for representative sets of parameter values for $g_2<0$ and g3 = 0. B, Interaction between two negative feedback effects for $g_3 \geq 0$ and g2 = 0. C, combining the effects of the g_2 and g_3 to generate antiresonance. For a fixed value of the slower negative feedback g_3=0.45, antiresonance was generated by decreasing the value of g_2. D, The values of the conductances were set so that their sum, and therefore Z_0 of the *Z*-profile of the antiresonator (blue curve), was identical to the Z_0 of a *Z*-profile with a single resonant peak (red curve). The Z_{max} were also identical. In all panels, g1 > 0. Parameter values for conductances and time constants are given in Table 3.2

Antiresonance gates feedback inhibition at low frequencies. The interaction between a resonant and antiresonant neuron has not been studied before. We found that proctolin induced antiresonance in the LP neuron but not the PD neuron. The LP neuron of the pyloric network interacts with the PD neuron – shown to exhibit MPR – through reciprocal inhibitory connections [109]. To explore the functional role of antiresonance, we used linear models described in eq. (6). To do this, we connected, through reciprocal inhibitory connections, a 2D linear resonator (neuron A) to another linear neuron (neuron B) which was either identical to neuron A or a 4D antiresonator (Figure 3.7A). The network was driven by injecting sinusoidal currents of different frequencies into neuron A. A 4D model was used and not a 3D model because we could tune the parameters so that both Z_0 and $Z_{\max}$ were identical between the resonator and antiresonator. The only difference was in the voltage amplitude response to input $f \geq 0$ and $f \leq f_{\text{res}}$ (Figure 3.7B1). This two-neuron network was motivated by the half-center configuration of PD and LP neurons, an example of two neurons with different f_{res} that interact in an oscillatory network.

The antiresonator neuron produced a voltage response to feedforward synaptic inputs with a minimum at the antiresonance frequency (Figure 3.7B2), which can also be seen in the Z-profile (Figure 3.7C1). The Z-profile of neuron A was amplified when neuron B was a resonator or antiresonator. However, when neuron B was an antiresonator the increase in Z of neuron A was smaller than the increase produced when neuron B was an identical resonator (Figure 3.7C2). The smaller increase in Z at low frequencies is explained by the fact that feedforward inputs at f around antiresonance, the voltage amplitude is attenuated relative to the resonator and is hyperpolarized relative to the synaptic half-activation voltage. This causes the feedback synapse to be only weakly activated and results in small values of synaptic conductance in neuron A. Therefore, by attenuating the voltage amplitude response, antiresonance gates feedback input onto neuron A.

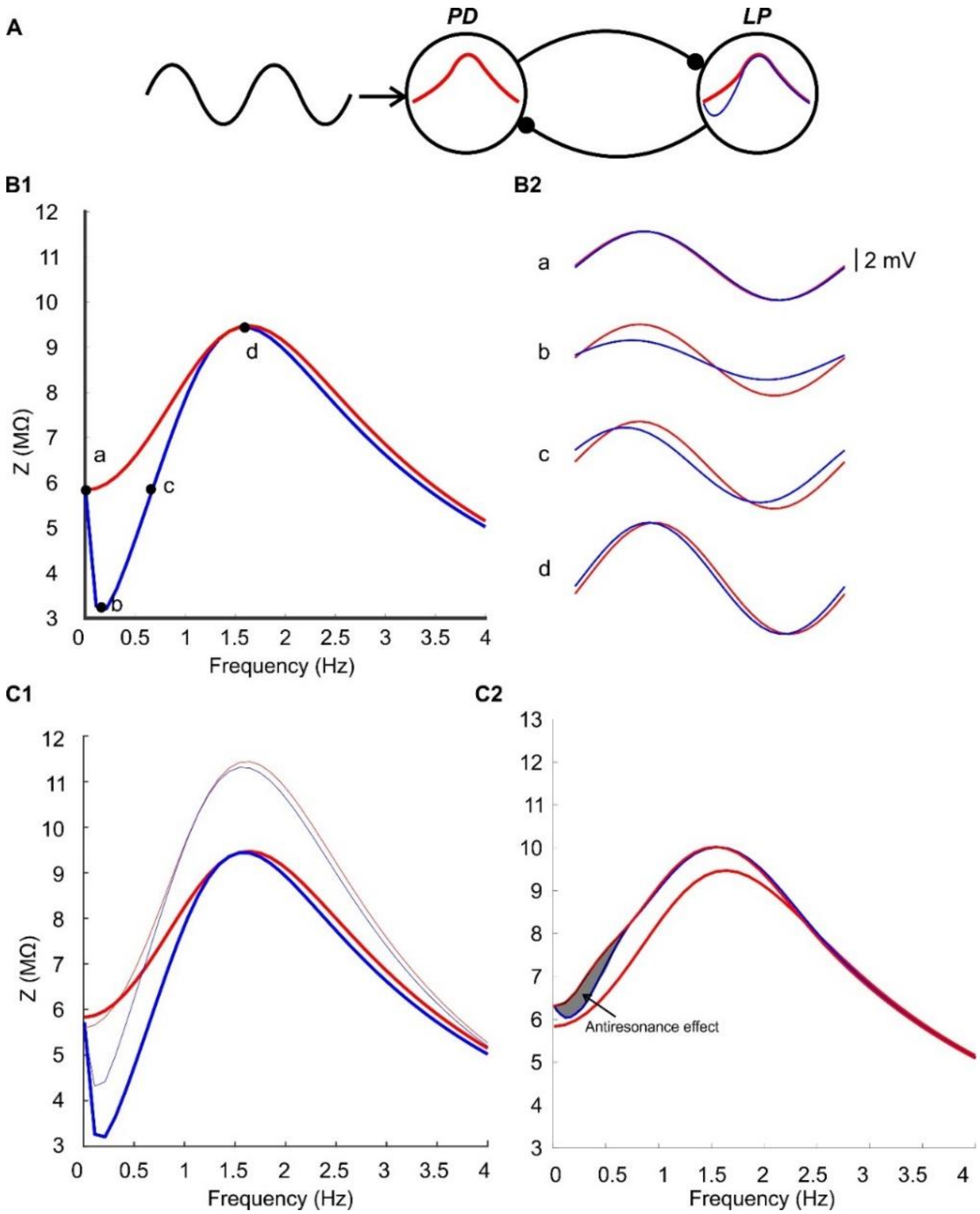

Figure 3.7 Antiresonance in a linear neuron preferentially amplifies MPR in connected neurons through reciprocal inhibitory connections. A, a 2D linear resonator was connected to either an identical 2D linear resonator or a 4D antiresonator via reciprocal inhibitory connections. The network was driven by sinusoidal current injection only into the 2D resonator. B1+B2, the voltage response corresponding to four distinct points on the Z-profiles of the 2D resonator and 4D antiresonator model neurons. At the antiresonance frequency labeled b on the *Z*-profile, the corresponding voltage response is much smaller in the antiresonator than in the resonator neuron. C1, The feedforward responses of the resonator and antiresonator to synaptic input preserve the difference between the *Z*-profiles at low frequencies. C2, The amplification of the *Z*-profile of the 2D resonator neuron by a resonator (red) through feedback inhibition is reduced when replaced by an antiresonator (blue). Gray shaded region indicates frequencies corresponding to a lesser amplification at low frequencies.

Antiresonance influences the frequency of an oscillatory network consisting of an extended Morris-Lecar oscillator and linear 4D resonator neuron. To examine whether antiresonance can influence the frequency of network oscillations. We coupled the oscillator model representing the biological neuron PD to a linear 2D resonator or a linear 4D antiresonator (Figure 3.8A and 3.8B1) and modified the properties of the oscillator model to produce oscillations at 4 different frequencies corresponding to distinct points along the *Z*-profile of the antiresonator and resonator models (Figure 3.8A). For each oscillation frequency, we measured the percent change in the period of the oscillation relative to the period of uncoupled oscillations (Figure 3.8B2). The differences in the effect on oscillation period between the two *Z*-profiles closely followed the differences in the *Z*-profiles. Moreover, when time was normalized to remove differences in frequency between the resonant and antiresonant model neurons, both neurons were equally as effective in slowing down the oscillator neuron. In contrast, the resonator was more effective than the antiresonator at slowing down the oscillator at the frequency corresponding to antiresonance. This is seen in the lower panel of Figure 3.8C where the resonator terminates the oscillator active phase earlier and remains inhibited much longer than when connected to the antiresonator. We found that at frequencies where the *Z*-profiles of the 2D resonator and 4D antiresonator were equal, their effect on the oscillation period was equal. Interestingly, the change in oscillation period showed the same non-monotonic dependence on the frequency of uncoupled oscillations. This effect may be due to the phase of the voltage response, which we do not address in this study but requires further investigation. Nonetheless, the largest difference between the two model neurons corresponded to the frequency at which antiresonance occurred (Figure

3.8D). These results demonstrate that the effect of proctolin on the network oscillator frequency may depend on the indirect actions on the *Z*-profiles of other neurons that interact with pacemaker oscillations.

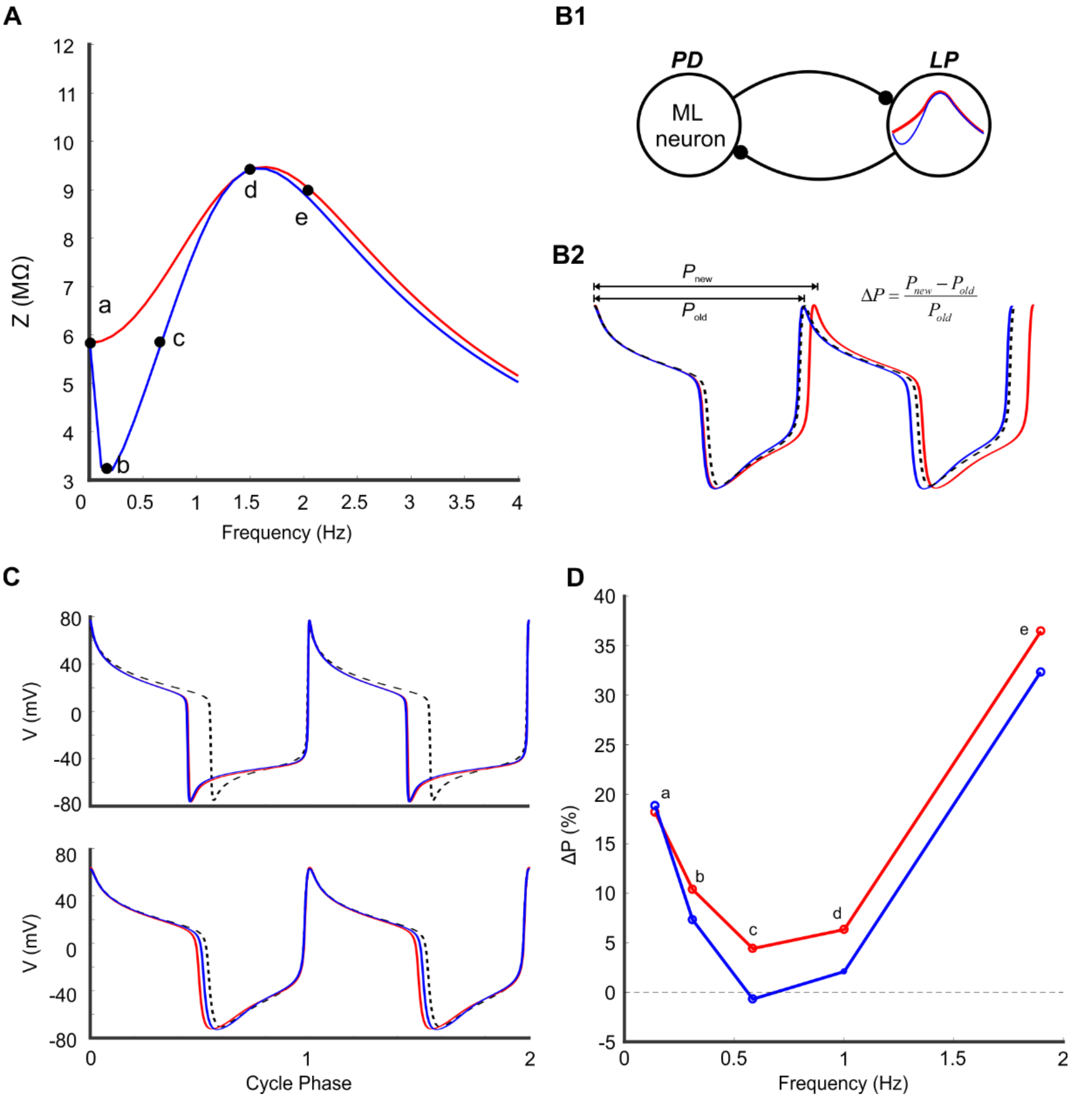

Figure 3.8 The effect of antiresonance on the frequency of Morris-Lecar oscillations. A, The Morris-Lecar model - given in eq. (3.8) and Table 3.4 - was modified to produce oscillations at frequencies corresponding to distinct points along the *Z*-profiles of a 2D resonator and a 4D resonator. B1, The Morris-Lecar model was connected to a 2D resonator and a 4D resonator via reciprocal inhibitory connections. B2, The oscillation period was measured as the change relative to the period of uncoupled oscillations. C, voltage traces of the ML neuron showing 2 cycles normalized in time uncoupled (dashed black line) and when coupled to a 2D linear resonator (red) or a 4D antiresonator (blue). D, The change in oscillation period as a function of uncoupled oscillation frequency when coupled a 2D resonator (red) or 4D antiresonator (blue).

3.4 Discussion

Understanding the generation of network oscillation frequency involves examination of the dynamic properties of the participating neurons and their interaction with network connectivity. One dynamic property is MPR [42]. For some neuron types, f_{res} is correlated with the oscillatory frequency of the networks in which they are a part [2 , 4, 65, 77, 97]. Although a causal relationship between MPR and the frequency of network oscillations has been shown in electrically-coupled networks [9], little is known about the contribution of MPR to activity of networks connected through chemical synapses. However, populations of resonant inhibitory neurons have been shown to promote network oscillations with stable frequency [2]. Furthermore, distinct neuron types in the same network show different f_{res} values [6, 29] but it is unclear how their MPR properties interact and how they contribute to network oscillations.

In this paper, we showed that MPR in distinct neuron types may be generated by different voltage- and time-dependent properties of ionic currents, which are the targets of neuromodulation. This neuromodulation can induce antiresonance in only one neuron type in a pair of synaptically-coupled neurons. Here, in the pyloric network of the crab STG, we demonstrated that the neuropeptide, proctolin, differentially altered the *Z*-profiles of the PD and LP neurons, which interact. In the LP neuron, proctolin induced antiresonance and increased in f_{res} whereas in the PD neuron, proctolin only increased $Z_{\max}$ without affecting f_{res}. The differences in PD and LP neuron *Z*-profiles are similar to the differences between pyramidal neurons (resonance) and interneuron (antiresonance) in the hippocampus [6]. The difference in Z-profiles between the neurons could indicate the unique roles in responding to external inputs and shaping network activity at different frequencies. We sought to find the mechanism for the generation of antiresonance of the type seen in the LP neuron at the nonlinear biophysical level and the linear level that represent ionic currents through the interaction of positive and negative feedback effects of gating variables. Constructing antiresonance at the linear level allowed us to examine how antiresonance contributes to activity and interacts with MPR in other network neurons.

Our experimental observations of the induction of LP antiresonance by proctolin were inconsistent with reports that proctolin activates only I_{MI}. There is evidence that peptides activate low-threshold activated currents that are voltage-, time- and calcium-dependent in other stomatogastric neurons [41, 113, 115]. The generation of antiresonance in the LP neuron is different from that exhibited by 3D linear models with a current that contributes a slow amplifying variable because the antiresonance is generated by increases in the input resistance Z_0 [8]. Therefore, the LP antiresonance involves a new biophysical mechanism that involves more than just the addition of a slow amplifying current. We explored the mechanisms at the nonlinear biophysical level in voltage clamp and with linearized conductance-based models.

We showed that fast activating I_{MI} increased the amplitude of MPR and a slowly-activating I_{MI} produced antiresonance by increases similar to [8]. Previous studies demonstrated that the neuropeptide proctolin increased the calcium concentration in muscle cells of lobster [115]. Our results showed that an increase in the maximum conductance of an existing I_{Ca} generated antiresonance that depended on the presence and properties of I_{KCa} and is consistent with effects of proctolin on the Z-profile of the biological LP neuron (Figure 3.4B1). Although proctolin may not affect the peak amplitude of the I_{KCa} (unpublished data), it is conceivable that it could modify the voltage-dependent time constant. Changing the rate would in turn change the transient response to sinusoidal current inputs.

Both PD and LP neurons contain similar amounts of high-threshold K^+ currents [21] and the time constant of I_{KCa} activation is highly voltage-dependent. We found the generation of antiresonance by an increase in the maximal conductance of I_{Ca} depended on the properties of the voltage-dependent activation time constant. Increases in I_{Ca} maximal conductance only produced antiresonance when the activation rate began to decrease at lower voltages and not higher voltages (not shown). This result could be verified by comparing the time to peak of I_{KCa} in response to voltage steps between LP and PD. This suggests that although proctolin may activate the same ionic current in distinct neuron types, its effect on the Z-profile may depend on the voltage- and time-dependent properties of ionic currents.

Previous studies investigated the mechanisms that generate antiresonance in 3D linear models [8]. We used linear models utilizing the findings from [8], which investigated the consequences of additional negative and positive feedback processes on the MPR generated by a 2D linear neuron. We found that the generation of antiresonance in the LP neuron by proctolin involved the activation of both slow positive and negative feedback effects provided by the gating variables of ionic currents. Therefore, we used a 4D linear model to simulate the *Z*-profile in proctolin. We used this 4D linear antiresonator neuron to examine its effects on network activity. We found that, relative to a 2D resonator; it preferentially amplified the *Z*-profile of a coupled neuron through reciprocal inhibitory connections. This occurred due to antiresonance attenuating the voltage amplitude response to feedforward synaptic input and therefore the conductance of feedback inputs was reduced. Similarly in this frequency range an antiresonator has a smaller effect on the frequency of an oscillator neuron. At the same time, the generation of antiresonance was also accompanied by changes in the phase shift of the neuron; but it is not clear whether phase, amplitude or both contribute to the network effects we observe. Therefore, future studies are required to determine the contributions of Z-profile and φ-profile through network connections.

We used linear models to generate antiresonance so that we could investigate its role within a network. We wanted to use linear models because we could change more than one parameter at a time to modify Z-profile attributes without affecting other attributes. We therefore ensured that the observed effects are directly due to the difference in Z of antiresonant and resonant profiles where antiresonance occurs, i.e. at $f>0$ and $f<=f$res. Both the resonant and antiresonant neurons were nearly identical in their Z-profiles for all other frequencies. Previously, the study of the emergence of antiresonance was approached by examining the modulation of MPR in 2D models by the interaction between two ionic currents with slow dynamics and either a positive or negative feedback [8]. We used these findings to construct a linear antiresonator that had an additional resonant variable and an amplifying variable, both operating at time scale slower than the resonant variable generating the underlying 2D MPR in the system. If the additional resonant variable is sufficiently slower than the existing resonant variable then it causes an amplification due to a decrease in Z_0 without affecting f_{res} or $Z_{\max}$ (see Figure 5b in [98]). To match the value of Z_0 (to recapitulate the proctolin modulation of the Z-profile by proctolin), we used added a slow amplifying variable to make a 4D model. The

4D model would respond to inhibition similarly to a 2D model if the conductances were changed such that their sum, and therefore, Z_0 was kept constant. This allowed us to examine the effect of changes in the voltage amplitude response while keeping the baseline voltage response to inhibition equal. This, in turn, allowed us to show that decreases in the voltage amplitude response of an antiresonator can reduce its influence in shaping the frequency response of connected neurons through feedback inhibition.

We speculate that the effects of antiresonance on oscillator frequency through inhibitory coupling could be due to the phase response properties of the coupled antiresonator/resonator neurons. The antiresonator had minimal effect on the oscillator frequency where the intrinsic oscillator frequency corresponded to the antiresonance frequency. The effect of phase response may be just as influential in determining the oscillator frequency due to the properties of the PRC of the coupled oscillator neuron. It would be interesting to determine if the effects of antiresonant versus a resonant neuron would depend on whether the neuron is a type 1 (an input can only delay independent of phase) or type 2 (an input can either advance or delay dependent on the phase). Therefore, it is not clear whether the antiresonator effect holds for all oscillators. Lastly, the suppression in the Z-profile at low frequencies may not have any effect on the frequency of an oscillator because depending on the biophysical properties of the oscillator, the PRC may be insensitive to changes in strength of the inhibitory synaptic input [116].

The PD neuron is electrically-coupled to other pyloric neuron types that includes the anterior burster neuron (AB) and two lateral posterior gastric neurons (LPG). Furthermore, previous studies have shown that the resonance frequency can influence the frequency of oscillations though electrical coupling [9]. Thus MPR measured in PD in the absence and presence of proctolin could result from network interactions. However, previous work in our lab demonstrated that MPR in PD is independent of its electrical coupling to the AB neuron [4]. Therefore, we are confident that our results are due to the effects of proctolin on the PD neuron.

The generation of antiresonance opens up several interesting questions about its role within a network. Our results make two predictions about the role of antiresonance in a two-cell reciprocal inhibitory network: (1) produces a sharpening in the *Z*-profile of coupled neurons receiving oscillatory inputs by precluding the amplification by the inhibitory synapse at low frequency; (2) will produce no change in an oscillator neuron at frequencies where antiresonance and the associated increased phase advance occur. These predictions can be tested using the dynamic clamp method. One can isolate either a follower LP or PY neuron and examine how coupling to a model antiresonator changes the *Z*-profile at low frequencies relative to a model resonator. Additionally, we could test the effects of antiresonance on the oscillations of PD pacemaker neurons by coupling a linear antiresonator when the frequency of PD neuron oscillations are changed by either DC current injection or injection of a low-threshold inactivating calcium current with various values of the inactivation time constant.

CHAPTER 4

FREQUENCY-DEPENDENT ACTIONS OF NEUROMODULATION

4.1 Introduction

Different neuromodulatory inputs underlie the flexibility in network operation by changing intrinsic and synaptic properties of network neurons [117, 118] . However, understanding how neuromodulatory actions on any single component influence the network output is often extremely difficult because the activity state of a network depends on the synaptic interactions of many neurons. Even at the level of a single neuron, modulation of any individual ion channel current may produce effects that are not readily predictable because multiple nonlinear ionic currents interact with one another and with the synaptic inputs to produce a neuron’s output. Moreover, dynamic interactions of ionic currents and synapses can lead to neuromodulator actions that are state or history dependent [119-121].

A prominent example of state-dependence is seen in oscillatory networks when the effect of a neuromodulator depends on the network frequency [31, 33, 122]}. One mechanism that could account for such state-dependent action is the activation or inactivation kinetics of the ionic currents targeted by the neuromodulator. It is also possible that the neuromodulator-activated currents may interact with other ionic currents in a way that would influence activity in specific frequency ranges [33]. However, neuromodulators often elicit reliable changes in activity, independent of variable underlying components [123].

In this paper we examine the hypothesis that network frequency may gate the actions of a neuromodulator on the neuronal output because the time-dependent kinetics of the ionic currents targeted by that neuromodulator produce a frequency-dependent effect. We address this hypothesis using the crustacean pyloric network, a well-studied central pattern generator (CPG) that produces stable oscillations in a range of frequencies (0.5 to >2 Hz), driven by rhythmic bursting in a group of pacemaker neurons, which drives all follower neurons with strong inhibitory synapses. The follower neurons, including the lateral pyloric (LP) neuron, rebound from this inhibition to produce a burst of action potentials. These neurons maintain a relatively constant bursting phase within each cycle, in a wide range of network frequencies [17, 49]. Pyloric follower neurons are modulated by a number of monoamines and neuropeptides that modulate their rhythmicity, rebound and excitability properties [13]. Among the best studied modulators of the pyloric network is the neuropeptide proctolin, which activates a fast voltage-dependent persistent current (the modulator-activated inward current, I_{MI}) in several pyloric neurons [27]. I_{MI} is thought to be crucial for the generation of oscillatory activity in this network [17, 28, 124].

To address whether the actions of proctolin on the LP neuron vary, depending on the network frequency during ongoing activity, we measured proctolin-activated currents using realistic LP neuron voltage waveforms applied at different cycle frequencies. We then used voltage ramps with different slopes to describe the variations in the proctolin-activated currents as a function of cycle frequency. Finally, using a combination of computational modeling and dynamic clamp, we explored how these currents may modify the LP neuron activity, including its burst onset phase and duty cycle in a frequency-dependent manner.

4.2 Methods

Solutions.

Cancer borealis physiological saline contained the following (in mM): 440 NaCl, 26 $MgCl_2$, 13 $CaCl_2$, 11 KCl, 10 Trisma base, 5 maleic acid, and 5 glucose, pH 7.4-7.6. All preparations were superfused with saline at 10-13ºC. Proctolin (American Peptide) was dissolved as a stock solution in distilled water and stored in 10^{-3} M aliquots and frozen at -20°C. We used a final concentration of 10^{-6} M, prepared by dissolving the stock solution in saline. Proctolin was superfused for at least 20 minutes before performing voltage-clamp measurements. Proctolin was washed out for at least 1 hour before repeating voltage-clamp protocols, as explained below.

For voltage-clamp experiments, tetrodotoxin (TTX; 10^{-7} M; Biotium), picrotoxin (PTX; 10^{-5} M; Sigma) were added to the saline to suppress voltage-dependent Na^+ currents (TTX) and glutamatergic inhibitory synaptic transmission (PTX). For dynamic-clamp experiments, PTX was added to the saline and the STG was isolated from descending neuromodulatory inputs by transection of the stomatogastric nerve (*stn*).

Realistic LP neuron voltage waveforms in voltage clamp.

We recorded the activity of an LP neuron during the ongoing rhythm and used the average of 5 cycles, sampled at 1000 points, to produce a unitary realistic waveform. This waveform was scaled to the desired amplitude and applied periodically at fixed cycle periods to drive the voltage clamped LP neuron, using the software Scope, developed in our laboratory (http://stg.rutgers.edu), and pClamp 10.3 (Molecular Devices). The periodic realistic waveform was applied from a holding voltage of -60 mV, with a slow-wave amplitude of 30 mV and a cycle period of 500, 1000 or 2000 ms. Each application sweep was done for 30 s. This protocol was carried out in normal saline and in the presence of 10^{-6} M proctolin, superfused for at least 20 minutes. The difference between the voltage clamp currents in the presence of proctolin and in normal saline (with identical voltage inputs) was defined as the proctolin-activated current I_{proc}. For quantification of the current, the difference current was filtered using the built-in MATLAB function *medfilt1* to remove the capacitive artifacts that resulted from the fast voltage changes in the LP waveform.

Voltage clamp ramp protocols.

The proctolin-activated current was measured by injecting symmetric ramps waveforms (-80 to 20 to -80 mV at four different slopes: ±400, ±200, ±100, and ±50 mV/s) into the voltage clamped LP neuron in normal saline and in the presence of 10^{-6} M proctolin. The difference current was defined as the proctolin-activated current I_{proc}. We quantified the effect of ramp slope and direction on the amplitude of this current by first fitting the current using a standard biophysical equation:

$$I(V) = I_0 + \bar{g}\,\frac{1}{1+\exp\left(-(V-V_{1/2})/k\right)}(V-E_{rev}) \tag{4.1}$$

with free parameters I_0, $\bar{g}$, $V_{1/2}$, k and E_{rev}. We used two-way repeated measures ANOVA to test for significance of the effect of ramp direction and ramp slope.

The model ionic currents used to reproduce the period- and slope-dependence of the proctolin-activated current.

We modeled the dependence of the proctolin-activated current on the period of the realistic LP waveforms and the voltage ramp slopes by assuming that proctolin activated a sum of two voltage-gated currents I_{MI} and a putative calcium current I_{CaProc}.

Both currents were modeled as standard Hodgkin-Huxley type currents with the associated gating variable equations given in Table 4.1.

I_{MI} was modeled as previously described [94]. The parameters of the steady-state activation and inactivation functions and time constants of I_{CaProc} were found by performing voltage clamp simulations to reproduce the amplitude dependence of the current on the rising phase of a voltage ramp slope and voltage waveform cycle period.

We modeled the activation and inactivation of I_{CaProc} to be within reported ranges of T-type calcium currents (I_{CaT}). The half-activation voltage of I_{CaT} is reported to be between -45 and -60 mV and the activation can be as fast as 2 ms [125]. Several types of neurons have I_{CaT} half-inactivation voltages around -80 mV [126], although it can be as high as -64 mV. [127]. While some neuron types have very slow I_{CaT} deinactivation rates, on the order of 1 s, [128], others are characterized by very rapid recovery, on the order of 90 ms [129].

The family of optimal LP model neurons.

Because neuromodulators have consistent effects on neuronal excitability independent of the baseline variability in biophysical parameters, we sought to find multiple models that produce approximately the same response to the synaptic input. We used a conductance-based model with currents known to be expressed in STG neurons [130] and used in other models of the LP neuron [36].

We developed a family of computational models of the LP neuron adapted from a previous model [36]. The 4-compartment model of Taylor, et al was reduced to 2 compartments, one representing the soma, primary neurite, near and far dendrites, and the other representing the axon. Only the axon compartment had a fast sodium current and therefore this compartment generated the action potentials. We did not see any significant difference between our 2-compartment model neurons and the corresponding 4-compartment models of Taylor et al [36].

The voltage in each compartment obeyed the current balance equation:

$$C\frac{dV}{dt} = -I_{mem} - I_{axial} - I_{Syn} \tag{4.2}$$

where C is the compartment capacitance, I_{mem} is the total intrinsic ionic currents, I_{axial} is the axial current coupling soma and axon compartments, and I_{Syn} is the synaptic current. The currents that composed I_{mem} in the soma were the transient potassium current (I_{A}), a persistent calcium current (I_{CaS}), a transient calcium current (I_{CaT}), a calcium-activated potassium current (I_{KCa}), a hyperpolarization-activated inward current (I_{H}) and a leak current ($I_{\text{L-soma}}$). The currents that composed I_{mem} in the axon were the fast sodium current (I_{Na}), the delayed-rectified potassium current (I_{Kd}) and a leak current ($I_{\text{L-axon}}$).

The mathematical descriptions of these currents was based on descriptions in previous work [28, 36, 130]. In all cases, we tuned the half-activation voltages and kinetics of these currents to provide good fits to voltage-clamp data. For instance, we tuned the properties of I_{KCa} to fit voltage-clamp measurements of the transient part of the high-threshold K^+ current in pyloric neurons [21]. All currents, including calcium currents, were modeled as ohmic currents, described by the equation:

$$\begin{gathered} I_j = \bar{g}_j m^p h^q (V - E_x) \\ \tau_x(V)\frac{dx}{dt} = x_\infty(V) - x \end{gathered} \tag{4.3}$$

where V is the membrane potential in mV, the gating variable x represents either m (activation) or h (inactivation) with time constant τ_x. In the case of the calcium-activated potassium current I_{KCa}, x_∞ and τ_x also depended on an ad hoc internal calcium current. The exact forms for x_∞ and τ_x are given in Table 4.1.

The conductance of I_{Syn} used to drive the model was obtained by voltage clamping the biological LP neuron at a holding voltage of -50mV during an ongoing pyloric rhythm and recording the synaptic current (data courtesy of H. Anwar). The conductance was given as:

$$g = \frac{I}{(V - E_{rev})} \tag{4.4}$$

where E_{rev} is the synaptic reversal potential, assumed to be -80 mV [17]. The conductance g was obtained by taking the average across 5 cycles, each waveform was scaled in time and amplitude and sampled at 1000 points to produce a unitary conductance waveform. This waveform was scaled to the desired conductance amplitude and period and injected periodically into the model neuron at different cycle periods: 500, 750, 1000 and 2000 ms. The same procedure was used in dynamic clamp below.

To find multiple optimal models of the LP neuron, we used a multi-objective evolutionary algorithm [37, 84, 89]. Evolutionary optimization finds solutions by optimizing a set of objectives. Each objective represents the difference between the target and the model attributes. For each objective, the target is defined as a range of desired values.

In our problem, the model attributes are parameters associated with the model voltage response to the synaptic conductance input applied at 1 Hz. We optimized the following 5 objectives: 1, slow-wave amplitude (18-25 mV); 2, burst onset phase (0.49-0.55); 3, burst duration **(**120 ms); 4, number of spikes per burst (2-8); 5, minimum membrane potential

(-65 - -60 mV). The MOEA was run with a population of 100 individuals and for 50 generations. We obtained a total of 300 optimal models and, to save computation time, performed all analysis on a random subset of 50 models from this population.

When optimizing multiple and potentially conflicting objectives, MOEA will find a set of solutions that constitute trade-offs in objective scores. For instance, an optimal parameter set may include solutions that are optimal in the burst onset phase but not in the slow-wave amplitude or vice versa and a range of solutions in between that result from the trade-offs in both objectives. Using NSGA-II, we varied the maximal conductance values and the voltage-dependence and kinetics of the transient I_{CaT} and persistent I_{CaS} calcium currents using "fudge factor" parameters v_{shift}, v_{scale}, and τ_{scale} that altered the dynamics of the currents. We explored the kinetics and voltage dependence because calcium currents have not been characterized in this system and the kinetic parameters that we adopted from other models may not have been appropriate for modeling the LP neuron.

All simulations were performed with custom written code in C++ and exported as Python modules so that the Python evolutionary algorithms library DEAP could be used for optimization.

Dynamic clamp experiments.

We used dynamic-clamp to inject artificial versions of ionic (I_{MI}, and I_{CaProc}) and synaptic currents (I_{Syn}) into the LP neuron [9, 21, 92, 124]. These currents were identical to those used in the computational model described above. The synaptic conductance was set to 0.1μS unless otherwise stated. With each set of parameters for I_{MI} and/or I_{CaProc}, the biological LP neuron was driven by a synaptic conductance with a reversal potential of -

80mV for at least 30s. The LP neuron activity was recorded for at least 10s before addition of I_{MI} and/or I_{CaProc} and the synaptic activation.

Table 4.1 Equations governing the Voltage-Dependence and Kinetics of Ionic Currents in the LP model Neurons.

		m_∞	τ_m	h_∞	τ_h
I_{H}	m	$\mathrm{lgc}\left(-\frac{v+84}{86}\right)$	200	-	-
I_{A}	$\mathrm{m^2h}$	$\mathrm{lgc}\left(\frac{v+54}{2}\right)$	$50+20m_\infty(v)$	$\mathrm{lgc}\left(\frac{v+60}{1}\right)$	$50+100h_\infty(v)$
I_{CaS}	$\mathrm{m^3}$	$\mathrm{lgc}\left(\frac{v+22+v_{shift}}{8v_{scale}}\right)$	16		
I_{CaT}	$\mathrm{m^3h}$	$\mathrm{lgc}\left(\frac{v+40+v_{shift}}{6v_{scale}}\right)$	$60\tau_{scale}$	$\mathrm{lgc}\left(-\frac{v+60+v_{shift}}{8v_{scale}}\right)$	$400\tau_{scale}$
I_{KCa}	mh	$\frac{\mathrm{lgc}\left(\frac{v+10}{13}\right)}{1+(C/25)^{-5}}$	$500-499\,\mathrm{lgc}\left(\frac{v-[-52-2.7\ln(C/20)]}{10}\right)$	$\frac{1}{1+(C/7.2)^{5/4}}$	12
I_{MI}	m	$\mathrm{lgc}\left(\frac{v+45}{5}\right)$	4	-	-
I_{CaProc}	$\mathrm{m^3h}$	$\mathrm{lgc}\left(\frac{v+50}{7}\right)$	1	$\mathrm{lgc}\left(\frac{v+56}{4}\right)$	85

The membrane potential v is in mV, intracellular calcium concentration is C is in µM and the time constants are τ_m and τ_h are in ms. $\mathrm{lgc}(x)=1/(1+\exp(-x))$. All parameters modified from [36], except for I_{CaProc} which was determined empirically to fit the properties of the proctolin-activated current.

Occasionally, the resting membrane potential and action potential threshold varied between preparations, most probably due to impalement quality. Therefore, to produce more consistent measurements, we also injected a leak current with a small negative maximal conductance to ensure that the LP neuron produced approximately the same number of spikes at the same frequency as measured during the ongoing rhythm. The negative-conductance leak current was given by $I_{NL}(V)=\bar{g}_{NL}(V-E_{NL})$ where E_{NL} =-68 mV is the reversal potential and $\bar{g}_{NL}$ is the conductance. When the value of the leak conductance was set to be negative in the dynamic clamp software it resulted in an overall decrease in the input conductance of the neuron.

Table 4.2 Model fixed parameter values

Parameter	**Value**
E_{Na}	50 mV
E_K	-80 mV
E_{Ca}	According to the Nernst equation at 10°C with $[Ca]_O$ = 13 mM.
E_{CaProc}	120 mV
E_H	-10 mV
E_{MI}	0 mV
$E_{L\text{-}Soma}$	-25 mV
$E_{L\text{-}Axon}$	-60 mV
$C_{m\text{-}Soma}$	40 nF
$C_{m\text{-}Axon}$	10 nF
$r_{axial\text{-}axon}$	r_a=0.3μS
$r_{axial\text{-}soma}$	r_a =1.3μS
[Ca]	τ_{Ca}=10 ms, Vol=6.49 μm^3, $[Ca]_\infty$ =20 μM

Dynamic clamp was implemented using the NetClamp software (Gotham Scientific; http://gothamsci.com/NetClamp) on a 64-bit Windows 7 PC using an NI PCI-6070-E board (National Instruments). Data were acquired using a Digidata 1440A Digitizer (Molecular Devices) at 5-KHz sampling rate.

Data analysis and statistics.

The response of the LP neuron to synaptic conductance inputs at different frequencies was analyzed using custom-written MATLAB (MathWorks) scripts. For each frequency and in separate instances with the addition of either I_{MI} or I_{MI} with I_{CaProc}, we measured the burst onset phase, termination phase and slow-wave amplitude of the LP neuron. The LP response phase in each cycle was analyzed from the onset of the pacemaker component of the synaptic input. Statistics were done in R (R Foundation).

4.3 Results

Across different animals, the pyloric network cycle period can vary considerably ranging from approximately 0.5 to >2 s [17]. The network output can be altered by multiple biogenic amines and neuropeptides that modify the properties of neurons and synapses. However, the effect of neuromodulators on the pyloric network activity depends on the state and level of activity of the network. For instance, proctolin increases the frequency of the pyloric rhythm when the initial frequency is low, but has little or no effect on frequency when the starting frequency is high [31, 33, 34]. The effect of neuromodulators at the single neuron level can also be altered by activity. For instance, the R15 neuron of *Aplysia* fires bursts of action potentials strongly modulated by serotonin. Changes in the activity that alter intracellular calcium levels also influences the modulation of R15 by serotonin [35].

Because most neuromodulators act through second-messenger pathways to modify the excitability of neurons, their action may be influenced by the ongoing activity patterns of target neurons. While proctolin has state-dependent effects on the pyloric network frequency [33], it may also have effects on the dynamics of individual neurons, which also depends on the network frequency. Recent work demonstrated that neuropeptides activate time-dependent ionic currents in other STG neurons [41]. In this study, we address the state-dependent effects of proctolin on the activity of the follower neuron LP. Specifically, we examine the hypothesis that the current activated by proctolin in the follower neuron LP depends on the frequency of ongoing pyloric network oscillations.

The amplitude of the proctolin-activated current is sensitive to the voltage waveform period. We examined whether the actions of the proctolin on the LP neuron depend on the pyloric cycle period. To measure the ionic currents activated by proctolin in the LP neuron, we abolished the ongoing rhythmic activity with bath application of TTX, PTX and by removing endogenous neuromodulatory inputs (see Methods). We then played back pre-recorded LP neuron voltage waveforms at different cycle periods in control saline and during bath application of 10^{-6} M proctolin and measured the proctolin-activated current (I_{proc}) as the difference current (Figure 4.1).

The peak amplitude and mean value of I_{proc} decreased with the waveform cycle period (Figure 4.1A). Overall, the longer waveform periods produced a significantly smaller current (one-way RM-ANOVA; N=6, $p < 0.001$). The mean current value followed the same trend as the peak and was significantly smaller as at longer waveform periods (one-way RM-ANOVA, N=6, $p < 0.001$). The fact that the waveform rise slope decreases with cycle period suggested that the decrease in I_{proc} and mean with longer cycle periods may be due to the increased inactivation of this current. Thus these results suggest that the changes in the mean current may be caused by the dynamics of inactivation of I_{proc} or some component of this current

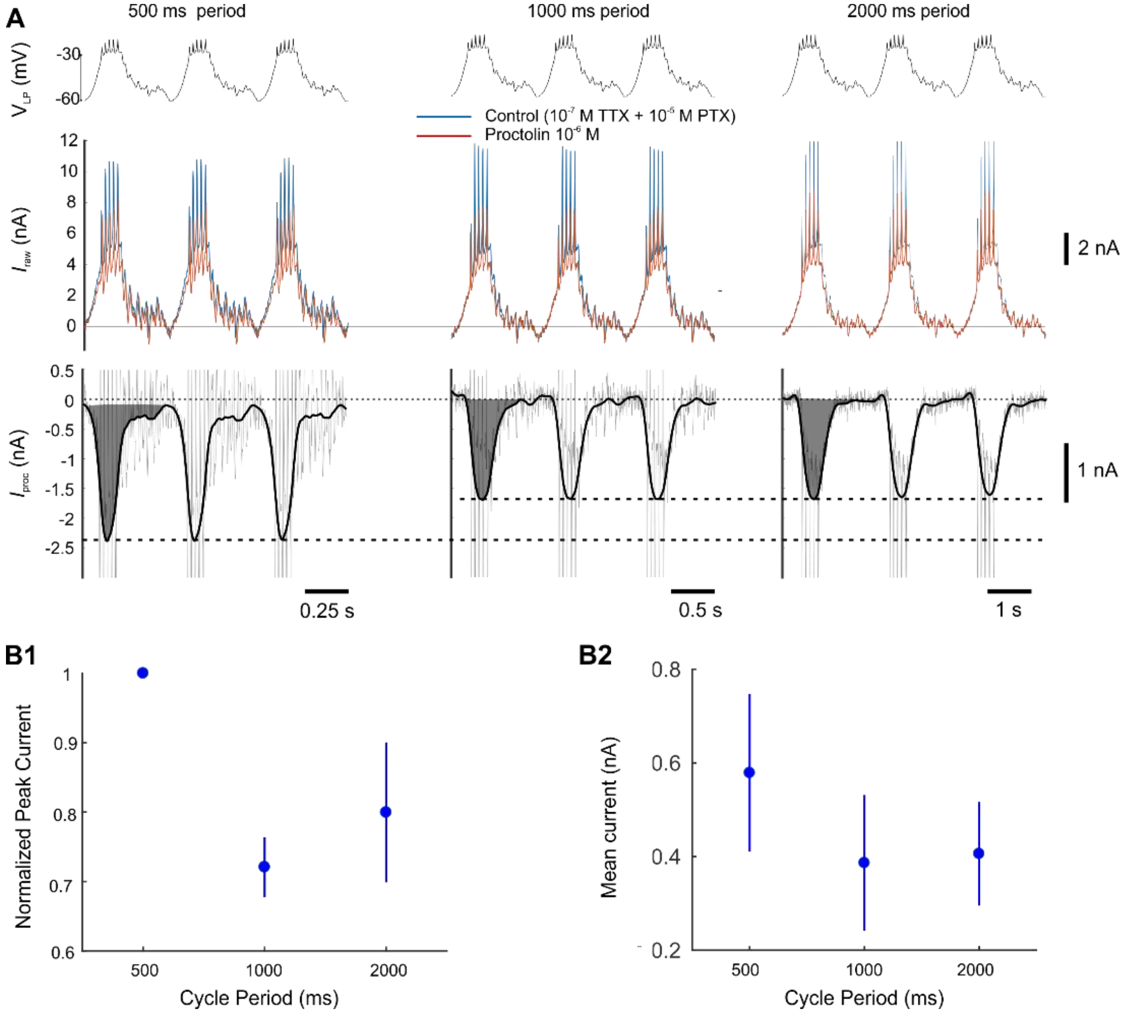

Figure 4.1 The peak and mean value of I_{proc} changes as a function of cycle period. A, Top, the LP voltage waveforms with a slow-wave amplitude of 30 mV with cycle periods of 500, 1000 and 2000 ms were used to clamp the LP membrane potential. The current (I_{LP}) was measured in control and in 10^{-6} M proctolin. The difference current (I_{proc}) was obtained by subtracting the control I_{LP} from the proctolin I_{LP} and smoothed using a median filter to remove the capacitive artifacts for quantification Dashed lines indicate the peak amplitude of I_{proc} at 500 and 1000 ms waveform periods. The shaded region in I_{proc} indicates the area over which the mean current was calculated. The minimum (B1) and mean (B2) current (mean ± SEM) as a function of cycle period (N=6). The minimum current was normalized to the minimum current at 500 ms.

Further confirmation of partial inactivation of I_{proc} could be observed by a comparison of the I_{proc} traces in sequential cycles of the LP voltage waveform at 500 ms and 2000 ms cycle periods. At 500 ms cycle period, the peak current amplitude in response to the second and subsequent applications of the unitary waveform were smaller than the first, indicating that the channel experiences inactivation that is slower than the voltage input. In contrast, the cycle-to-cycle inactivation was much less at 2000 ms cycle period. Therefore, the pyloric rhythm frequency determines the inactivation level of the proctolin-activated current and its contribution to the LP neuron activity.

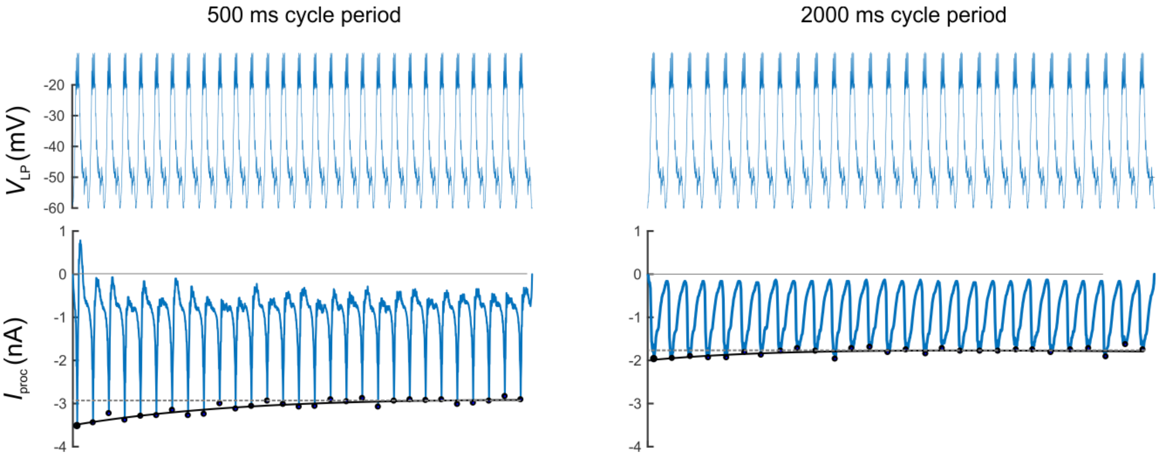

Figure 4.2 The proctolin-activated difference current I_{proc} shows more inactivation at longer waveform cycle periods. Black dots indicate the (negative) peak amplitude of I_{proc} in each cycle. Horizontal dashed line indicates the steady-state value (average of last 5 cycles) and the black curve is a single exponential decay fit. The amplitude of the decay is 0.6 nA for P=500 ms and 0.22 nA for P=2000 ms.

The amplitude of I_{proc} is sensitive to the slope and direction of voltage ramps. Thus far, we have indicated that the levels of I_{proc} may depend on its time course of inactivation. We noted that increases in the waveform cycle period were accompanied by decreases in the voltage slope. In previous studies, I_{MI}, which is a fast persistent current, has been measured using voltage ramps and the current amplitude was assumed to be independent of the ramp slope or whether the ramp was rising or falling {Golowasch, 1992 #71;Swensen, 2000 #103}. However, such a current should not show a difference in amplitude with changing the cycle period of the voltage input, as we found above with realistic waveforms. Therefore, to explore the properties of I_{proc} in the LP neuron we used symmetric voltage ramps to measure the difference current (see Methods).

In contrast with previous reports, we found that I_{proc} peak amplitude was larger with ascending ramp compared to descending ramp (Figure 4.3). Additionally, I_{proc} peak amplitude increased significantly with ramp slope for ascending ramps, but the amplitude did not change with the descending ramp slope (Figure 4.3C-D; two-way RM-ANOVA, N=14, $p < 0.001$). For the smallest voltage ramp slope, I_{proc} peak amplitude was not different between the ascending and descending voltage ramps, which suggested that the current only partially inactivates and, at this slope, it is maximally inactivated by the peak of the ramp (Figure 4.3C). These results are consistent with the waveform data and suggest that proctolin, in addition to the previously-described I_{MI}, also activates an inactivating inward current that adds to the total inward current on the ascending ramp but is at least partly inactivated on the descending ramp.

An inactivating low-threshold putative calcium current and I_{MI} are sufficient to capture the dependence of I_{proc} on waveform period and ramp slope. Our results indicating that I_{proc} depends on the waveform cycle period and voltage slope is inconsistent with the view that proctolin and other peptides only activate a single fast non-inactivating inward current, I_{MI} [27, 28].To characterize minimally the biophysical mechanisms that can reproduce the ramp currents, we built a simple computational model to explore whether a low-threshold inactivating inward current, together with I_{MI}, could reproduce these results.

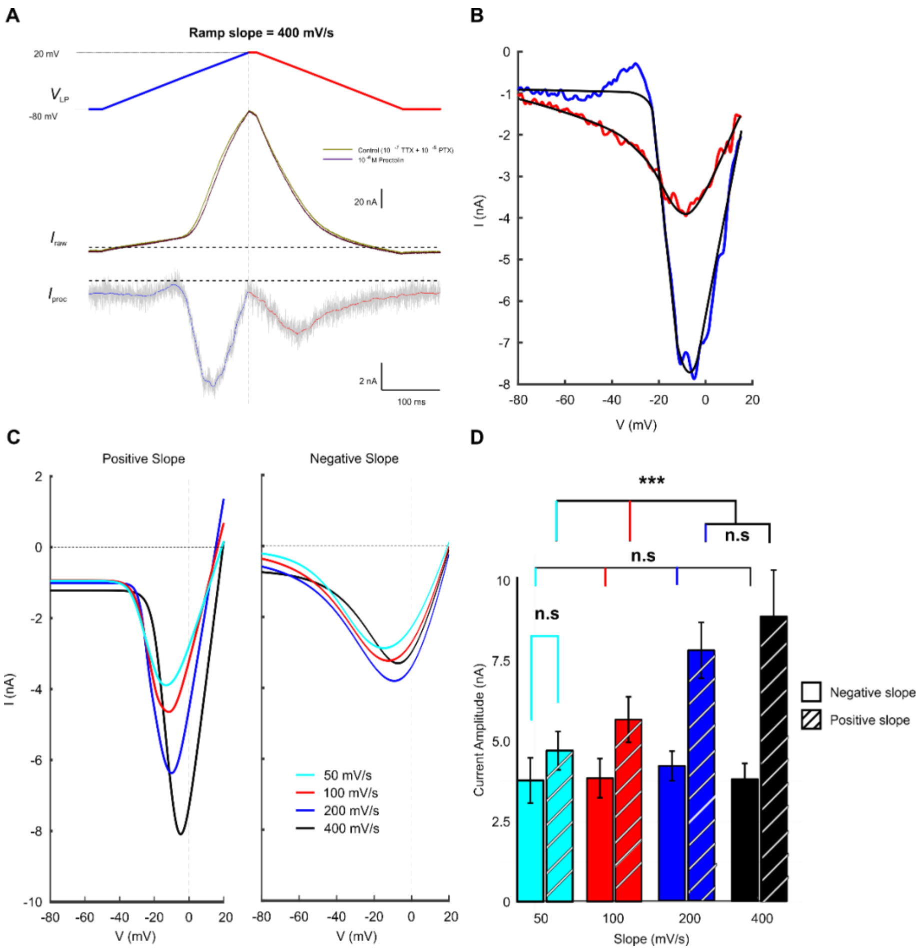

Figure 4.3 The peak amplitude of I_{proc} is sensitive to the slope of ascending but not descending voltage ramps. A1. A symmetric voltage ramp protocol was applied to the LP neuron from a holding voltage of -80mV to a peak voltage of 20mV. The voltage ramp is separated into ascending (blue) and descending (red) parts, with slopes of 400 mV/s. The voltage clamp current I_{LP} was measured in control saline (black) and in bath applied proctolin (10^{-6} M) (grey) and the difference current was defined as I_{proc}. Colors correspond to the voltage ramp protocol. A2, *I*-*V* plots of I_{proc} for the ascending and descending voltage ramps (colors corresponding to A1). B. average of fits of I_{proc} obtained from the average of 14 preparation measured on the ascending and descending voltage ramps with various slopes (top) in the voltage range given in A1. C. The absolute peak current is shown in response to voltage ramps of different slopes measured for the ascending and descending phases of the ramp. Increasing ramp slope increased the peak current for ascending but not the descending ramp. Furthermore, the current was significantly larger for the ascending ramp for large slopes.

Using a simple computational model (see Methods), we found that the experimental results could be explained by the sum of I_{MI} and a current with properties like a T-type calcium current. We refer to this putative calcium current as I_{CaProc}. The availability of the current depends on its level of inactivation. Three main properties relating to inactivation that would determine the dependence of the current on ramp and waveform cycle period: the kinetics of inactivation, steady-state inactivation and the kinetics of recovery from inactivation. We tuned the parameters associated with these properties to reproduce the dependence of I_{proc} on waveform cycle period and voltage ramp slope. The values of these parameters (Table 4.1) were in the range reported by studies in other neuron types [127].

When I_{Proc} consisted of $I_{\mathrm{MI}} + I_{\mathrm{CaProc}}$, the amplitude measured during the ascending ramp increased with ascending ramp slope. In contrast, the amplitude of this I_{proc} was not sensitive to the slope on the descending ramps (Figure 4.4A). As expected, the amplitude of I_{proc}, when it consisted of only I_{MI}, was insensitive to the ramp slope or direction (Figure 4.4B). These results suggest that the low voltage activation and rapid inactivation of I_{CaProc} are sufficient to produce the effect of ascending voltage ramps various rates without contaminating the I_{MI} response measured on descending voltage ramps.

Figure 4.4C shows the response of a model I_{proc} in voltage clamp using LP realistic waveforms at the cycle periods used in experiments. When I_{proc} consisted of only I_{MI}, the amplitude was insensitive to changes in the cycle period. In contrast, when I_{proc} consisted of $I_{\mathrm{MI}} + I_{\mathrm{CaProc}}$, the current was largest at short waveform periods (Figure 4.4D). These results suggest that the dependence of the amplitude and mean of I_{proc} on cycle period can be explained by the inactivation and recovery from inactivation of I_{CaProc}.

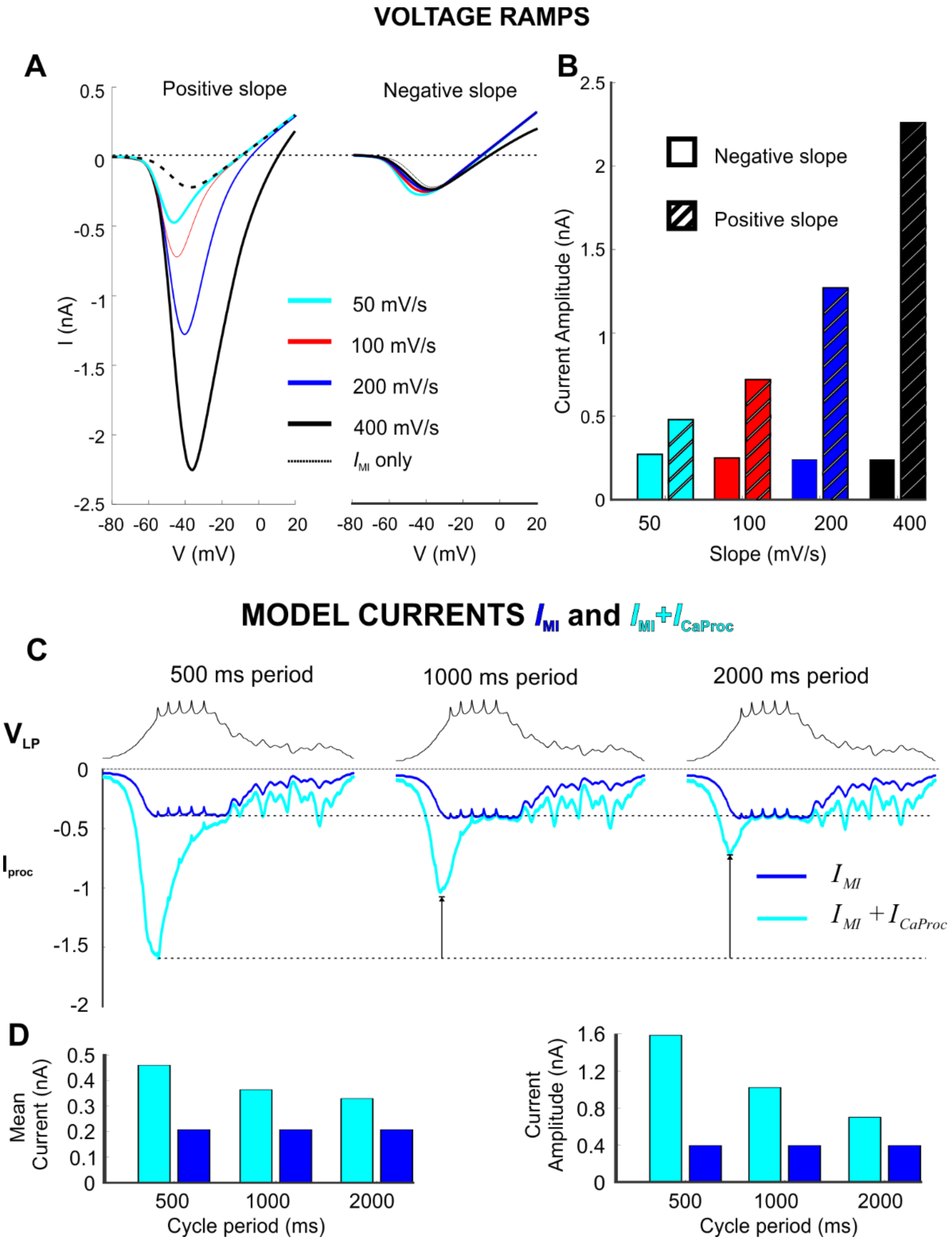

Figure 4.4 A low-threshold inactivating current (I_{CaProc}) is sufficient to reproduce the dependence of I_{proc} on voltage-ramp slope and waveform cycle period. A, The model I_{proc}, measured in response to symmetric voltage ramps of various slopes from -80 to +20 mV, shown for the ascending and descending ramps. B, The model I_{proc} peak value in response to changing the ramp slope and direction. C, I_{proc} measured in the model using realistic voltage waveforms at various cycle periods in voltage clamp. I_{proc} consisted of either only I_{MI} or a combination of I_{MI} and I_{CaProc}. Dotted horizontal lines mark the peak amplitude of I_{proc} at the 500 ms period. Arrows indicate the decrease in the I_{proc} amplitude of relative to the 500 ms period. D, The change in model I_{proc} mean value and amplitude at different voltage waveform cycle periods. Colors as in C.

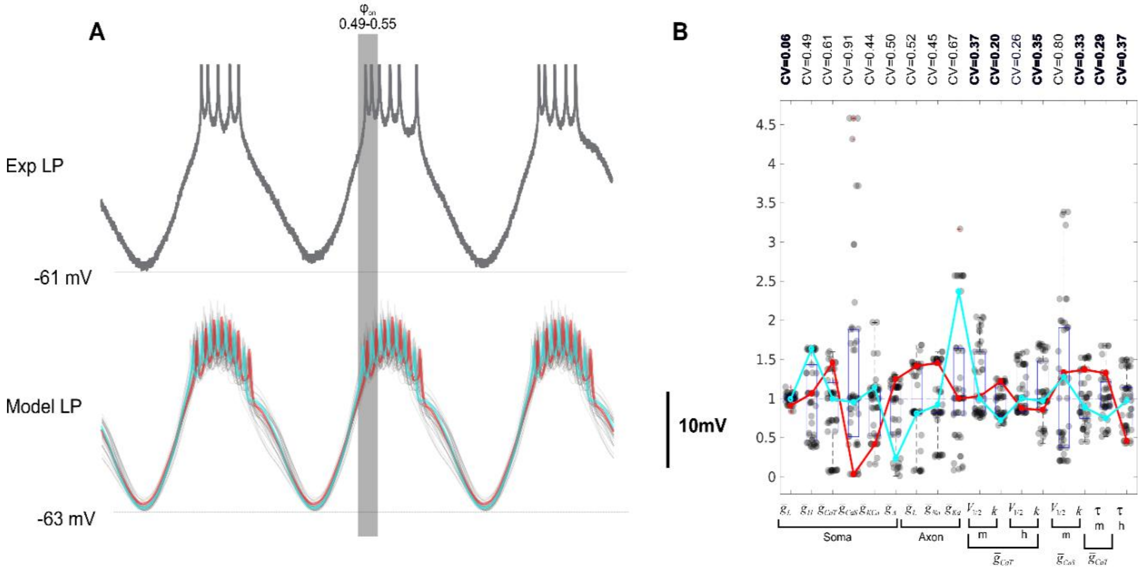

Figure 4.5 Multiple model parameter sets capture the response of the LP neuron to a 1 s cycle period realistic synaptic conductance input. A, the response of a biological LP neuron (upper trace) to a 1 s period dynamic clamp synaptic conductance input, applied in a decentralized preparation and 10^{-5} M PTX. Model LP neurons were optimized to reproduce the same response attributes for slow-wave amplitude, onset phase, burst duration and number of spikes per burst. 50 optimal models (lower traces) were selected at random from the optimal population of 300. Two of the optimal models are highlighted in cyan and red traces. B, The distribution of 17 model parameter values, with darker tones representing greater distribution density. The value of each parameter was normalized to the median value of its distribution (dashed horizontal line) for comparison. These median values are (g in µS; V, k in mV; $\boldsymbol{\tau}$ in ms): $\bar{g}_L$ =0.23 (soma); $\bar{g}_H$ =3.01; $\bar{g}_{CaT}$ =0.41; $\bar{g}_{CaS}$ =0.17; $\bar{g}_{KCa}$ =98.83; $\bar{g}_A$ = 0.73; $\bar{g}_L$ =0.59 (axon); $\bar{g}_{Na}$ =607.89; $\bar{g}_{Kd}$ =144.46; $\bar{g}_{CaT}$ m_∞ $V_{1/2}$=-29, k = 9.29; $\bar{g}_{CaT}$ h_∞ $V_{1/2}$=-49.63, k = 9.41; $\bar{g}_{CaS}$ m_∞ $V_{1/2}$=-12.33, k = 9.21; $\bar{g}_{CaT}$ τ_m =47.77, τ_h =528.25. In these simulations $\bar{g}_{MI}$ and $\bar{g}_{CaProc}$ were set to 0. Two model parameter sets, corresponding to the highlighted traces in panel A, are shown for comparison (cyan and red), indicating that models that exhibit similar traits did not require a consistent relationship among their parameters. Eight of the 17 model parameters were relatively tightly constrained by the optimization (bold-faced CV: coefficient of variation < 0.4) in all optimal models.

The functional effects of the proctolin-activated currents in the LP model neuron. In order to examine the functional consequences of the dependence of I_{proc} on cycle period, we used a detailed computational model of the LP neuron (see Methods; Table 4.1) and quantified the model LP neuron activity parameters during ongoing oscillations. Ionic currents in identified STG neurons are known to have variable maximal conductances across preparations [17, 49]. We therefore examined the effect of the proctolin-activated currents not on a single LP neuron parameter set, but rather a family of LP model neurons with distinct parameter sets, all of which produced the same (optimal) activity pattern at a cycle period of 1 s. To produce such a family, the model neuron activity was optimized in response to a 1 s realistic synaptic conductance input, using a multi-objective evolutionary algorithm (see Methods), to match the response attributes of a biological LP neuron driven with the same dynamic clamp synaptic conductance (Figure 4.5A). Since neuromodulatory input to the STG had been removed by decentralization, we our optimized models had no I_{MI} or I_{CaProc}.

The response attributes that were fit were: the slow-wave amplitude (21mV), minimum voltage, burst onset phase (55%), number of spikes per burst (5) and burst duration (125ms). The parameter values of the maximal conductances in the population showed considerable variability (Figure 4.5B) but the low-threshold transient calcium current parameters were constrained relative to all other parameters. We then subjected random subset of 50 optimal models (chosen from among 300) to synaptic conductance inputs with 500, 750, 1000 and 2000 ms cycle period, and recorded the mean and standard deviation of the burst onset phase, duty cycle (burst duration/cycle period), and slow-wave amplitude (see Methods). For these 50 models, we compared the relative actions of I_{MI} and I_{CaProc} in changing these values at each cycle period. We predicted that, due to its transient time-dependent properties, I_{CaProc} would affect one or more properties mainly at shorter cycle periods because, at large periods, it would be more inactivated.

Table 4.3 Response features of optimal LP models across a range of frequencies.

	Cycle Period (ms)			
	500	750	1000	2000
φ_{on}	0.69±0.60	0.60±0.015	0.55±0.01	0.46±0.01
Slow-wave amplitude (mV)	14.79±0.72	17.65±0.59	19.28±0.63	20.95±1.05
Duty Cycle	0.16±0.06	0.27±0.05	0.30±0.03	0.34±0.04

Values of burst onset phase, slow-wave amplitude, and duty cycle (mean ± std) measured across the 50 randomly selected optimal models.

We assessed the effect of adding I_{MI} and I_{CaProc} separately or together on the response dynamics of the LP model neurons in response to synaptic conductance inputs of different cycle periods. We found that, independent of the variability in intrinsic baseline model parameters, adding I_{MI} alone was more effective at advancing phase relative to control at small cycle periods (Figure 4.6A). This was because both the amplitude and phase of all models was decreased and delayed in response to 500 ms inputs and so I_{MI} provided the depolarizing drive to offset this frequency-dependent change in amplitude and thus the time it takes to reach spike threshold.

We found no difference in the onset phase relative to control between adding I_{CaProc} alone or together with I_{MI} (Figure 4.6A). To understand the effect of I_{CaProc} on onset phase on top of the action of I_{MI} and if the effect of I_{CaProc} depended on the level of I_{MI}, we plotted the change in onset phase when I_{MI} and I_{CaProc} were added together relative the effect of I_{MI} alone (Figure 4.6B). We found that the effect of I_{CaProc} in advancing phase depended on the maximum conductance of I_{MI}, since the additional effect of I_{CaProc} decreased for all cycle periods and was not different from I_{MI} alone at 2000 ms period (Figure 4.6B).

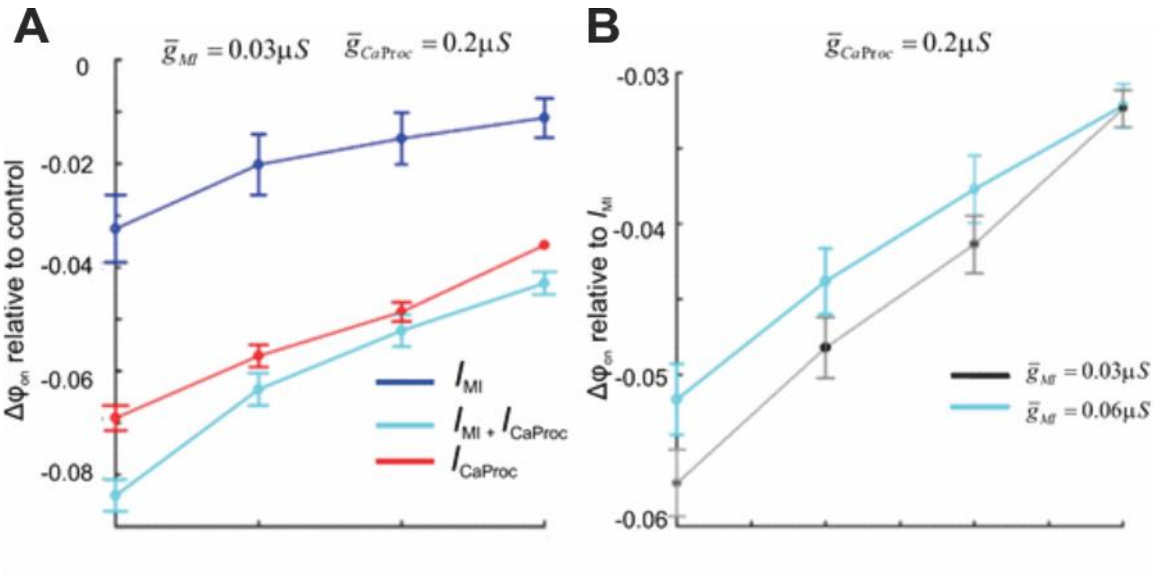

Figure 4.6 Proctolin-activated I_{CaProc} produces a phase change at small cycle periods but its effect depends on the level of I_{MI}. A, The LP model neuron phase change relative to control, plotted as a function of waveform cycle period in the presence of I_{MI} alone, $I_{CaProc} + I_{MI}$ and I_{CaProc} alone. B, The effect of increasing cycle period on the onset phase for the $I_{CaProc} + I_{MI}$, normalized to the onset phase for the I_{MI} only condition, at each frequency, for two baseline values of $\bar{g}_{MI} = 0.03$ and 0.06 µS.

Using dynamic clamp to assess the functional effects of the proctolin-activated currents in the biological LP neuron The LP computational model neuron predicted in the presence of I_{MI}, the time-dependent properties of I_{CaProc} produce larger decreases in the burst onset phase at short cycle periods. To examine whether these predictions bear out in the biological system, we used dynamic clamp to introduce different levels of I_{MI} and I_{CaProc} into the synaptically isolated LP neuron, while it was driven by a dynamic clamp synaptic conductance inputs at different cycle periods (Figure 4.7A).

For the same set of cycle periods used in the model, we found that addition of I_{CaProc} changed both the amplitude and onset phase relative to both control and injection of dynamic clamp I_{MI} (Figure 4.7B). As in the comparable manipulations of the computational model (Figure 4.6), we measured the effect of injection of I_{CaProc} on the onset phase relative to control and found that the onset phase was significantly larger during 500ms cycle period inputs than for other longer periods. However, in contrast to the model, injection of I_{MI} alone did not produce any changes in onset phase as a function of cycle period (Figure 4.7C).

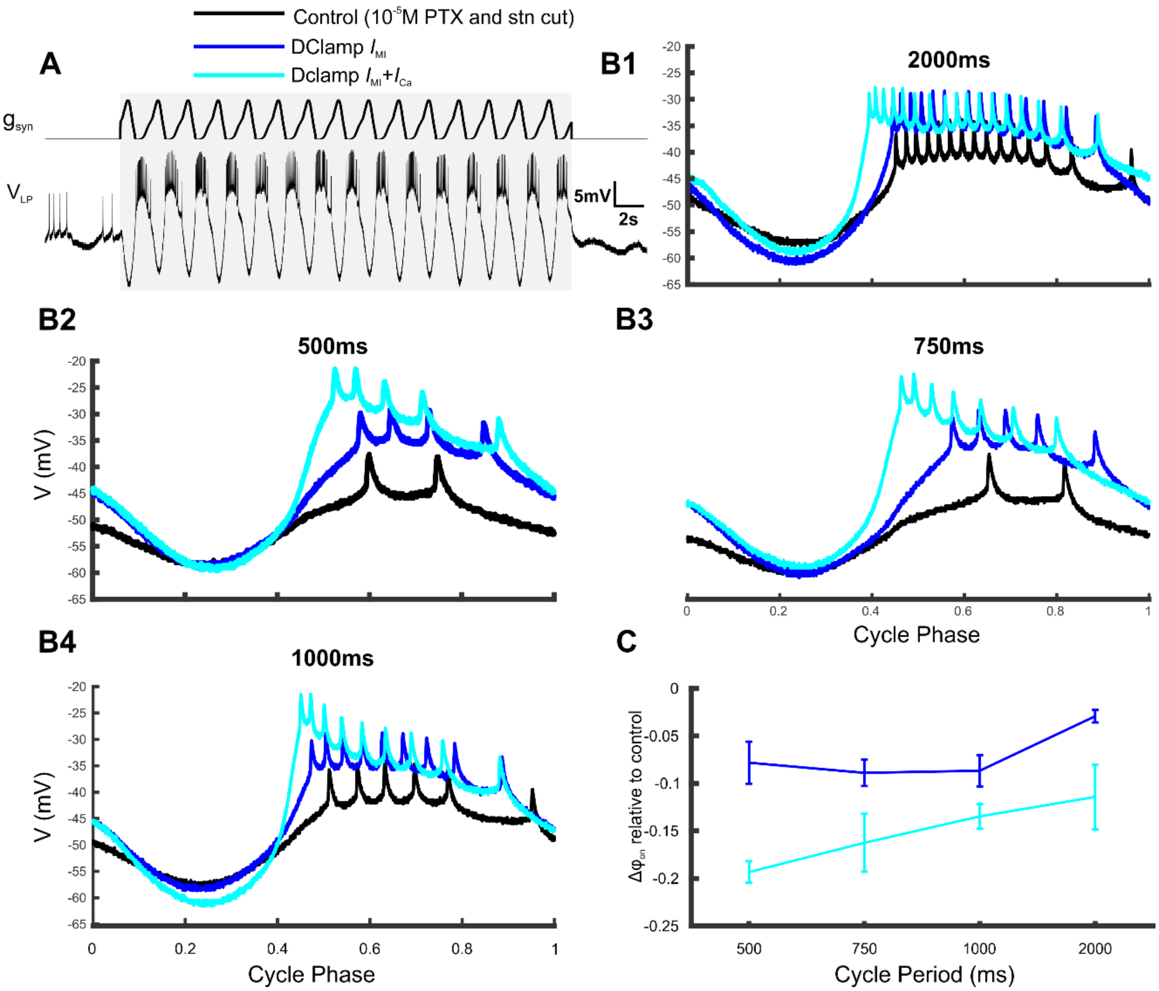

Figure 4.7 Adding I_{MI} and I_{CaProc} is more effective than I_{MI} alone at advancing onset phase. A, The voltage response (V_{LP}) of the synaptically isolated LP neuron to dynamic clamp injection of artificial synaptic conductance (g_{syn}) inputs in control conditions. The dClamp manipulations were run for 30 s to that the LP response reaches steady state. B, The response to the last cycles of g_{syn} injection at different cycle periods (B1-B4) was extracted to measure the burst onset phase in control and with the dynamic clamp addition I_{MI} alone and $I_{\mathrm{MI}} + I_{\mathrm{CaProc}}$. C, The LP neuron phase change relative to control plotted as a function of cycle period.

Proctolin produces larger phase advances at shorter cycle periods. To test whether the effect of bath application of proctolin is comparable to dClamp injections of I_{CaProc} and I_{MI}, we drove the LP neuron at different cycle periods (with a dClamp synaptic conductance) in control and in low (10^{-7} M) and high (10^{-6} M) concentrations of proctolin. We then compared the LP burst onset phase in proctolin to the phase measured in control saline during dClamp current injection.

At cycle periods $\geq$ 1000 ms, neither concentration of proctolin produced a change in phase compared to control saline with no additional current, or control saline with only dClamp I_{MI}. However, at cycle periods < 1000 ms, whereas the onset phase change in low concentration proctolin resembled that observed with dClamp I_{MI} alone, large concentrations of proctolin produced a phase change comparable to dClamp $I_{\mathrm{MI}} + I_{\mathrm{CaProc}}$. These findings suggest that the influence of proctolin on the activity phase of the LP neuron is comparable to the combination of dClamp I_{MI} and I_{CaProc}.

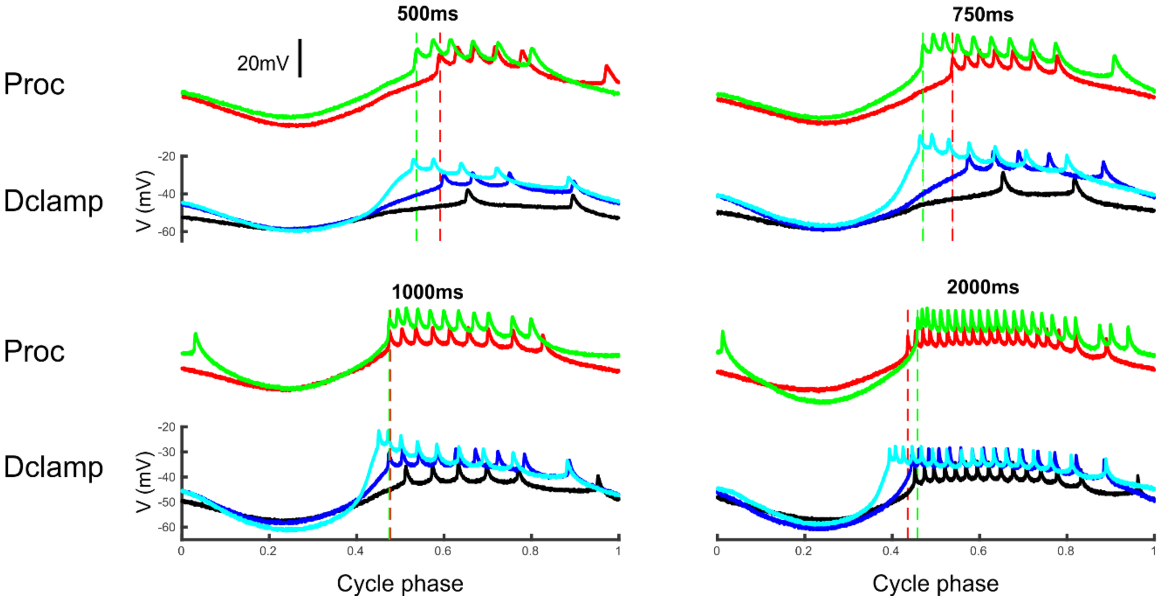

Figure 4.8 The frequency-dependent effect of proctolin on LP onset phase is comparable to dClamp I_{MI} and I_{CaProc}. In each panel: top, LP voltage in response to synaptic conductance input in the presence of low (10^{-7} M, red) and high (10^{-6} M, green) concentration of Proctolin. In each panel: bottom, a comparison with the LP voltage in response to synaptic conductance input in control (black), with dClamp I_{MI} (blue), and dClamp $I_{\mathrm{MI}} + I_{\mathrm{Ca}}$ (cyan). Dashed lines are used to compare the onset phase in the presence of low and high concentrations with that observed during dClamp injection.

4.4 Discussion

We have identified a frequency-dependent mechanism underlying the proctolin control of burst onset phase in a follower neuron in an oscillatory network. Underlying this frequency-dependent effect was the activation of at least two inward currents with distinct voltage- and time-dependence. The identification of a time-dependence of the proctolin-activated currents is novel and in contrast to those who previously studied the properties of this current [17, 28]. The pyloric rhythm maintains its pattern over a range of frequencies [17] by keeping the phase of the component neurons constant. The time-dependence of the proctolin-activated currents may play a role in the phase maintenance of burst onset.

Furthermore, neuromodulators show state-dependent actions [33] so that the activity determines the extent or sign of modulator action [122]. We showed that the activity of a neuron given by the steady-state frequency could account for the state-dependent actions of neuromodulators on individual neurons. The action of a neuromodulator preferentially advanced phase and duty cycle at high frequencies, by virtue of the properties of the time-dependent inactivation of an inward current activated by proctolin.

Although I_{MI} is a fast persistent current, across animals the amplitude of I_{MI} is positively correlated with the phase of synaptic inputs [17] which may suggest an inactivating property. In support of this, a recent study suggests that a peptide modulator elicits low-threshold inactivating transient inward currents, in addition to I_{MI}, in a stomatogastric neuron [41]. The inactivation time-dependence of the low-threshold current was shown to interact with I_{MI} to promote post-inhibitory rebound bursting.

Therefore, a neuromodulator may modify multiple physiological mechanisms, but it would do so in frequency ranges constrained by the time scale of ionic current kinetics.

Our approach of using realistic waveforms to drive LP in voltage-clamp to measure modulator-activated difference current at different frequencies was a novel one. If proctolin-activated current were fast and non-inactivating, as previously suggested [17, 28], then the properties of the current would be independent of cycle period. Using this method, we were able to reliably identify transient inactivating currents by showing that both the absolute peak current and mean current decreased with increasing cycle period. Surprisingly, increasing the amplitude of the realistic waveform slightly decreased the peak current at all cycle periods relative to 500ms, but did not produce similar decreases in the mean current. This may imply that the activation of a transient component is activated more strongly in voltage range of LP activity (usually ~ -30mV peak slow-wave potential [17])

The fast, voltage-dependent inactivation implies a current similar to T-type calcium currents, which may provide an important intrinsic mechanism to regulate multiple dynamic processes such as onset phase and burst duration. Our ramp protocols also pointed towards proctolin targeting an inactivating inward current with distinct dynamics to the previously identified I_{MI}. This current was sensitive to voltage ramps on the rising and not falling phase. Furthermore, even at fast voltage ramps the current on the rising phase was largely inactive at the beginning of the falling phase, thus suggesting a low-threshold fast inactivating inward current. However, further studies are needed to identify the biophysical phenotype of this current.

Recent work using the related neuropeptide CabPK in the LG neuron of the gastric mill neuron showed that multiple currents including I_{MI} plus both slow and fast activating transient, low-threshold inward currents [41]. Here, we demonstrated that proctolin may activate I_{MI} and at least one other voltage-dependent inward current with distinct voltage-dependence and kinetics in the pyloric LP neuron. Although these additional currents were not identified with pharmacological blockers, another study showed that only the additional time-dependent currents, and not I_{MI}, were sensitive to replacing the extracellular Ca^{2+} with Mn^{2+}, a Ca^{2+} channel antagonist [41]. We therefore, carried out our study with the assumption that this additional current was a fast-activating transient calcium current.

In conclusion, this study provides a plausible mechanism to explain why the action of a neuromodulator can be altered by the activity of neurons. Previous work showed a state-dependent action of proctolin on the pyloric cycle period promotes network oscillations at 1 Hz cycle frequency producing larger increases in slow rhythms as compared to faster ones [33]. Here, we show that the actions of proctolin on individual neurons may depend on the activity of the target neuron. Due to the time-dependent properties of ionic currents in the target neuron, the neuromodulator may alter features of activity in a frequency-dependent manner. We showed that these features may include the onset of spiking or rebound burst phase and duty cycle. However, the frequency-dependent effect depends on the level of modulator-activated persistent currents. Therefore, it is plausible that these modulator-activated currents are expressed in individual neurons with precise ratios to achieve frequency-dependent effects. Understanding the physiological conditions under which time-dependent currents produce reliable phase changes, i.e. whether and how they interact with other intrinsic regenerative phase-promoting inward currents remains to be determined.

CHAPTER 5

CONCLUSION AND DISCUSSION

5.1 Purpose and goals

The primary purpose of this thesis was to understand the biophysical control of frequency-dependence in neurons and determine whether short-term actions of neuromodulators depend on the frequency of oscillation. The goals of this dissertation were threefold: 1) to understand the interaction of multiple resonant ionic currents in the generation of MPR in pyloric pacemaker PD neurons; 2) to understand how frequency-dependent responses shape network activity; 3) to examine the frequency-dependent actions of neuromodulation. As a model system, we used the pyloric network of the crab *Cancer borealis* and used a combined experimental and computational approach to accomplish these goals. Based on the results presented here, I conclude that the kinetics of inactivating currents not only are important for generating preferred frequency responses in neurons but also alter the action neuromodulators have on network activity.

The first goal was accomplished by measuring the MPR as reflected in the Z- and φ- profiles of biological PD neurons in voltage clamp. I then used a genetic algorithm to obtain multiple biophysical models with unique combinations of parameter values constrained by biological measurements of ionic currents. I used the fact that the resonance frequency and zero-phase frequency were identical in these models to explain the dependence of MPR properties on the kinetics of ionic currents. The second goal was accomplished by measuring unique changes in the MPR of distinct neuron types by the same neuromodulator, and computationally exploring the consequences of such changes on the activity of neurons in a simplified two-cell reciprocal inhibitory network. The third goal was accomplished by measuring neuromodulator-activated ionic currents in voltage-clamp using realistic waveforms and ramps of various cycle periods and voltage slopes respectively. Using computational modeling, I identified a fast inactivating inward current, I_{CaProc}, proposed to be a target of the neuropeptide proctolin in addition to I_{MI}, to explain the frequency-dependence of the proctolin-activated current. This was shown experimentally using realistic LP voltage waveforms and voltage ramps of various cycle periods and slopes. To determine the effects of a fast inactivating inward current on the activity of the LP neuron, I used a combination of modeling and dynamic clamp. In particular, I explored the effect of such currents on the onset spiking phase in response to realistic synaptic inputs in both a family of computational models that produce LP-like activity and in biological LP neurons using the dynamic clamp technique. In both approaches, I used specific ratios of the maximal conductances of transient and persistent neuromodulator-activated currents during rhythmic inputs at various frequencies and measured changes in onset spiking phase.

5.2 Main Results

In this section, I explore the general findings related to the question addressed in each chapter.

5.2.1 Chapter 2: Mechanisms of Generation of Membrane Potential Resonance in a Neuron with Multiple Resonant Ionic Currents

In this chapter, I was interested in understanding how multiple resonant ionic currents interact to generate MPR in the pyloric pacemaker PD neuron. To address this, I measured the MPR of PD neurons using voltage-clamp. Two caveats must be addressed, namely the use of voltage clamp and PD electrical coupling. Voltage clamp has been used previously for this purpose, and it gives comparable f_{res} measurements to those calculated when using current clamp [29, 62, 70]. The PD neuron is electrically-coupled to other pyloric neuron types that include the anterior burster neuron (AB) and two lateral posterior gastric neurons (LPG). Furthermore, previous studies have shown that the resonance frequency can influence the frequency of oscillations though electrical coupling [9]. Thus MPR measured in PD could result from network interactions. However, previous work in our lab demonstrated that MPR in PD is independent of its electrical coupling to the AB neuron [4].

To understand how MPR is generated in the PD neuron in voltage clamp, I used a data-driven approach. More specifically, I constructed a biophysical model that was parameterized by equations associated with two ionic currents, I_{H} and I_{Ca}, which were thought to shape MPR in the PD neuron. Since the attributes of the Z- and φ-profiles were relatively stable across different animals and the maximal conductances of ionic currents are variable [60], I used an MOEA to obtain multiple combinations of parameter values associated with I_{H} and I_{Ca}. I found models that fit the experimental data with high accuracy without needing to consider additional ionic currents. We therefore, examined the population of parameter sets to understand their contribution to MPR.

The first key finding from this chapter includes the fact that multiple combinations of parameter values can produce MPR. At the same time, I observed correlations between parameters defining the same and different ionic currents. Using a sensitivity analysis, I found specific correlations maintained the values of Z-profile attributes. In particular, the $\tau_m - \tau_h$ correlation associated with the time constants of I_{Ca} gating variable, maintained f_{res}. In addition, the $\bar{g}_{Ca} - V_{1/2}^{h_\infty}$ correlation also associated with I_{Ca}, maintained Q_Z, without affecting f_{res}. Furthermore, the $\bar{g}_H - \bar{g}_{Ca}$ correlation was present in a subpopulation of models that produced appropriate changes in fres and Z_{max} as the V_{low} of the voltage ZAP was decreased. Other studies failed to see correlations in parameter values in models containing multiple resonant currents [43, 72]. This may be because voltage-clamp used in our study restricted the voltage range of the neuron and thus limits the contribution of I_{Ca} and I_{H} with nonoverlapping activation voltage ranges.

Although I did not refute the possible role of additional currents in influencing the Z- and φ-profiles, it is unlikely that they would have a major influence on the correlations I found. I used voltage clamp to limit the role of currents activated at higher threshold. In the crab PD neuron, I_A does not activate more than 5% at -30 mV (the equations are in [94]). Additionally, [4] explored the role of several other ionic currents on resonance with pharmacological blockers, and I could therefore exclude those that had no effect.

In the biological PD neuron and the good fit models, I found that the f_{res} and $f_{\varphi=0}$ were nearly identical, which was not reported previously. Whether this is because MPR was measured in voltage clamp and not current clamp or due to the unequal contributions of non-overlapping resonant currents requires further investigation. Nonetheless, I used the equality in these frequencies to explain the dependence of f_{res} on the kinetics of individual ionic currents. Specifically, I showed that MPR occurs at a given frequency because the amplitude is largest when it is synchronized with voltage inputs. Any parameter that shifts the phase of ionic currents also shifts the frequency at which that ionic current is maximum and therefore f_{res}. I believe this to be a general rule for how MPR is generated in voltage clamp by one or many ionic currents.

A previous study incorporating these currents in a model of hippocampal pyramidal neurons saw resonance (f_{res}) without phasonance ($f_{\varphi=0}$) [43]. However, phasonance could be restored by making the inactivation time constant of a low-threshold I_{Ca} slower. This is consistent with our result and suggests that PD neurons show resonance and phasonance, whereas CA1 pyramidal neurons only show resonance because PD neurons have a low-threshold I_{Ca} whose inactivation is much slower than in CA1 pyramidal neurons. For instance, in our models the average inactivation time constant was ~450 ms, whereas in [43] it was 30 ms.

5.2.2 Chapter 3: Biophysical Mechanisms of Modulator-induced Antiresonance and its Functional Role in an Oscillatory Network

In this chapter I was interested in understanding if neuromodulators have different effects on neurons with distinct MPR properties which interact in an oscillatory network. My findings showed proctolin modulates the MPR of the PD pacemaker neuron and the LP neuron but had differential effects on the shape of the *Z*-profile. Consistent with other studies, proctolin amplifies PD MPR by increasing the Z_{max} without changing f_{res}. In contrast, proctolin switches the *Z*-profile of the LP neuron from having only a single resonant peak to a *Z*-profile where $Z(f)$ shows a minimum at low nonzero f (antiresonance) followed by a shift in f_{res} to higher frequencies. This more complex *Z*-profile shape has been experimentally reported in hippocampal interneurons [6] and the antiresonance has been proposed to suppress activity in the theta range of frequencies in which CA1 pyramidal neurons are most excitable. However, the functional consequences were not explored in previous studies.

I provided a simple mechanism for the differential effects of proctolin on the *Z*-profile of the PD and LP neuron, which is related to an increase in I_{MI}, I_{Ca} or both. A simple amplification could occur by either an increase in I_{MI} or I_{Ca}. Since both neurons express a calcium-dependent potassium (I_{KCa}), the generation of antiresonance in LP could be related to the modification of voltage-dependent activation time constant of I_{KCa}, which followed the changes in intracellular calcium concentration. Such changes in intracellular calcium concentration could be achieved by an increase in a low-threshold I_{Ca} that generates MPR or a yet undescribed current that is added by proctolin. These findings underline a novel aspect of neuromodulation, where rich dynamics in the rhythmic output of oscillatory networks are produced by a single neuromodulator differentially altering the MPR properties of specific neurons.

Furthermore, I computationally explored the consequences of differential modulation of neurons that interact in an oscillatory network. To do this, I constructed linear models that showed resonance or antiresonance. Previous computational studies [7, 8] used similar linear conductance-based models to show how additional ionic currents operating at various time scales modulate existing resonance generated by 2D models. It was shown that a 3D model having an additional current that contribute a slow positive feedback can produce antiresonance [8] but antiresonance was less pronounced when Z_0 .was unchanged My experimental observation of the change in the Z-profile of the LP neuron by proctolin suggested that additional ionic currents that contribute a slower negative feedback are also activated. Therefore, I used a 4D linear model to capture this effect and found that the underlying mechanism for the generation of antiresonance.

In contrast to nonlinear conductance-based models, the use of linear models greatly facilitated our ability to control f_{res} and other resonance attributes independently. I changed the values of the resonator parameters in such a way that antiresonance was generated with no effect on Z_0, f_{res}, and $Z_{\max}$. This required changing more than one biophysical parameter at a time in a manner consistent with previous work [8]. This ensured that the observed effects are directly due to the antiresonance at low frequency oscillatory inputs and not due to other changes in the shape of the *Z*-profile.

Our first result using linear models to examine antiresonance effects through network interaction showed that antiresonance can reduce feedback inputs to limit amplification in the low frequency range of the *Z*-profiles of postsynaptic neurons. I showed that this was due to antiresonance because a 2D resonator with identical Z_0, f_{res}, and $Z_{\max}$ produced a bigger amplification at low frequencies but an equal amplification relative to the antiresonator model. Our second result using linear models to examine antiresonance effects through network interactions showed that antiresonance produces smaller changes in the period of an intrinsic oscillator through reciprocal inhibition.

The method of changing *Z*-profile attributes without changing other attributes to examine the effects on network activity was also used previously [9]. Previous work showed that network effects in an electrically-coupled network were due to the *Z*-profile and were independent of parameter values chosen. My results showed a causal relationship between antiresonance and both the shape of *Z*-profiles and oscillation period of a linear model neuron and an oscillator model neuron in a two neuron synaptically-coupled network. However, similar to [9] further work is needed to show that these network effects hold for a wide range of parameters for neurons in a two-neuron synaptically-coupled network. Moreover, at least for a synapse with no dynamics, the antiresonance effects do depend on the values chosen for synaptic parameters and so future work should characterize the contribution of antiresonance to the modification of the Z-profile of synaptically-coupled neurons.

I examined the effects of changing sets of parameters associated with ionic currents that contribute slow feedback to the subthreshold response to oscillatory inputs. Biologically, these changes may be achieved by simultaneous modulation of multiple parameters associated with distinct voltage-gated ionic currents to alter network dynamics. My biophysical conductance-based modeling suggests that at least in the LP neuron of the crab, these effects are embodied in the complex interaction between I_{Ca} and I_{KCa}.

Our results also have implications for the activity of the pyloric network. The pyloric network activity is driven by the AB/PD pacemaker group, including one AB electrically coupled to two PD neurons. The LP neuron provides the sole chemical synaptic feedback to the pacemaker group. Previous studies have shown that it can potentially alter the rhythm period generated by the pacemaker group [110]. Other studies show that the synapse has no effect in spite of several-fold increases in its strength [131], or that the synapse serves to make the rhythm frequency more robust under control conditions [132]. My findings suggest that the emergence of antiresonance in the LP neuron may act to stabilize the pacemaker group oscillations by preferentially amplifying PD resonance by reducing inhibitory feedback at low frequencies.

The effects on oscillator period through chemical synaptic coupling could be partly due to the φ-profile. In model neurons that produce MPR, at some special frequency, $f_{\varphi=0}$, the neuron will synchronize with its input [73]. In networks of spiking neurons coupled with spike-mediated synapses, $f_{\varphi=0}$ of individual neurons predicts the frequency of network activity [133]. My study predicted that resonant or antiresonant neurons have minimal effect on the frequency of an oscillator neuron at frequencies near $f_{\varphi=0}$ and antiresonance increased the range of frequencies over which the oscillator period was minimally affected (Figure 3.8).

Additional ionic currents, which contribute amplifying and resonant variables in linear models, that change the *Z*-profile, also affect the φ-profile [8]. We chose to use a 4D linear model because in 3D models the antiresonance phenomenon is less pronounced for increases in a slow amplifying variable that would not affect input resistance [8]. This indicated that a combination of resonant and amplifying variables was required to generate antiresonance while leaving input resistance unchanged. However, the interaction between these two variables in shaping the φ-profile is unclear. Previous work showed that the addition of a slow resonant variable to 2D models increases the maximum phase advance and increases $f_{\varphi=0}$. In contrast, the addition of a slow amplifying variable to 2D models seems to have opposite effects [8]. To better understand how these two variables interact to shape the φ-profile, additional work should be carried out that examines the effects of increasing the values of the effective ionic conductances while keeping their sum constant and measuring the effect on attributes of the φ-profile.

Previous studies have shown some neuromodulators such as proctolin can have extensive cellular and synaptic effects on the pyloric network. [13]. Our results suggest that a part of these modulatory effects on the neurons of the pyloric network can be attributed to alterations in the *Z*-profile of interacting neurons. I found that at low concentrations of 10^{-7} M proctolin there was little effect on the *Z*-profiles of the PD and

LP neurons. However, such concentrations have been shown to affect other aspects of pyloric network activity such as phasing of pyloric network neurons [34].

5.2.3 Chapter 4: Frequency-dependent Actions of Neuromodulation

Neuromodulators alter pyloric network output through modification of the properties of neurons and synapses [34, 105]. The action of neuromodulators on network output depends on prior network activity or state [32, 33]. Similarly, neuromodulators can have frequency-dependent effects [35]. In this chapter, I examined the hypothesis that the effect of neuromodulators on the activity of individual neurons depends on the frequency of oscillation.

I addressed this hypothesis by recording neuromodulator-activated voltage-gated ionic currents using prerecording realistic unitary waveforms in voltage clamp. I measured the frequency-dependence in the modulator-activated current by scaling the cycle period and measuring changes in the current. To our knowledge, this approach has not been used before for the investigation of frequency-dependence of neuromodulation. This method opens up future studies to understand the contribution of other neuromodulator-activated currents to the generation of rhythmic activity at different frequencies.

Our findings show that the effect of proctolin depends on the frequency of membrane potential oscillations. Using realistic LP voltage waveforms I showed that the proctolin-activated current in the LP neuron was dependent on the waveform period and slope. The largest current response occurred in response to shorter waveform period and steep voltage slopes. Modeling using I_{MI} and low-threshold rapidly inactivating calcium current I_{CaProc}, similar to T-type calcium currents, showed that the larger response at short waveform periods is due to the rapid time-dependent inactivation and recovery from inactivation. Furthermore, the frequency-dependence of I_{proc} relied on the ratio of I_{CaProc} to I_{MI}. The frequency-dependence was contingent upon I_{CaProc} dominating at early phases of the cycle period and I_{MI} dominating at later phase due to its persistent activation. This suggest that the effects of neuromodulators depend on the frequency of oscillation due to the relative contributions of multiple ionic currents with distinct voltage- and time-dependence.

Using computational modeling and the dynamic clamp technique, with the LP neuron as an example, I showed that the activation of I_{CaProc} produced changes in the spiking activity, which depended on the oscillation cycle period. In particular, the larger decreases in onset spike phase were seen at short cycle periods. Reduction of T-type currents expressed in thalamic reticular neurons increased the threshold for burst firing and produced a delay in the onset of bursting [134]. I proposed that this effect was due to I_{CaProc} as it depended on inactivation properties similar to other fast-inactivating T-type currents [125, 127]. Furthermore, fast inactivating inward currents, which are calcium-dependent are targeted by neuropeptides in other STG neurons and calcium-dependent in addition to I_{MI} [41].

Our findings suggests I_{CaProc} has properties similar to the T-type calcium currents, [125]. The fast recovery from inactivation allows I_{CaProc} to produce an inward current at short waveform cycle periods. I showed that, for a given half-inactivation voltage, an inhibitory synaptic input would produce the largest current when the cycle period was short. The duration of the synaptic input scales with cycle period. Therefore, short cycle periods result in short duration synaptic inputs. Such inputs gave larger currents because the inactivation gate was too slow relative to the synaptic input. In contrast, longer duration synaptic inputs (corresponding to long cycle periods) allows the relatively quick inactivation gate to close, and thus decrease the current. These findings demonstrated that the inactivation properties of ionic currents could account for the frequency-dependent effects of neuromodulator-activated currents. To our knowledge, the use of realistic voltage waveforms at different cycle periods had not been used before to examine frequency-dependent properties of neuromodulators.

My study indicates that I_{CaProc} could lead to post-inhibitory rebound (PIR) burst firing. PIR bursting often involves the complementary influence of multiple voltage-gated ionic currents. Non-inactivating ionic currents move the membrane potential into the activation range of additional currents. These currents are usually inactivating T-type calcium currents [41, 135]. Previous studies examined the interaction of the non-inactivating inward current, I_{MI}, with a slowly inactivating inward current and found that PIR bursting was promoted by I_{MI} [41]. However, increases in I_{MI} led to decreases in the PIR effects of I_{CaProc}, which inactivates much faster than the inactivating current used in [41]. Therefore, further work is needed to characterize how the effect of ionic currents with different inactivation rates on PIR depends on fast non-inactivating inward currents, such as $I_{\mathrm{MI.}}$ One could measure the effect of phase as a function of cycle period when the inactivation rate of ICaProc is either slow or fast and then show that I_{MI} promotes PIR for slower inactivation rates.

5.3 General Discussion

There were three separate but inter-related aims of this thesis. The first was to understand the biophysical mechanisms that shape the MPR of neurons. The second was to determine if there is a functional role of antiresonance in shaping the activity of individual neurons and networks. The third and final aim was to examine the frequency-dependent actions of neuromodulation. Addressing these aims has led to general insight about the underlying mechanisms of frequency-preference in single neurons, its control by neuromodulation in distinct neuron types, and the functional consequences for the activity of such neurons in an oscillatory network.

I showed that variability in multiple ionic current properties can be compensated for by correlated expression. Correlated expression of ionic current parameters conserves multiple MPR features. One outcome of this could be to maintain the equality between f_{res} and $f_{\varphi=0}$ When this occurs the total amplitude of (one or many) ionic currents is largest when it is in-phase with voltage inputs. The kinetic parameters of ionic currents shift f_{res} because they shift the phase of ionic currents, which changes the frequency at which ionic current is maximum. I believe this to be a general rule for how MPR is generated in voltage clamp by one (or many) ionic currents.

Any ionic mechanism that produces MPR could generate spontaneous membrane potential oscillations [42]. Slowly inactivating inward currents, such as low-threshold calcium currents, may contribute to both the generation of oscillations and determination of the oscillation frequency in the pyloric pacemaker PD neurons. Furthermore, it is most likely that the kinetic parameters of such currents are under the control of neuromodulators, which regulates the oscillation frequency. Few studies have explored the dynamics of calcium currents in stomatogastric neurons (Johnson et al., 2003) and their role in the generation of rhythms at different frequencies in this network remains to be explored.

Our findings indicate novel aspects of neuromodulation, where rich dynamics in the rhythmic output of oscillatory networks are produced. First a single neuromodulator differentially alters the MPR properties of distinct neurons due to differences in intrinsic properties. The functional consequences of changes in MPR on network activity had not previously been explored. Using linear models, I showed that antiresonance may have profound consequences for the control of stable network oscillations. Secondly, the actions of neuromodulators can also be frequency-dependent due to the addition of novel time-dependent inward currents. Due to the inactivation properties of neuromodulator-activated ionic currents onset phase of bursting is preferentially advanced at short cycle periods. This could provide an additional mechanism to promote phase maintenance, a common phenomenon in the pyloric network whereby neurons maintain burst phase across a wide range of network cycle periods.

In conclusion, this thesis demonstrated that a combined experimental and computational approach is an effective way to understand how variability can lead to stable activity as seen in the MPR of neurons. Moreover, the use of nonlinear and linear modeling provides insights into the mechanisms that control the frequency-dependent responses of neurons and provides testable predictions for experimentalists.

APPENDIX

Supplementary Figures pertaining to Chapter 2

The figures in this appendix relate to supplementary material that accompany chapter 2. They are primarily concerned with the role of I_H in determining the multiple combinations of parameter values that shape MPR in the PD neurons.

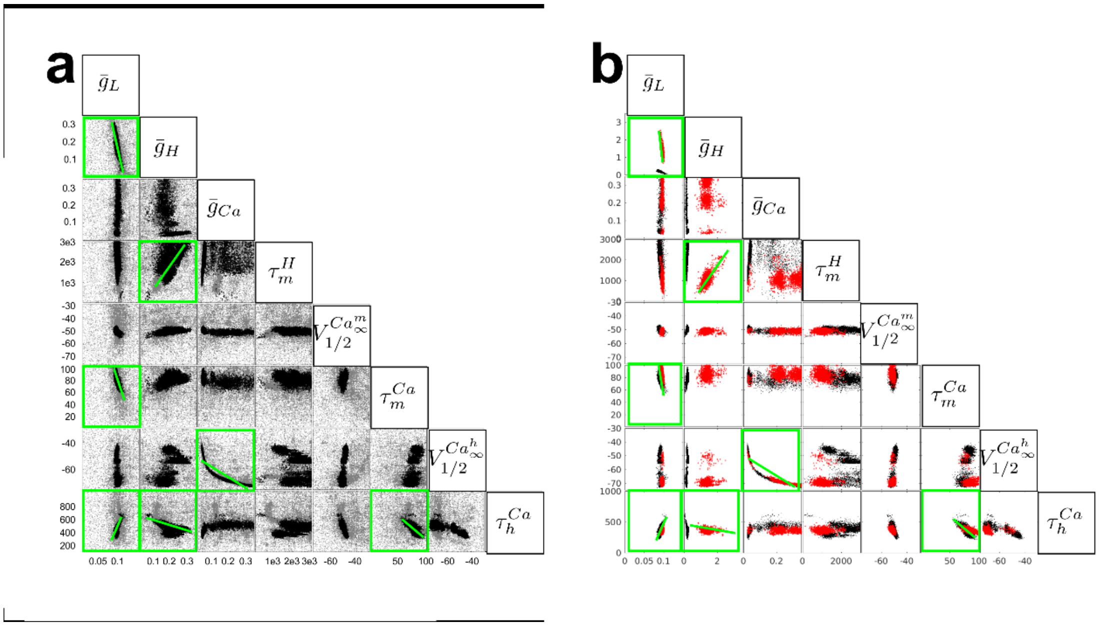

Figure A1, Changing the value of $V_{1/2}^{H_\infty^m}$ does not change the correlations observed among the model parameters. a. Correlations shown in Figure. 2.8b with $V_{1/2}^{H_\infty^m}$ at -70 mV. b. Correlations obtained with $V_{1/2}^{H_\infty^m}$ set to -96 mV (red dots). MOEA was run only once in this case, compared to 5 times in panel a (hence the difference in the number of points). Black dots are the same as panel a. Note that the values of $\bar{g}_H$ in this case are about 10 times larger than those in panel a, but the correlations (green boxes) remain intact. More importantly, the range of parameters other than $\bar{g}_H$ is exactly the same in both cases.

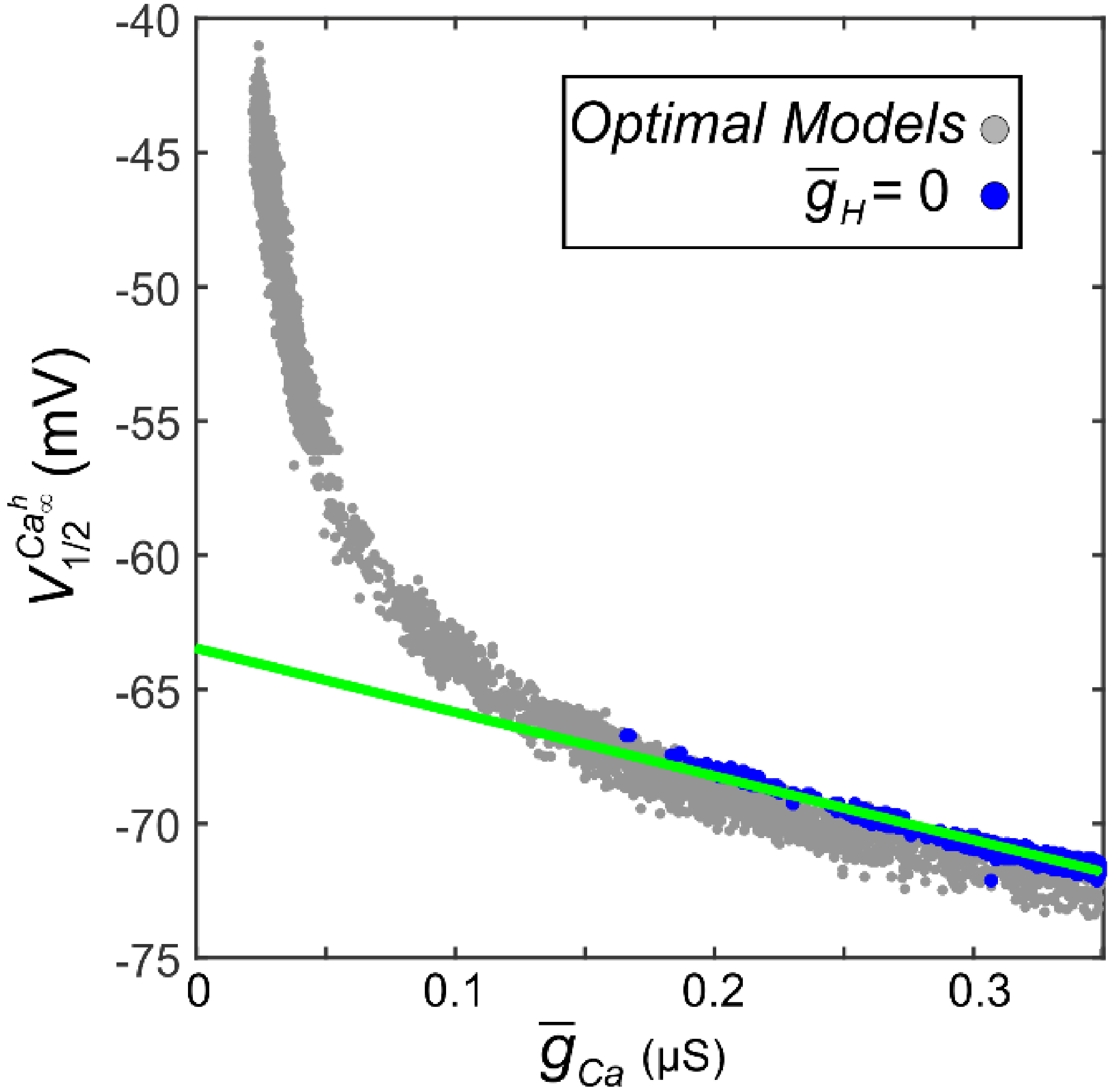

Figure A2. I_H extends the dynamic range of I_{Ca} parameters over which I_{Ca}-mediated MPR occurs. Parameter values for the optimal models in $\bar{g}_{Ca}$-$V_{1/2}^{Ca_{\infty}^{h}}$ space shown for all models (grey dots) and those without I_H (blue dots). We removed I_H by setting $\bar{g}_H$ = 0, and ran the MOEA multiple times using the same Z- and φ-profiles to constrain the I_{Ca} parameters. A linear fit (green) shows that, when $\bar{g}_H$ =0, the relationship between $\bar{g}_{Ca}$-$V_{1/2}^{Ca_{\infty}^{h}}$ is linear and matches a narrow range of the high $\bar{g}_{Ca}$ values in Figure 2.6c.

REFERENCES

1. Lau T, Zochowski M. The resonance frequency shift, pattern formation, and dynamical network reorganization via sub-threshold input. PLoS One. 2011;6(4):e18983.

2. Moca VV, Nikolic D, Singer W, Muresan RC. Membrane resonance enables stable and robust gamma oscillations. Cereb Cortex. 2014;24(1):119-42.

3. Sciamanna G, Wilson CJ. The ionic mechanism of gamma resonance in rat striatal fast-spiking neurons. J Neurophysiol. 2011;106(6):2936-49.

4. Tohidi V, Nadim F. Membrane resonance in bursting pacemaker neurons of an oscillatory network is correlated with network frequency. J Neurosci. 2009;29(20):6427-35.

5. Wu N, Hsiao CF, Chandler SH. Membrane resonance and subthreshold membrane oscillations in mesencephalic V neurons: participants in burst generation. J Neurosci. 2001;21(11):3729-39.

6. Pike FG, Goddard RS, Suckling JM, Ganter P, Kasthuri N, Paulsen O. Distinct frequency preferences of different types of rat hippocampal neurones in response to oscillatory input currents. J Physiol. 2000;529 Pt 1:205-13.

7. Richardson MJ, Brunel N, Hakim V. From subthreshold to firing-rate resonance. J Neurophysiol. 2003;89(5):2538-54.

8. Rotstein HG. Resonance modulation, annihilation and generation of anti-resonance and anti-phasonance in 3D neuronal systems: interplay of resonant and amplifying currents with slow dynamics. J Comput Neurosci. 2017;43(1):35-63.

9. Chen Y, Li X, Rotstein HG, Nadim F. Membrane potential resonance frequency directly influences network frequency through electrical coupling. J Neurophysiol. 2016:jn 00361

10. Stein W. Modulation of stomatogastric rhythms. J Comp Physiol A Neuroethol Sens Neural Behav Physiol. 2009;195(11):989-1009.

11. Harris-Warrick RM, Johnson BR. Checks and balances in neuromodulation. Front Behav Neurosci. 2010;4.

12. Nusbaum MP, Beenhakker MP. A small-systems approach to motor pattern generation. Nature. 2002;417(6886):343-50.

13. Marder E, Bucher D. Understanding circuit dynamics using the stomatogastric nervous system of lobsters and crabs. Annu Rev Physiol. 2007;69:291-316.

14. Rekling JC, Feldman JL. PreBotzinger complex and pacemaker neurons: hypothesized site and kernel for respiratory rhythm generation. Annu Rev Physiol. 1998;60:385-405.

15. Grillner S, Wallen P. On the cellular bases of vertebrate locomotion. Prog Brain Res. 1999;123:297-309.

16. Garcia VJ, Daur N, Temporal S, Schulz DJ, Bucher D. Neuropeptide receptor transcript expression levels and magnitude of ionic current responses show cell type-specific differences in a small motor circuit. J Neurosci. 2015;35(17):6786-800.

17. Goaillard JM, Taylor AL, Schulz DJ, Marder E. Functional consequences of animal-to-animal variation in circuit parameters. Nat Neurosci. 2009;12(11):1424-30.

18. Miller JP, Selverston AI. Mechanisms underlying pattern generation in lobster stomatogastric ganglion as determined by selective inactivation of identified neurons. II. Oscillatory properties of pyloric neurons. J Neurophysiol. 1982;48(6):1378-91.

19. Marder E, Eisen JS. Electrically coupled pacemaker neurons respond differently to same physiological inputs and neurotransmitters. J Neurophysiol. 1984;51(6):1362-74.

20. Bal T, Nagy F, Moulins M. The pyloric central pattern generator in Crustacea: a set of conditional neuronal oscillators. Journal of Comparative Physiology A. 1988;163(6):715-27.

21. Golowasch J, Bose A, Guan Y, Salloum D, Roeser A, Nadim F. A balance of outward and linear inward ionic currents is required for generation of slow-wave oscillations. J Neurophysiol. 2017;118(2):1092-104.

22. Marder E. Cholinergic motor neurones in the stomatogastric system of the lobster. J Physiol. 1976;257(1):63-86.

23. Marder E, Thirumalai V. Cellular, synaptic and network effects of neuromodulation. Neural Netw. 2002;15(4-6):479-93.

24. Kiehn O, Kjaerulff O, Tresch MC, Harris-Warrick RM. Contributions of intrinsic motor neuron properties to the production of rhythmic motor output in the mammalian spinal cord. Brain Res Bull. 2000;53(5):649-59.

25. Marder E, Hooper SL. Neurotransmitter modulation of the stomatogastric ganglion of decapod crustaceans. Model Neural networks and Behavior. 1985.

26. Marder E, Weimann JM. Modulatory control of multiple task processing in the stomatogastric nervous system. Neurobiology of Motor Progamme Selection. 1992.

27. Swensen AM, Marder E. Multiple peptides converge to activate the same voltage-dependent current in a central pattern-generating circuit. J Neurosci. 2000;20(18):6752-9.

28. Golowasch J, Marder E. Ionic currents of the lateral pyloric neuron of the stomatogastric ganglion of the crab. J Neurophysiol. 1992;67(2):318-31.

29. Tseng HA, Martinez D, Nadim F. The frequency preference of neurons and synapses in a recurrent oscillatory network. J Neurosci. 2014;34(38):12933-45.

30. Dembrow NC, Chitwood RA, Johnston D. Projection-specific neuromodulation of medial prefrontal cortex neurons. J Neurosci. 2010;30(50):16922-37.

31. Weimann JM, Skiebe P, Heinzel HG, Soto C, Kopell N, Jorge-Rivera JC, et al. Modulation of oscillator interactions in the crab stomatogastric ganglion by crustacean cardioactive peptide. J Neurosci. 1997;17(5):1748-60.

32. Szabo TM, Chen R, Goeritz ML, Maloney RT, Tang LS, Li L, et al. Distribution and physiological effects of B-type allatostatins (myoinhibitory peptides, MIPs) in the stomatogastric nervous system of the crab Cancer borealis. J Comp Neurol. 2011;519(13):2658-76.

33. Nusbaum MP, Marder E. A modulatory proctolin-containing neuron (MPN). II. State-dependent modulation of rhythmic motor activity. J Neurosci. 1989;9(5):1600-7.

34. Hooper SL, Marder E. Modulation of the lobster pyloric rhythm by the peptide proctolin. J Neurosci. 1987;7(7):2097-112.

35. Kramer RH, Levitan IB. Activity-dependent neuromodulation in Aplysia neuron R15: intracellular calcium antagonizes neurotransmitter responses mediated by cAMP. J Neurophysiol. 1990;63(5):1075-88.

36. Taylor AL, Goaillard JM, Marder E. How multiple conductances determine electrophysiological properties in a multicompartment model. J Neurosci. 2009;29(17):5573-86.

37. Fox DM, Tseng HA, Smolinski TG, Rotstein HG, Nadim F. Mechanisms of generation of membrane potential resonance in a neuron with multiple resonant ionic currents. PLoS Comput Biol. 2017;13(6):e1005565.

38. Guckenheimer J, Gueron S, Harris-Warrick RM. Mapping the dynamics of a bursting neuron. Philos Trans R Soc Lond B Biol Sci. 1993;341(1298):345-59.

39. Golowasch J, Goldman MS, Abbott LF, Marder E. Failure of averaging in the construction of a conductance-based neuron model. J Neurophysiol. 2002;87(2):1129-31.

40. Goldman MS, Golowasch J, Marder E, Abbott LF. Global structure, robustness, and modulation of neuronal models. J Neurosci. 2001;21(14):5229-38.

41. Rodriguez JC, Blitz DM, Nusbaum MP. Convergent rhythm generation from divergent cellular mechanisms. J Neurosci. 2013;33(46):18047-64.

42. Hutcheon B, Yarom Y. Resonance, oscillation and the intrinsic frequency preferences of neurons. Trends Neurosci. 2000;23(5):216-22.

43. Rathour RK, Narayanan R. Inactivating ion channels augment robustness of subthreshold intrinsic response dynamics to parametric variability in hippocampal model neurons. J Physiol. 2012;590(22):5629-52.

44. Gutfreund Y, Yarom Y, Segev I. Subthreshold oscillations and resonant frequency in guinea-pig cortical neurons: physiology and modelling. J Physiol. 1995;483(3):621-40.

45. Hutcheon B, Miura RM, Yarom Y, Puil E. Low-threshold calcium current and resonance in thalamic neurons: a model of frequency preference. J Neurophysiol. 1994;71(2):583-94.

46. Khorkova O, Golowasch J. Neuromodulators, not activity, control coordinated expression of ionic currents. J Neurosci. 2007;27(32):8709-18.

47. Schulz DJ, Goaillard JM, Marder EE. Quantitative expression profiling of identified neurons reveals cell-specific constraints on highly variable levels of gene expression. Proceedings of the National Academy of Sciences of the United States of America. 2007;104(32):13187-91.

48. McAnelly ML, Zakon HH. Coregulation of voltage-dependent kinetics of Na(+) and K(+) currents in electric organ. J Neurosci. 2000;20(9):3408-14.

49. Bucher D, Prinz AA, Marder E. Animal-to-animal variability in motor pattern production in adults and during growth. J Neurosci. 2005;25(7):1611-9.

50. Schmidt SL, Dorsett CR, Iyengar AK, Frohlich F. Interaction of Intrinsic and Synaptic Currents Mediate Network Resonance Driven by Layer V Pyramidal Cells. Cereb Cortex. 2016; 27(9): 4396-4410.

51. Norris BJ, Wenning A, Wright TM, Calabrese RL. Constancy and variability in the output of a central pattern generator. J Neurosci. 2011;31(12):4663-74.

52. Golowasch J. Ionic Current Variability and Functional Stability in the Nervous System. Bioscience. 2014;64(7):570-80.

53. Ransdell JL, Nair SS, Schulz DJ. Rapid homeostatic plasticity of intrinsic excitability in a central pattern generator network stabilizes functional neural network output. J Neurosci. 2012;32(28):9649-58.

54. Dicaprio R, Jordan G, Hampton T. Maintenance of motor pattern phase relationships in the ventilatory system of the crab. J Exp Biol. 1997;200(6):963-74.

55. Roffman RC, Norris BJ, Calabrese RL. Animal-to-animal variability of connection strength in the leech heartbeat central pattern generator. J Neurophysiol. 2012;107(6):1681-93.

56. Cohen AH, Ermentrout GB, Kiemel T, Kopell N, Sigvardt KA, Williams TL. Modelling of intersegmental coordination in the lamprey central pattern generator for locomotion. Trends Neurosci. 1992;15(11):434-8.

57. Manor Y, Bose A, Booth V, Nadim F. Contribution of synaptic depression to phase maintenance in a model rhythmic network. J Neurophysiol. 2003;90(5):3513-28.

58. MacLean JN, Zhang Y, Goeritz ML, Casey R, Oliva R, Guckenheimer J, et al. Activity-independent coregulation of IA and Ih in rhythmically active neurons. J Neurophysiol. 2005;94(5):3601-17.

59. MacLean JN, Zhang Y, Johnson BR, Harris-Warrick RM. Activity-independent homeostasis in rhythmically active neurons. Neuron. 2003;37(1):109-20.

60. Schulz DJ, Goaillard JM, Marder E. Variable channel expression in identified single and electrically coupled neurons in different animals. Nat Neurosci. 2006;9(3):356-62.

61. Tobin AE, Cruz-Bermudez ND, Marder E, Schulz DJ. Correlations in ion channel mRNA in rhythmically active neurons. PLoS One. 2009;4(8):e6742.

62. Tseng HA, Nadim F. The membrane potential waveform of bursting pacemaker neurons is a predictor of their preferred frequency and the network cycle frequency. J Neurosci. 2010;30(32):10809-19.

63. Hu H, Vervaeke K, Storm JF. Two forms of electrical resonance at theta frequencies, generated by M-current, h-current and persistent Na+ current in rat hippocampal pyramidal cells. J Physiol. 2002;545(3):783-805.

64. Zemankovics R, Kali S, Paulsen O, Freund TF, Hajos N. Differences in subthreshold resonance of hippocampal pyramidal cells and interneurons: the role of h-current and passive membrane characteristics. J Physiol. 2010;588(12):2109-32.

65. Erchova I, Kreck G, Heinemann U, Herz AV. Dynamics of rat entorhinal cortex layer II and III cells: characteristics of membrane potential resonance at rest predict oscillation properties near threshold. J Physiol. 2004;560(Pt 1):89-110.

66. Schreiber S, Erchova I, Heinemann U, Herz AV. Subthreshold resonance explains the frequency-dependent integration of periodic as well as random stimuli in the entorhinal cortex. J Neurophysiol. 2004;92(1):408-15.

67. Lampl I, Yarom Y. Subthreshold oscillations of the membrane potential: a functional synchronizing and timing device. J Neurophysiol. 1993;70(5):2181-6.

68. Lampl I, Yarom Y. Subthreshold oscillations and resonant behavior: two manifestations of the same mechanism. Neuroscience. 1997;78(2):325-41.

69. Puil E, Meiri H, Yarom Y. Resonant behavior and frequency preferences of thalamic neurons. J Neurophysiol. 1994;71(2):575-82.

70. Beatty JA, Song SC, Wilson CJ. Cell-type-specific resonances shape the responses of striatal neurons to synaptic input. J Neurophysiol. 2015;113(3):688-700.

71. Song SC, Beatty JA, Wilson CJ. The Ionic Mechanism of Membrane Potential Oscillations and Membrane Resonance in Striatal LTS Interneurons. J Neurophysiol. 2016:jn 00511

72. Rathour RK, Narayanan R. Homeostasis of functional maps in active dendrites emerges in the absence of individual channelostasis. Proceedings of the National Academy of Sciences of the United States of America. 2014;111(17):1787-96.

73. Rotstein HG, Nadim F. Frequency preference in two-dimensional neural models: a linear analysis of the interaction between resonant and amplifying currents. J Comput Neurosci. 2014;37(1):9-28.

74. Rotstein HG. Subthreshold amplitude and phase resonance in models of quadratic type: nonlinear effects generated by the interplay of resonant and amplifying currents. J Comput Neurosci. 2015;38(2):325-54.

75. Rotstein HG. Frequency Preference Response to Oscillatory Inputs in Two-dimensional Neural Models: A Geometric Approach to Subthreshold Amplitude and Phase Resonance. J Math Neurosci. 2014;4:11.

76. Buzsaki G. Theta oscillations in the hippocampus. Neuron. 2002;33(3):325-40.

77. Hu H, Vervaeke K, Graham LJ, Storm JF. Complementary theta resonance filtering by two spatially segregated mechanisms in CA1 hippocampal pyramidal neurons. J Neurosci. 2009;29(46):14472-83.

78. Tikidji-Hamburyan RA, Martinez JJ, White JA, Canavier CC. Resonant Interneurons Can Increase Robustness of Gamma Oscillations. J Neurosci. 2015;35(47):15682-95.

79. Stark E, Eichler R, Roux L, Fujisawa S, Rotstein HG, Buzsaki G. Inhibition-induced theta resonance in cortical circuits. Neuron. 2013;80(5):1263-76.

80. Marder E. Variability, compensation, and modulation in neurons and circuits. Proceedings of the National Academy of Sciences of the United States of America. 2011;108 Suppl 3:15542-8.

81. Puil E, Gimbarzevsky B, Miura RM. Quantification of membrane properties of trigeminal root ganglion neurons in guinea pigs. J Neurophysiol. 1986;55(5):995-1016.

82. Hutcheon B, Miura RM, Puil E. Subthreshold membrane resonance in neocortical neurons. J Neurophysiol. 1996;76(2):683-97.

83. Hodgkin AL, Huxley AF. A quantitative description of membrane current and its application to conduction and excitation in nerve. J Physiol. 1952;117(4):500-44.

84. Deb K. Multi-objective optimization using evolutionary algorithms. 1st ed. Chichester ; New York: John Wiley & Sons; 2001. xix, 497 p. p.

85. Gimbarzevsky B, Miura RM, Puil E. Impedance profiles of peripheral and central neurons. Can J Physiol Pharmacol. 1984;62(4):460-2.

86. Buchholtz F, Golowasch J, Epstein IR, Marder E. Mathematical model of an identified stomatogastric ganglion neuron. J Neurophysiol. 1992;67(2):332-40.

87. Mitchell M. An introduction to genetic algorithms. Cambridge, Mass.: MIT Press; 1996. viii, 205 p. p.

88. Malik A, Shim K, Prinz A, Smolinski T, G. Multi-objective evolutionary algorithms for analysis of conductance correlations involved in recovery of bursting after neuromodulator deprivation in lobster stomatogastric neuron models. BMC Neurosci. 2014;15(1):P370.

89. Deb K, Pratap A, Agarwal S, Meyarivan T. A fast and elitist multiobjective genetic algorithm: NSGA-II. IEEE Transactions on Evolutionary Computation. 2002;6(2):182-97.

90. Nowotny T, Levi R, Selverston AI. Probing the dynamics of identified neurons with a data-driven modeling approach. PLoS One. 2008;3(7):e2627.

91. Rathour RK, Malik R, Narayanan R. Transient potassium channels augment degeneracy in hippocampal active dendritic spectral tuning. Sci Rep. 2016;6:24678.

92. Prinz AA, Bucher D, Marder E. Similar network activity from disparate circuit parameters. Nat Neurosci. 2004;7(12):1345-52.

93. Rotstein HG, Olarinre M, Golowasch J. Dynamic compensation mechanism gives rise to period and duty-cycle level sets in oscillatory neuronal models. J Neurophysiol. 2016;116(5):2431-52.

94. Zhao S, Golowasch J. Ionic current correlations underlie the global tuning of large numbers of neuronal activity attributes. J Neurosci. 2012;32(39):13380-8.

95. Peck JH, Gaier E, Stevens E, Repicky S, Harris-Warrick RM. Amine modulation of Ih in a small neural network. J Neurophysiol. 2006;96(6):2931-40.

96. Wang XJ. Neurophysiological and computational principles of cortical rhythms in cognition. Physiol Rev. 2010;90(3):1195-268.

97. Engel TA, Schimansky-Geier L, Herz AV, Schreiber S, Erchova I. Subthreshold membrane-potential resonances shape spike-train patterns in the entorhinal cortex. J Neurophysiol. 2008;100(3):1576-89.

98. Rotstein HG. Resonance modulation, annihilation and generation of antiresonance and antiphasonance in 3D neuronal systems: interplay of resonant and amplifying currents with slow dynamics. bioaRxiv 2016;091207.

99. Prinz AA, Billimoria CP, Marder E. Alternative to hand-tuning conductance-based models: construction and analysis of databases of model neurons. J Neurophysiol. 2003;90(6):3998-4015.

100. Haas JS, White JA. Frequency selectivity of layer II stellate cells in the medial entorhinal cortex. J Neurophysiol. 2002;88(5):2422-9.

101. Johnson BR, Kloppenburg P, Harris-Warrick RM. Dopamine modulation of calcium currents in pyloric neurons of the lobster stomatogastric ganglion. J Neurophysiol. 2003;90(2):631-43.

102. Marder E, Calabrese RL. Principles of rhythmic motor pattern generation. Physiol Rev. 1996;76(3):687-717.

103. Ledoux E, Brunel N. Dynamics of networks of excitatory and inhibitory neurons in response to time-dependent inputs. Front Comput Neurosci. 2011;5:25.

104. Fellous JM, Houweling AR, Modi RH, Rao RP, Tiesinga PH, Sejnowski TJ. Frequency dependence of spike timing reliability in cortical pyramidal cells and interneurons. J Neurophysiol. 2001;85(4):1782-7.

105. Nadim F, Bucher D. Neuromodulation of neurons and synapses. Curr Opin Neurobiol. 2014;29:48-56.

106. Prescott SA, Ratte S, De Koninck Y, Sejnowski TJ. Pyramidal neurons switch from integrators in vitro to resonators under in vivo-like conditions. J Neurophysiol. 2008;100(6):3030-42.

107. Banks MI, Pearce RA, Smith PH. Hyperpolarization-activated cation current (Ih) in neurons of the medial nucleus of the trapezoid body: voltage-clamp analysis and enhancement by norepinephrine and cAMP suggest a modulatory mechanism in the auditory brain stem. J Neurophysiol. 1993;70(4):1420-32.

108. Halliwell JV, Adams PR. Voltage-clamp analysis of muscarinic excitation in hippocampal neurons. Brain Res. 1982;250(1):71-92.

109. Rabbah P, Nadim F. Distinct synaptic dynamics of heterogeneous pacemaker neurons in an oscillatory network. J Neurophysiol. 2007;97(3):2239-53.

110. Mamiya A, Nadim F. Dynamic interaction of oscillatory neurons coupled with reciprocally inhibitory synapses acts to stabilize the rhythm period. J Neurosci. 2004;24(22):5140-50.

111. Rotstein HG, Nadim F, editors. Current versus voltage clamp measurements of resonance in neuronal systems: lessons from the response of biophysical models to oscillatory inputs. Society for Neuroscience; 2014.

112. Fakler B, Adelman JP. Control of K(Ca) channels by calcium nano/microdomains. Neuron. 2008;59(6):873-81.

113. Oh M, Zhao S, Matveev V, Nadim F. Neuromodulatory changes in short-term synaptic dynamics may be mediated by two distinct mechanisms of presynaptic calcium entry. J Comput Neurosci. 2012;33(3):573-85.

114. Graubard K. Synaptic transmission without action potentials: input-output properties of a nonspiking presynaptic neuron. J Neurophysiol. 1978;41(4):1014-25.

115. Wilkens JL, Shinozaki T, Yazawa T, ter Keurs HE. Sites and modes of action of proctolin and the FLP F2 on lobster cardiac muscle. J Exp Biol. 2005;208(4):737-47.

116. Prinz AA, Thirumalai V, Marder E. The functional consequences of changes in the strength and duration of synaptic inputs to oscillatory neurons. J Neurosci. 2003;23(3):943-54.

117. Harris-Warrick RM, Marder E. Modulation of neural networks for behavior. Annu Rev Neurosci. 1991;14:39-57.

118. Marder E. Neuromodulation of neuronal circuits: back to the future. Neuron. 2012;76(1):1-11.

119. Goaillard JM, Taylor AL, Pulver SR, Marder E. Slow and persistent postinhibitory rebound acts as an intrinsic short-term memory mechanism. J Neurosci. 2010;30(13):4687-92.

120. Hooper SL, Buchman E, Weaver AL, Thuma JB, Hobbs KH. Slow conductances could underlie intrinsic phase-maintaining properties of isolated lobster (Panulirus interruptus) pyloric neurons. J Neurosci. 2009;29(6):1834-45.

121. Nadim F, Brezina V, Destexhe A, Linster C. State dependence of network output: modeling and experiments. J Neurosci. 2008;28(46):11806-13.

122. Spitzer N, Cymbalyuk G, Zhang H, Edwards DH, Baro DJ. Serotonin transduction cascades mediate variable changes in pyloric network cycle frequency in response to the same modulatory challenge. J Neurophysiol. 2008;99(6):2844-63.

123. Brookings T, Goeritz ML, Marder E. Automatic parameter estimation of multicompartmental neuron models via minimization of trace error with control adjustment. J Neurophysiol. 2014;112(9):2332-48.

124. Zhao S, Golowasch J, Nadim F. Pacemaker neuron and network oscillations depend on a neuromodulator-regulated linear current. Front Behav Neurosci. 2010;4:21.

125. Huguenard JR. Low-threshold calcium currents in central nervous system neurons. Annu Rev Physiol. 1996;58:329-48.

126. Huguenard JR, McCormick DA. Simulation of the currents involved in rhythmic oscillations in thalamic relay neurons. J Neurophysiol. 1992;68(4):1373-83.

127. Hernandez-Cruz A, Pape HC. Identification of two calcium currents in acutely dissociated neurons from the rat lateral geniculate nucleus. J Neurophysiol. 1989;61(6):1270-83.

128. Takahashi K, Ueno S, Akaike N. Kinetic properties of T-type Ca2+ currents in isolated rat hippocampal CA1 pyramidal neurons. J Neurophysiol. 1991;65(1):148-55.

129. Fraser DD, MacVicar BA. Low-threshold transient calcium current in rat hippocampal lacunosum-moleculare interneurons: kinetics and modulation by neurotransmitters. J Neurosci. 1991;11(9):2812-20.

130. Turrigiano G, LeMasson G, Marder E. Selective regulation of current densities underlies spontaneous changes in the activity of cultured neurons. J Neurosci. 1995;15(5 Pt 1):3640-52.

131. Harris-Warrick RM, Coniglio LM, Levini RM, Gueron S, Guckenheimer J. Dopamine modulation of two subthreshold currents produces phase shifts in activity of an identified motoneuron. J Neurophysiol. 1995;74(4):1404-20.

132. Thirumalai V, Prinz AA, Johnson CD, Marder E. Red pigment concentrating hormone strongly enhances the strength of the feedback to the pyloric rhythm oscillator but has little effect on pyloric rhythm period. J Neurophysiol. 2006;95(3):1762-70.

133. Nadim F, Zhao S, Zhou L, Bose A. Inhibitory feedback promotes stability in an oscillatory network. J Neural Eng. 2011;8(6):065001.

134. Fuhrmann G, Markram H, Tsodyks M. Spike frequency adaptation and neocortical rhythms. J Neurophysiol. 2002;88(2):761-70.

135. Huguenard JR, Prince DA. Intrathalamic rhythmicity studied in vitro: nominal T-current modulation causes robust antioscillatory effects. J Neurosci. 1994;14(9):5485-502.

136. McCormick DA, Pape HC. Properties of a hyperpolarization-activated cation current and its role in rhythmic oscillation in thalamic relay neurones. J Physiol. 1990;431:291-318.